International Journal of Advances in Telecommunications Electrotechnics, Signals and Systems

Vol. 1, No. 2-3
2012

www.ijates.org

International Journal of
Advances in Telecommunications
Electrotechnics, Signals and Systems

a publication of the International Science and Engineering Society

Aims and Scope

The International Journal of Advances in Telecommunications, Electronics, Signals and Systems (IJATES^2) is an all-electronic international scientific journal with the aim to bring the most recent and unpublished research and development results in the area of electronics to the scientific and technical societies, and is supported by the ISES (International Science and Engineering Society, o.s.). The journal's scope covers all the aspects of telecommunication, signal processing, theory and design of circuits and systems for electronics.

The IJATES^2 is ready to publish experimental and theoretical full papers and letters submitted by prospective authors. Paper submitted for publication must be written in English and must follow a prescribed format. All papers are subjected to a critical peer-review prior to publication.

The IJATES^2 is an open access journal which means that all content is freely available without charge to the user or his/her institution. Users are allowed to read, download, copy, distribute, print, search, or link to the full texts of the articles in this journal without asking prior permission from the publisher or the author. This journal provides immediate open access to its content on the principle that making research freely available to the public supports a greater global exchange of knowledge.

www.ijates.org

CONTENTS

Universal Voltage Conveyor and Current Conveyor in Fast Full-Wave Rectifier

Josef Burian, Jaroslav Koton, and Norbert Herencsar

Abstract—This paper deals with the design of a fast voltage-mode full-wave rectifier, where universal voltage conveyor and second-generation current conveyor are used as active elements. Thanks to the active elements, in theory the input and output impedance of the non-linear circuit is infinitely high respectively zero. For the rectification only two diodes and three resistors are required as passive elements. The performance of the circuit is shown on experimental measurement results showing the dynamic range, time response, frequency dependent DC transient value and RMS error for different values of input voltage amplitudes.

Keywords—Universal voltage conveyor, current conveyor, fast full-wave rectifier.

I. Introduction

In instrumentation and measurement, precision rectifiers serve as very important blocks. They are used in applications such as ac voltmeters and ammeters, signal-polarity detectors, averaging circuits, peak-value detector rectification function is of great importance [1]. The threshold voltage of the diodes does not enable to use simple rectifiers if low-voltage signals are to be analyzed. Therefore precision rectifiers employing active elements have to be used.

As the nowadays systems operate at higher frequency bands, also the single functional blocks, analog or digital, have to be able to process the higher frequency signals. In area of precision full-wave rectifiers, the solutions using standard operational amplifiers are probably the most known [2]. However, such structures are able to operate well only at frequencies much bellow the transient frequency of the active element, mainly because of the finite slew-rate [3], [4]. To design non-linear structures, i.e. also rectifiers, operating at higher frequencies it is suitable to drive the diodes by current, which actually means to connect them to high-impedance current outputs of an active element. For this purpose, the second generation current conveyor (CCII) is used in the full-wave rectifier discussed in [5]. The same structure from [5] using two active elements and four diodes is also analyzed in [6]-[8]. As two diodes are grounded, the voltage- [5], [8] or current- [7], [8] biasing scheme can be used to further extend the operational region. Another precision full-wave rectifier based on operational amplifier structure is given in [9], where the original operational amplifier is replaced by the operational conveyor and latter by second generation current

J. Burian, J. Koton, and N. Herencsar are with the Brno University of Technology, Dept. of Telecommunications, Purkynova 118, 612 00 Brno, Czech Republic (corresponding author: koton@feec.vutbr.cz).

conveyor [4]. Once the diodes in the structure are replaced by NMOS transistors the MOS only rectifiers using CCII and dual-X current conveyors were presented in [10] and [11], respectively.

The operational transconductance amplifiers (OTA) feature with the high-impedance current output and hence are also suitable for the design of fast non-linear circuits [12]. In [13] or [14] transistors operating as switches are connected to the output of the OTA subsequently providing full-wave rectification. Operating the OTAs in weak inversion region the transconductance of the active element is controlled by the current derived from the input signal to be rectified. Such idea is presented in [15] and [16].

In this paper we present a new circuit solution of a voltage-mode full-wave rectifier using one universal voltage conveyor and one second generation current conveyor as active elements. The only two diodes used in the structure are suitably driven by current to enable the high-frequency signal processing. Thanks to the active elements used, the input impedance of the non-linear circuit is infinitely high in theory. The rectifier provides both inverting and non-inverting voltage responses that are taken at the output of voltage buffers having zero impedance in theory. Therefore, the structure is very suitable to be connected into the signal path without any additional circuitry. To show and make it possible to compare the performance of the new rectifier, the frequency dependent RMS error and DC transient value for different amplitudes of the input signal are evaluated. Measurement results of the DC and transient analyses are also given that show the feasibility to rectify the signals of frequency 2MHz and beyond.

II. Current and Voltage Conveyor

The current conveyors have been presented in 1968 for the very first time [17], however, they did not found any significant usage as the operational amplifiers were more attractive at that time. Current conveyors received considerable attention after the second (CCII) [18] and later third (CCIII) [19] generation current conveyors were designed. These elements are now advantageously used in applications, where the wide bandwidth or current output response is necessary. Mainly the CCII is used as basic active element from which other types of active elements can be derived, such as the current controlled CC (CCCII) [20], differential voltage CC (DVCC) [21], or electronically tunable CC (ECCII) [22]. The behavior of a three-terminal positive CCII (Fig. 1(a)) is described by following equations:

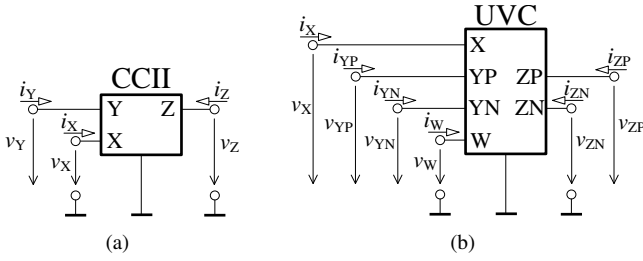$$v_X = v_Y, \quad i_Y = 0, \quad i_Z = i_X. \tag{1}$$

Fig. 1. Circuit symbol of (a) the three-terminal CCII, (b) the universal voltage conveyor UVC
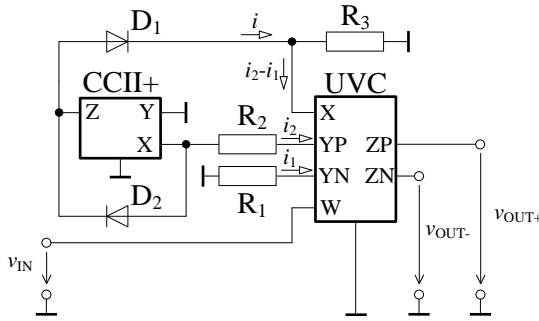

Fig. 2. Proposed fast full-wave rectifier

Another flexible building block for active circuit synthesis is the voltage conveyor (VC) that has been presented in [23]. Based on the duality principle to current conveyors, also first-, second-, and third-generation voltage conveyors can be described [24]. The current differencing buffered amplifier (CDBA) [25] can be identified as the differential current voltage conveyor (DCVC+) [26]. In [27], [28] the universal voltage conveyor (UVC) has been described (Fig. 1(b)). It is a 6-port active element that has one voltage input X, two current differencing inputs YP and YN, and two mutually inverse voltage outputs ZP and ZN. Connecting the auxiliary voltage input W either to ZP, common node (ground), or ZN the three generations of voltage conveyors can be designed [28]. The relation between the terminal currents and voltages is described by following set of equations:

$$i_X = i_{YP} - i_{YN}, \quad v_{YP} = v_{YN} = v_W, \qquad (2)$$

$$v_{ZP} = v_X, \quad v_{ZN} = -v_X. \qquad (3)$$

III. PROPOSED FULL-WAVE RECTIFIER

As already given in the text above, the terminal W of the universal voltage conveyor is used to determine the generation of the voltage conveyor. However, it can be also used as an independent voltage input of a functional block featuring with infinitely high input impedance in theory. This fact is with advantage used for the design of the precision full-wave rectifier shown in Fig. 2.

For positive input voltage v_{IN} the diode D_2 is open and the current i through D_1 is therefore zero. Hence, the current flowing through the resistor R_3 is equal to the difference of i_2

and i_1 currents. The output voltages of this functional block can subsequently be derived as:

$$v_{OUT+} = -v_{OUT-} = -\left(\frac{1}{R_2} - \frac{1}{R_1}\right)R_3 v_{IN}, \quad v_{IN} > 0. \quad (4)$$

If the input voltage is negative, the diode D_1 is open, the current i equals to the current flowing through the resistor R_2 and the output voltage can be determined as follows:

$$v_{OUT+} = -v_{OUT-} = -\frac{R_3}{R_1}v_{IN}, \quad v_{IN} < 0. \qquad (5)$$

Comparing (4) and (5), if the circuit from Fig. 2 should really perform the operation of full-wave rectification, following condition needs to be fulfilled:

$$\frac{1}{R_2} - \frac{1}{R_1} = \frac{1}{R_1}, \qquad (6)$$

which for the values of the resistors R_1 and R_2 means: $R_1 = 2R_2$. The required voltage gain can be then adjusted by the ratio of the resistors R_3 and R_1.

IV. EVALUATED PARAMETERS DESCRIPTION

Except the common measurements as are the DC transfer showing proper operation area of the functional block and time responses of the output signal, to compare current circuit solution to other rectifiers, it is suitable to also evaluate the frequency dependent DC value transfer p_{DC} and RMS error p_{RMS} [29]:

$$p_{DC} = \frac{\int\limits_T y_R(t)\,dt}{\int\limits_T y_{ID}(t)\,dt}, \qquad (7)$$

$$p_{RMS} = \sqrt{\frac{\int\limits_T [y_R(t) - y_{ID}(t)]^2\,dt}{\int\limits_T y_{ID}^2(t)\,dt}}, \qquad (8)$$

where the $y_R(t)$ and $y_{ID}(t)$ represent the actual and ideally rectified signal and T is the period of the rectified signal. The ideal behavior of the rectifier is characterized by the values $p_{DC} = 1$ and $p_{RMS} = 0$. Increasing the frequency and decreasing the magnitude of the input signal, compared to ideally rectified signal deviations of the actual output voltage $v_{OUT}(t)$ occur and p_{DC} decreases below one and p_{RMS} increases.

Another possibility, how to evaluate proper behavior of the rectifier is to analyze the harmonic components of the output signal [4]. When a sinusoidal signal of frequency ω is applied to full-wave rectifier, the steady-state response at the output ideally consists of even harmonic components at frequencies of 2ω, 4ω, 6ω, etc., the odd harmonic components are zero. Using the Fourier series analysis the coefficients, i.e. the magnitudes of harmonic components of the output signal can be found as:

$$V_{2(2n)} = \frac{4V_{INmax}}{\pi}\frac{1}{4n^2 - 1}, \qquad (9)$$

where V_{INmax} is the amplitude of the input signal to be rectified, and $n = 1, 2, 3, ...$ defines the the $2n$-th harmonic component of the output signal.
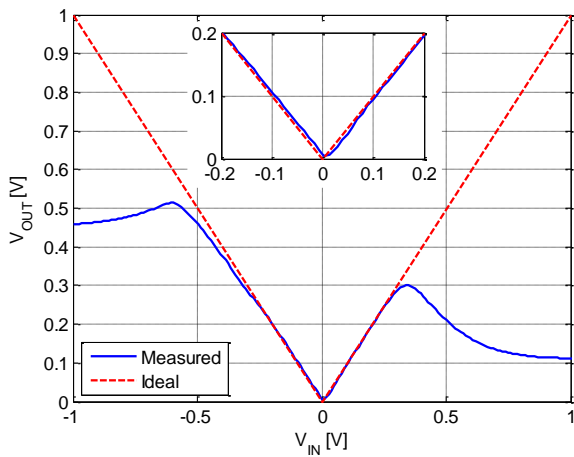
Fig. 3.   DC transfer of the proposed full-wave rectifier
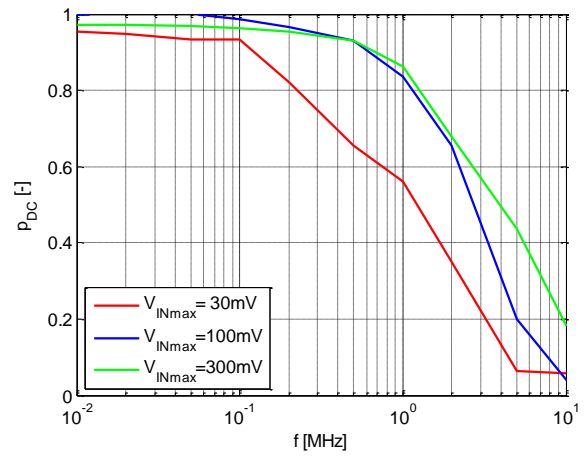
Fig. 5.   The DC value transfer for different input signal magnitudes
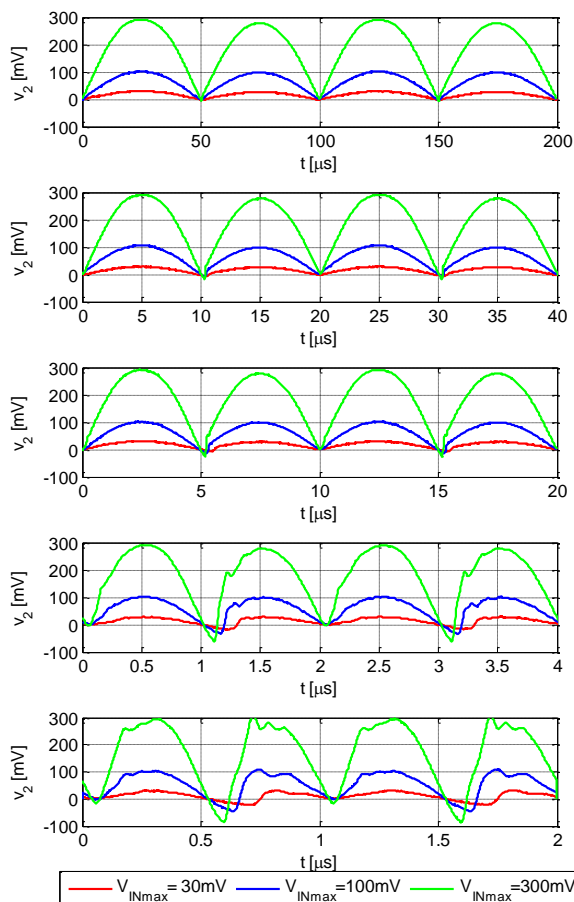
Fig. 4.   Measured transient responses for $V_{\mathrm{INmax}} = \{30; 100; 300\}$ mV and frequencies 10 kHz, 50 kHz, 100 kHz, 500 kHz, and 1 MHz

Fig. 6.   The RMS error for different input signal magnitudes

V. MEASUREMENT RESULTS

The proposed fast full-wave rectifier has been further analyzed by experimental measurements. As active elements the universal current conveyor UCC-N1B [30] and universal voltage conveyor UVC-N1C [31] have been used. The values of the resistors are $R_1 = R_3 = 1$ kΩ, $R_2 = 500$ Ω, and the diodes are all-purpose 1N4148 [32].

The measured DC transfer characteristic is shown in Fig. 3.

In practice, the active elements use ± 1.65 V supply voltage. From the parameters in [30] and [31], linear behavior of the UCC and UVC is defined for terminal voltages and currents up to ± 0.7 V and ± 0.7 μA . Therefore, to prevent the active elements to operate in their saturation region, the processed input signals should be of maximal magnitude 300 mV. The transient responses of the rectifier for input signal magnitudes $V_{\mathrm{INmax}} = \{30; 100; 300\}$ mV and frequencies 10 kHz, 50 kHz, 100 kHz, 500 kHz and 1 MHz are shown in Fig. 4. From the measurement results it can be seen that for input signal frequencies from 10 kHz to 100 kHz there are no or minor distortions of the output signal. First for the frequency 500 kHz more visible deviations in zero-cross area can be observed. Anyway, even if the transient responses do not fully agree to the ideally rectified signal, the deviations are not that significant as we are mainly interested in the DC component of the output signal.

Using (7) and (8), from transient measurements the frequency dependent DC value transfer p_{DC} and RMS error p_{RMS} for input signal magnitudes 30 mV, 100 mV, and 300 mV were evaluated and are shown in Fig. 5 and Fig. 6, respectively. As it can be seen from the graphs, at low frequencies the higher the magnitude of the input signal the closer are the values of p_{DC}
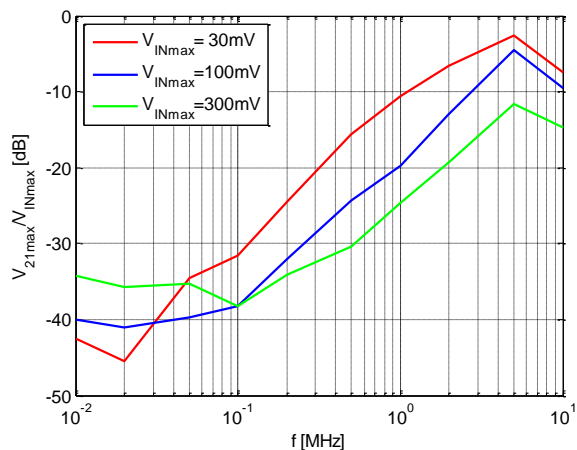
Fig. 7.   Variation of the fundamental component magnitude of the output signal for different input signal magnitudes
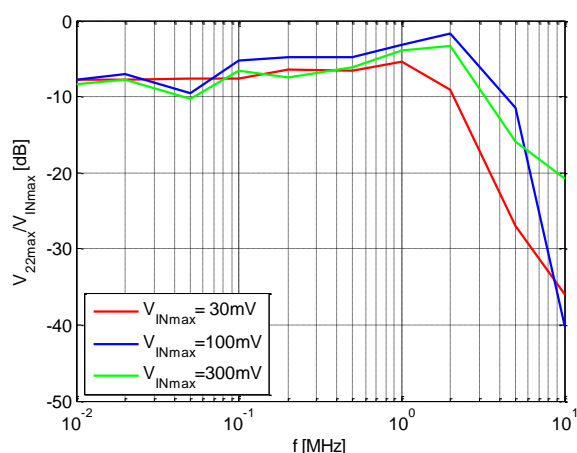
Fig. 8.   Variation of the second-harmonic (2ω) component magnitude of the output signal for different input signal magnitudes

and p_{RMS} parameters to the ideal ones. Once the frequency increases the p_{DC} drops below unity and for the magnitude of 300 mV the rectifier can be used to process signals up to 2 MHz (p_{DC-3dB}).

The harmonic components of the output signal have also been analyzed. According to the theory, the odd harmonic components of the fundamental frequency ω are zero, i.e. $-\infty$dB. However, based on the measurements, it is in the range of -40 dB at low frequencies, see Fig. 7. As the frequency of the input signal increases, also the magnitude of fundamental component at the output increases. The drop of magnitude at frequencies higher than 5 MHz is caused by the active elements, as they start to attenuate the input signal. The magnitude of second-harmonic component is shown in Fig. 8. As it could be expected from (9), the magnitude of the second-harmonic component is close to -7.44 dB for all magnitudes of the input signal. Increasing the frequency, the magnitude drops down as the circuit looses its feature to rectify the signal.

VI. CONCLUSION

In this paper a new realization of the voltage-mode full-wave rectifier has been presented. The structure uses one universal voltage conveyor and one second-generation current conveyor (CCII). The two diodes are directly connected and driven by the current terminal of the CCII, which enables high frequency operation of the functional block. The behavior of the proposed rectifier has been verified by experimental measurements, where except of the DC transfer and time responses, the frequency dependent DC value transfer p_{DC} and RMS error p_{RMS} have also been evaluated.

REFERENCES

[1] C. Toumazou, F. J. Lidgey, and D. G. Haigh, "*Analogue IC design: The current-mode approach*," London: Peter Peregrinus Ltd., 1990.

[2] U. Tietze, Ch. Schenk, and E. Gramm, "*Electronic Circuits-Handbook for Design and Application*", Springer, 2008.

[3] C. Toumazou and F. J. Lidgey, "Fast current-mode precision rectifier", *Electron. Wireless World*, 1987, vol. 93, no. 1621, pp. 1115-1118.

[4] S. J. G. Gift and B. Maundy, "Versatile precision full-wave rectifiers for instrumentation and measurements", *IEEE Trans Instrum. Meas.*, 2007, vol. 56, no. 5, pp. 1703-1710.

[5] C. Toumazou, F. J. Lidgey, and S. Chattong, "High frequency current conveyor precision full-wave rectifier", *Electronics Letters*, 1994, vol. 30, no. 10, pp. 745-746.

[6] A. A. Khan, M. A. El-Ela, and M. A. Al-Turaigi, "Current-mode precision rectification", *Int. J. Electron.*, 1995, vol. 79, no. 6, pp. 853-859.

[7] B. Wilson and V. Mannama, "Current-mode rectifier with improved precision", *Electronics Letters*, 1995, vol. 31, no. 4, pp. 247-248.

[8] D. Stiurica, "Truly temperature independent current conveyor precision rectifier", *Electronics Letters*, 1995, vol. 31, no. 16, pp. 1302-1303.

[9] S. J. G. Gift, "A high-performance full-wave rectifier circuit", *Int. J. Electron.*, 2000, vol. 87, no. 8, pp. 925-930.

[10] E. Yuce, S. Minaei, and O. Cicekoglu, "Full-wave rectifier realization using only two CCII+s and NMOS transistors", *Int. J. Electron.*, 2006, vol. 93, no. 8, pp. 533-541.

[11] S. Minaei and E. Yuce, "A new full-wave rectifier circuit employing single dual-X current conveyor", *Int. J. Electron.*, 2008, vol. 95, no. 8, pp. 777-784.

[12] K. Montree, "High frequency and high precision CMOS full-wave rectifier", in *Proc. IEEE Int. Conf. Communication Systems*, 2010, pp. 5-8.

[13] S. Maheshawari, "Current controlled precision rectifier circuits", *J. Circuits, Systems, and Computers*, 2007, vol. 16, no. 1, pp. 129-138.

[14] N. Minhaj, "OTA-based non-inverting and inverting precision fullwave rectifier circuits without diodes", *Int. J. Recent Trends in Engineering*, 2009, vol. 1, no. 3, pp. 72-75.

[15] C. Jongkunstidchai, C. Fongsamut, K. Kumwachara, and W. Surakampontorn, "Full-wave rectifiers based on operational transconductance amplifiers", *Int. J. Electron. Commun.*, 2007, vol. 61, pp. 195-201.

[16] C. Chanapromma and K. Daoden, "A CMOS fully differential operational transconductance amplifier operating in sub-threshold region and its application", in *Proc. IEEE 2nd Int. Conf. Signal Proc. Systems - ICSPS 2010*, 2010, pp. V2-73-V2-77.

[17] K. C. Smith and A. Sedra, "The current conveyor: a new circuit building block", *IEEE Proc.*, vol. 56, pp. 1368-1369, 1968.

[18] A. Sedra adnd K.C. Smith, "A second-generation current conveyor and its application", *IEEE Trans. Circ. Th.*, vol. 17, pp. 132-134, 1970.

[19] A. Fabre, "Third-generation current conveyor: a new helpful active element", *Electronics Letters*, vol. 31, no. 5, pp. 338-339, 1995.

[20] A. Fabre, O. Saaid, F. Wiest, and C. Baucheron, "High frequency applications based on a new current controlled conveyor", *IEEE Trans. Circuits Syst.-I*, vol. 43, no. 2, pp. 82-90, 1996.

[21] H. O. Elwan and A. M. Soliman, "Novel CMOS differential voltage current conveyor and its applications", *IEE Proc. Circuits, Devices, Systems*, vol. 144, no. 3, pp. 195-200, 1997.

[22] W. Surakampontorn and K. Kumwachara, "CMOS-based electronically tunable current conveyor", *Electronics Letters*, vol. 28, no. 14, pp. 1316-1317, 1992.

[23] I. M. Filanovsky and K. A. Stromsmoe, "Current-voltage conveyor", *Electronics Letters*, vol. 17, no. 3, pp. 129-130, 1981.

[24] T. Dostal and J. Pospisil, "Hybrid models of 3-port immittance convertors and current and voltage conveyors", *Electronics Letters*, vol. 18, no. 20, pp. 887-888, 1982.

[25] C. Acar and S. Ozoguz, "A new versatile building block: current differencing buffered amplifier suitable for analog signal processing filters", *Microelectronics Journal*, vol. 30, no. 2, pp. 157-160, 1999.

[26] K. Salama and A. Soliman, "Novel MOS-C quadrature oscillator using the differential current voltage conveyor", in *Proc. 42nd Midwest Symposium on Circuits and Systems - MWSCAS 99*, Las Cruces, USA, pp. 279-282, 1999.

[27] J. Koton, K. Vrba, and N. Herencsar, "Tuneable filter using voltage conveyors and current active elements", *Int. J. Electron.*, vol. 96, no. 8, pp. 787-794, 2009.

[28] J. Koton, N. Herencsar, and K. Vrba, "KHN-equivalent voltage-mode filters using universal voltage conveyors", *Int. J. Electron. Commun.*, vol. 65, no. 2, pp. 154-160, 2011, doi:10.1016/j.aeue.2010.02.005.

[29] D. Biolek, V. Biolkova, and Z. Kolka, AC analysis of operational rectifiers via conventional circuit simulators, in *Proc. WSEAS Transactions on Circuits and Systems*, vol. 3, no. 10, pp. 2291- 2295, 2004.

[30] Datasheet UCC-N1B: Universal Current Conveyor (UCC) and Second-Generation Current Conveyor (CCII+/-), Rev.0, 2010, available online: http://www.utko.feec.vutbr.cz/koton/soubory/ucc_n1b_rev0.pdf.

[31] Datasheet UVC-N1C 0520: Universal Voltage Conveyor, Rev.0, 2010, available online: http://www.utko.feec.vutbr.cz/herencsar/UVC_N1C_0520.pdf.

[32] Datasheet High-speed diodes 1N4148; 1N4448, NXP Semiconductors, Aug. 2004, avaialble online: www.nxp.com/documents/data_sheet/1N4148_1N4448.pdf

Josef Burian received the B.Sc. degree in electrical engineering from the Brno University of Technology, Czech Republic, in 2011. Currently, he is finishing his master studies in electrical engineering at the Brno University of Technology, Czech Republic. His research is focused on measurement, analysis and design of linear and non-linear functional blocks.

Jaroslav Koton received the M.Sc. an Ph.D. degree in electrical engineering from the Brno University of Technology, Czech Republic, in 2006 and 2009, respectively. He is currently an Assistant Professor at the Department of Telecommunications of the Faculty of Electrical Engineering and Communication of Brno University of Technology, Czech Republic. His current research is focused on linear and non-linear circuit designing methods with current or voltage conveyors, and current active elements. He is an author or co-author of about 85 research articles published in international journals or conference proceedings. Dr. Koton is a Member of IEEE and IACSIT.

Norbert Herencsar received the M.Sc. and Ph.D. degrees in Electronics & Communication and Teleinformatics from Brno University of Technology (BUT), Brno, Czech Republic, in 2006 and 2010, respectively. Currently, he is an Assistant Professor at the Dept. of Telecommunications, BUT. From September 2009 through February 2010 he was an Erasmus Exchange Student with the Dept. of Electrical and Electronic Engineering, Bogazici University, Istanbul, Turkey. His research interests include analog filters, current-mode circuits, tunable frequency filter design methods, and oscillators. He is an author or co-author of about 75 research articles published in international journals or conference proceedings. Dr. Herencsar is a Member of IEEE, ACEEE, IAENG, and Senior Member of IACSIT.

Implementation of Mobility Management Methods for MANET

Pavel Vajsar, Jiri Hosek, Milan Bartl and Karol Molnar

Abstract—The Mobile Adhoc Networks represent very perspective way of communication. The mobility management is on the most often discussed research issues within these networks. There have been designed many methods and algorithms to control and predict the movement of mobile nodes, but each method has different functional principle and is suitable for different environment and network circumstances. Therefore, it is advantageous to use a simulation tool in order to model and evaluate a mobile network together with the mobility management method. The aim of this paper is to present the implementation process of movement control methods into simulation environment OPNET Modeler based on the TRJ file. The described trajectory control procedure utilized the information about the route stored in the GPX file which is used to store the GPS coordinates. The developed conversion tool, implementation of proposed method into OPNET Modeler and also final evaluation are presented in this paper.

Keywords— GPS, GPX, MANET, mobility, OPNET Modeler, simulation, software.

I. INTRODUCTION

AD-HOC networks recently represent one of the most attractive research fields in telecommunication technology. The wireless ad-hoc network is a decentralized network that does not rely on any pre-existing communication infrastructure. Each wireless node is capable of movement and can participate in the routing process by forwarding data to other neighbouring nodes [1], [2].

Mobile Ad-hoc Network (MANET) is one of the technologies that belong to the wireless ad-hoc networks. MANET represents a system of wireless mobile nodes which can freely and dynamically self-organize into a dynamic network with temporary topology allowing users and devices internetwork seamlessly [3].

Because, the MANET is a communication system consisting of mobile nodes, one of the important factors in the simulation of these networks is the ability to control the movement of mobile nodes during the simulation. For this reason, the mobility control of individual nodes or entire networks becomes a key factor for the testing and simulation of communication systems [4]. While keeping the functionality of mobile nodes and networks, wireless communication allows changing their position based on the

Pavel Vajsar[1], Jiri Hosek[2] and Milan Bartl[3] are with Department of Telecommunications, Brno University of Technology, Brno, Czech Republic (e-mails: pavel.vajsar@phd.feec.vutbr.cz[1], hosek@feec.vutbr.cz[2], bartl02@stud.feec.vutbr.cz[3]).
Karol Molnar is with the Honeywell International, s.r.o. (e-mail: Karol.Molnar@honeywell.com).

predefined trajectories, orbits and randomly selected routes [5].

The possibility to control the movement of mobile node allows more effective prediction and scheduling of network sources for individual stations, such as handover optimization in MANETs.

II. TRAJECTORY CONTROL IN OPNET MODELER

In the environment of OPNET Modeler (OM), there are several ways to control the trajectory of mobile node. Firstly, the type of trajectory is chosen and then its assignment to the selected node is defined. There are more trajectory types and ways of assignment in the simulation environment OPNET Modeler, see following chapters [6].

A. Segment-based trajectory

In order to exactly determine the trajectory of mobile node in OM, user can use the segment-based trajectory. Thus defined trajectory consists of one or more traversal-time values and a set of three-dimensional (x, y, altitude) coordinates that define the mobile node's path. In addition, trajectories with variable-length segments have a set of angles (roll, pitch, yaw) that define the mobile node's orientation in space. Segment-based trajectories are stored in ASCII text files with a *.trj extension. For proper functionality of so defined trajectory, it is necessary to place the *.trj file into a folder created by the project and then assign this file with defined trajectory to a mobile node or network using the "trajectory" attribute [6].

1) Fixed-interval trajectory

Segment-based trajectories come in two varieties: fixed-interval and variable-interval. In a fixed-interval trajectory, only one value determines the traversal time for all segments, hence a node takes the same amount to time to traverse every segment, regardless of the segment's length. In addition, a single value generally determines the altitude for all points. The *.trj file has following structure:

```
<coordinate_count>
locale: <locale>
<sample_time_step> <position_unit> <coordinate_method>
<x_coord_0>, <y_coord_0>, <alt_0>
<x_coord_1>, <y_coord_1>, <alt_1>
...
<x_coord_n>, <y_coord_n>, <alt_n>
```

2) Variable-interval trajectory

In a variable-interval trajectory, each point has its own specified altitude, wait time, traversal time (time from the previous point to the current point), and orientation. The wait

time causes a mobile object to pause at each point before it begins traversing the next segment. The *.trj file for variable-interval trajectory has following structure:

```
Version: 3
Position_Unit: <position_unit>
Altitude_Unit: <altitude_unit>
Coordinate_Method: <coordinate_method>
locale: <locale>
Calendar_Start: <start_time>
Coordinate_Count: <coordinate_count>
# X Position ,Y Position ,Altitude ,Traverse Time, Wait
Time, Pitch, Yaw, Roll
<x_coord_0>,<y_coord_0>,<alt_0>,<trav_time_0>,<wait_time
_0>,<pitch_0>,<yaw_0>,<roll_0>>
<x_coord_1>,<y_coord_1>,<alt_1>,<trav_time_1>,<wait_time
_1>,<pitch_1>,<yaw_1>,<roll_1>>
...
<x_coord_n>,<y_coord_n>,<alt_n>,<trav_time_n>,<wait_time
_n>,<pitch_n>,<yaw_n>,<roll_n>>
```

3) Relative movement

Because the mobile nodes can be nested (e.g. a mobile node within a mobile sub-network), the movement of the parent subnetwork can affect the movement of the child node. It must be considered when the segment-based trajectories are created. The effect on movement is as follows [6]:

- If the child node's position units are degrees, movement is considered in an absolute sense relative to the earth. Parent subnetwork movement has no effect on the child node.
- If the child node's position units are non-degree (such as meters or feet), movement is relative to the parent subnetwork. Thus, if the parent subnet is moving east at 10 meters per second (m/s) and the child node within it is moving west at 5 m/s, the motion of the node with respect to the earth is 5 m/s east.

4) Defining segment-based trajectories

The segment-based trajectory can be created and assigned manually in OPNET Modeler. The procedure for defining a trajectory varies slightly depending on whether the trajectory uses fixed intervals or variable intervals.

B. Random trajectory

Trajectories and orbits specify deterministic paths for mobile nodes. Random trajectory is defined by a rectangular region in which a node will move during a simulation. This region is specified by x-y coordinates or by using a mobility domain. During simulation, the node randomly selects a destination in the region and moves toward it at a specified or randomly chosen speed. Upon reaching its destination, the node pauses a configurable length of time before it repeats the process by selecting another random destination [6].

C. Direct manipulation of position attributes

In addition to trajectories and orbits, OPNET Modeler users can model movement of mobile sites by directly manipulating position attributes. If a trajectory is specified for a mobile node, the path of that site is predetermined for the entire simulation. However, if no trajectory is specified, the node's position can be directly updated by any process during simulation. A mobile node's x position and y position

attributes specify its location in its parent subnetwork. A mobile node's altitude attribute specifies its elevation relative to sea level, the underlying terrain, or the parent subnetwork (depending on the site's altitude modeling attribute setting). A change to one of these attributes will cause an immediate change in the location of the mobile site [6].

Typically, one of two techniques is employed to dynamically change the location of a mobile node. In both cases, a user-defined process is responsible for modifying the position attributes of a mobile node. The first technique is a centralized approach, in which one process is responsible for updating the positions of all of the mobile nodes in a network model. The second technique is a decentralized approach. In the sense that each mobile node has a process executing within it that updates only its own position [6].

III. GPX AS INPUT DATA

The real path is obtained using the GPS (Global Positioning System) system and stored in the GPX (GPS eXchange Format) file subsequently. This file type can be captured from the navigation device or online maps servers. This GPX file with defined path is passed to the OPNET Modeler environment, where it is converted by special functions into a format that meets the requirements of OM for movement control.

A. GPX file format

The GPX file format is based on XML (eXtensible Markup Language), which means that the file contains predefined tags to represent the whole trajectory [7]. The structure of a GPX file format is described in Table I.

TABLE I
STRUCTURE OF THE GPX FILE FORMAT

XML Element	Description
<?xml version="1.0" standalone="yes"?>	File header placed at the beginning of the document.
<gpx>	Tag identifying GPX files.
<trk>	Tag representing a track.
<trkseg>	Tag containing the list of points representing the track.
<trkseg lat="49.5684025" lon="14.0124586" >	Tag containing the GPS coordinates of the point.

1) Haversine formula

One of the most important operations during the conversion of a GPX file to an OPNET Modeler trajectory file is to calculate the distances between two consecutive points of the track. This calculation is realized according to the mathematical equation called haversine formula [8]. This formula is defined as:

$$haversin\frac{d}{R} = haversin(\varphi_1 - \varphi_2) + \cos(\varphi_1) + \cos(\varphi_2) + \cos(\Delta\lambda), \quad (1)$$

where

- *haversin*() is the haversin function:

$$haversin(\theta) = sin^2\left(\frac{\theta}{2}\right) = \frac{1-\cos(\theta)}{2} \quad (2)$$

- *d* is the distance between two points,
- *R* is the diameter of the Earth,
- φ_1 is the latitude of the first point,
- φ_2 is the latitude of the second point,
- $\Delta\lambda$ is the difference in longitude of two points.

IV. Implementation of Online Conversion Tool

Detailed knowledge of both formats (GPX and TRJ) taking part in conversion is compulsory, as well as painstaking validation of perfection of the conversion process. At first, a web interface was developed for conducting this process. This interface was capable to operate with desired formats and provided more comprehensible environment than OPNET Modeler.

The first stage of the work was accordingly focused on implementing an application for conversion of GPX files to TRJ format which is supported by OM for the sake of insertion and testing of a real trace within OM environment. As for technological solution, the simplest approach has been chosen. The entire system is designed as a web application. The basic architecture of this application is shown in Fig. 1.

The user interface was programmed using plain HTML (HyperText markup Language) without any additional libraries or frameworks. For mere input validation was used simple JavaScript. The very conversion and parsing is conducted on the server side. UI provides options for choosing a file to be converted and uploads this file to the server where all the necessary operations are performed. A technology of PHP (Hypertext Preprocessor) was used to develop the server side of the application.

PHP scripting language was chosen for several reasons. GPX files are based on XML (eXtensible Markup Language) language and are practically identical. SimpleXML libraries were used for the reason of being supported by majority of contemporary webhosting providers. This means that no required installation or additional libraries, which results in simplification of development of the application. Another reason may be an extension like Google Maps API or any other map basis that may stand for data source in hypothetical extension of the application, as well as viewing a trace stored in a GPX file. At least but not last, in case of emplacement on public web page, the application could be available to all Internet users.

A. PHP Scripting Language

The PHP (Hypertext Preprocessor) is a widespread multipurpose scripting language. Especially, it is used for web application development, so it consequently supports an encapsulation into HTML. When used with dynamic web pages, scripts are being processed at server side and mere results of this process are transmitted to the target browser.

B. JavaScript

The JavaScript is multiplatform object-oriented scripting language. It is used, nowadays, mostly as programming language for web pages. Its code is often inserted directly into HTML code of a page. JavaScript usually controls interactive elements like buttons or special text fields, or can be used for creating animations and image effects.
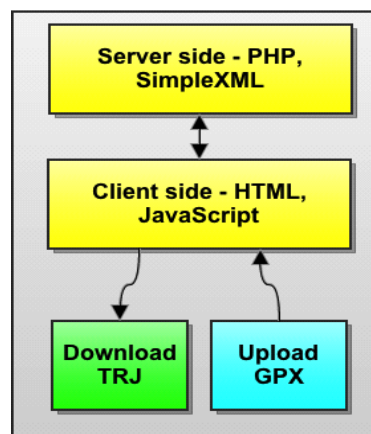

Fig. 1. Conversion application architecture

Word Java in the title of this language is of mere marketing character, though, and the language itself has nothing in common with the Java language besides similar syntax.

Unlike the other programming languages (e.g. PHP or ASP), JavaScript code is usually processed after the page is loaded in a browser (i.e. at the client side). This fact results in several security restrictions for protection of user's privacy. For example, JavaScript cannot process files stored on the disk [11].

C. Conversion Interface

Individual inputs of the application are controlled by JavaScript so that only a number can be inserted and a blank value is invalid. In a case when user disables JavaScript in his web browser, the inputs are subsequently checked by PHP as well. The graphical user interface of the application is shown in following Fig 2.

In the first stage, the application loads selected file and validates its appendix (must be .gpx). Size of the file is checked afterwards. Its maximal value is set for 10MB. The file is subsequently stored at the server side in a directory named gpx. Further, the file is loaded by function simplexml_load_file. This function converts the file into an object in memory. This step also includes validation of structure of the file, whether it corresponds with XML/GPX standards. With these requirements fulfilled, the object stored in memory is searched for an element <trkpt>. This element contains parameters of geographical latitude and longitude. These parameters are then stored in one field. If the object contains further information about time or altitude, these data are stored in the field as well. After storing all points of the track into the field, a count of these points is computed. Furthermore, if background is set on Campus, values in the field are converted from angular coordinates to coordinates of selected background. With a check button Center checked, a center of the trace is placed exactly into the middle of the coordinate system.

A new file *trajectory.trj* is created subsequently in a directory called export. A header is inserted into this file according to chosen metrics of the trace and to the count of trace points computed earlier. After this import, the field containing coordinates, time and altitude is read and the values are written into the file in a format specific to TRJ files.

During the last stage the old file from the *gpx* directory is deleted and the new TRJ file is available to download.
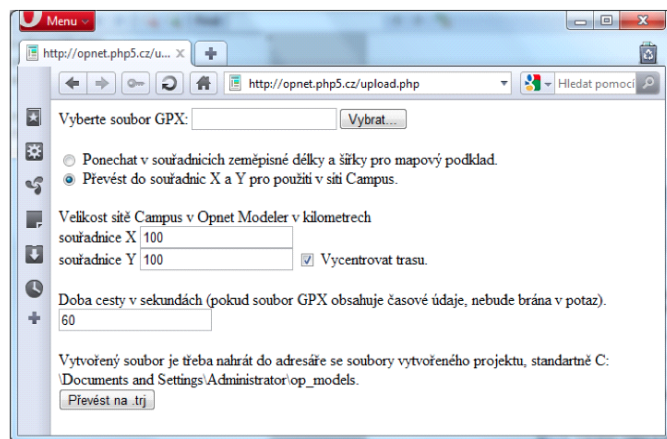

Fig. 2. Conversion application – graphical user interface

V. GPX TO TRJ CONVERSION IN OPNET MODELER

The C/C++ programming language can be used in OPNET Modeler to implement new and modify existing functions. All functions related to the work with GPX format have been stored in the *gpx.h* header file. Using the *#include "gpx.h"* command this header is inserted to the Header Block of the process model created in OPNET Modeler [6].

The coordinates obtained from the GPX file are stored in a structure containing 4 parameters, as it is shown in the following fragment of source code. The first two parameters (latitude and longitude) represent the location, the third parameter defines the altitude and the fourth parameter stores the timestamp.

```
struct coordinate {
        double longitude ;
        double latitude ;
        double altitude ;
        int time ;
};
```

The first step of converting a GPX file to a TRJ format is loading the GPX file from the given directory. Next the file must be opened for reading and processed by a XML parser, e.g. by functions available in the TinyXML library. The data obtained will be inserted into a vector. In our model this process is realized by the *CoordToVector* function:

```
vector < coordinate > CoordToVector ( char gpx_file
[128] , bool isTimeMan, double timeMan , double speed ,
bool * err )
```

This function is directly called from the process model. The input parameters of the function are the following:

- **gpx_file** – the name of the GPX file which has to be loaded.
- **is_time_manual** – a flag, which takes value 1 if the time is configured manually via model attributes or 0 if the time is obtained directly from the GPX file.
- **travel_time_manual** –manually defined time value, entered via an attribute of the model.

- **speed** - manually defined speed of movement, entered via an attribute of the model.
- ***err** – a pointer type flag, which takes value 1 if an error occurs during the process, i.e. if the file with given name is not present or if the format is not supported. Consequently this flag terminates the simulation in the process model, as it is described later.

By executing the CoordToVector function, it creates a vector of coordinate structures, defined earlier.

```
Vector< coordinate > v;
```

This vector is the return value of the CoordToVector function and contains the coordinates of each point together with its altitude and timestamp. In the next step the vector is converted into a TRJ format. This conversion is provided by the GPXtoTRJ function.

```
void GPXtoTRJ ( char site_name [128] , vector <
coordinate > v , bool * err )
```

The input parameters specify the vector of coordinate values and the name of the target TRJ file. First, the header is inserted into the file. Next the input vector is processed step by step and the values calculated are entered into the TRJ file. The timestamp of the first entry equals to 0. The timestamp of the following entries equals to the difference between the timestamp of the current and previous entry.

The TRJ file also contains information about the total number of coordinates. This parameter is required during the configuration of a mobile node in the OPNET Modeler environment. The total number of coordinates is determined by the CountFunc function:

```
int CountFunc ( vector < coordinate > v ),
```

which is called by the vector of coordinates as an input argument. Additionally, the length of the whole trajectory is calculated. This calculation is provided by the *DistanceInMeters* function:

```
double DistanceInMeters ( const coordinate & from ,
const coordinate & to )
```

This function returns a value of type double, which contains the length of the whole track in meters. The distance is calculated according to the haversine formula introduced in section 3.

VI. SIMULATION PROCESS IN OPNET MODELER

Firstly, it is necessary to set up the simulation environment after the implementation of functions for the conversion of GPX file into TRJ file. The first step is the import of designed functions into environment. This process is important and allows using new functions during the simulation process. The next step is the design of simulation scenario, in which nodes trajectory will be changed according to GXP file.

A. Set up OPNET Modeler simulation environment

All necessary functions for the conversion of GPX file into TRJ file are implemented in header file called gpx.h. The OPNET Modeler simulation environment can read standard header files from this location:

```
\{INSTALL_DIR}\{OPNET_VERSION}\models\sd\include
```

Therefore, the gpx.h file can be stored into this location or a folder, which contains the gpx.h file, can be linked into simulation environment through the menu item Edit-Preferences-Compilation Flags for All Code. This menu item contains:

```
/ W3 / D _ C R T _ S E C U R E _ N O _ D E P R E C A T E
/ IC :\ {INSTALL_DIR} \ {OPNET_VERSION} \ models \ std \
include
```

To add another record, it is necessary to modify the menu item. The value PATH_TO_FOLDER will be replaced by real path to folder, which contains gpx.h file. This modification defines another search path for header files.

```
/ W3 / D _ C R T _ S E C U R E _ N O _ D E P R E C A T E
/ IC :\ {INSTALL_DIR} \ {OPNET_VERSION} \ models \ std \
include / IC : \ {PATH_TO_FOLDER}
```

B. Initial configuration of simulation scenarios

Firstly, a new project has to be created in OPNET Modeler. The creation of the mobile node's model is the necessary step. This node's model can by obtained by duplicating the default model. The duplicated model of mobile node was modified and extended for ability to manage its own trajectory, which depends on the GPX file. The duplication of mobile node's model is necessary, because the modification of the existing mobile node's model would be reflected in all applications of this model, i.e. in other independent simulations.

The duplicated mobile node's model is extended by new processor, which is called Mobility. This processor is based on standard processor called Sink, which contains two states - Init (forced) and Discard (unforced), see Fig. 3.

C. Extended attributes of mobile node

In the OPNET Modeler environment, it is possible to extend existing objects attributes by new custom attributes. The aim is to manage nodes movement by the route defined in GPX file, therefore it is necessary to extend the node's attributes by few new attributes:

- **GXP File** - specifies the name and path of GPX file which defines the route.
- **Manual Time** - the time can be entered manually (enable) or can be used from GPX file (disable). If this attribute is disabled and GPX file does not contain information about time, then the time 1s is used for a transition from one point to another.
- **Travel Time** - total time (in minutes) required for completion of the journey.
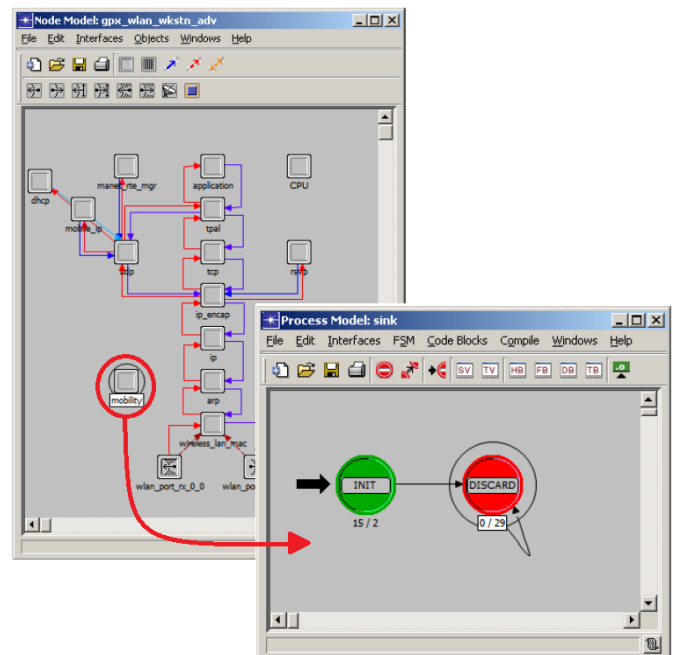
Fig. 3. Mobility processor and child process model

- **Speed** - speed of movement in km/h.
- **Generate TRJ** - if this attribute is enabled, TRJ file is created during simulation, which can be displayed in OPNET Modeler environment or it can be reused for another simulation process. If value is set up to disable, TRJ file is not created.
- **Movement Report** - determines whether the reports about mobile node's movement will be displayed in the OPNET simulation console.

These attributes can be set during the mobile node configuration in user interface part of OPNET Modeler or can be set by program during the simulation process. New attributes can be seen in Fig. 4.
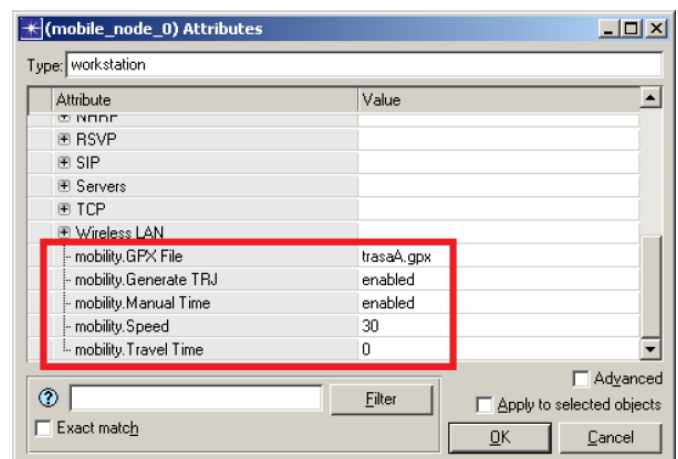
Fig. 4. New defined attributes for mobile node

D. Extending process model

The process model described above was based on a standard process model called Sink. The Sink process model is not

suitable for a trajectory management, therefore the Sink process was extended by an unforced state called Coordinates. It can be seen in Fig. 5.

1) INIT state

The INIT state is an initial state in every process model in OPNET Modeler environment. This state contains operations to get node identifier (ID), nodes attributes and to set coordinates vector.

```
my_obj_id = op_id_self();
parent_obj_id = op_topo_parent(my_obj_id);
op_ima_obj_attr_get (my_obj_id , "gpx file", site_gpx);
…
mymap[parent_obj_id]=CoordToVector(site_gpx, time_manual
,travel_time , speed , &err );
distance = PathDistance ( mymap [ parent_obj_id]);
count = CountFunc(mymap[parent_obj_id]);
GPXtoTRJ (site_name, mymap[parent_obj_id], &err);
```

At first, an ID of the Mobility process is loaded using *op_id_self()* function. After that is loaded an ID of the parent process. Subsequently, appropriate attributes of the mobile node are loaded using function *op_ima_attr_get()*. In the example above there is only a sample showing loading of the gpx attribute. Other attributes are loaded similarly. Function *CoordToVector()* is called afterwards. It fills the *mymap* vector with coordinates. Following functions determine length of the loaded route and count of coordinates of the entire route.

If the attributes of the node are set to create TRJ file, fiction *GPXtoTRJ()* is called. Its output is a TRJ file, which is located in the project folder. After performing all tasks program transits into the Coordinates state.

2) COORDINATES state

This state browses the vector of coordinates that was created in the INIT state. These coordinates are assigned to the mobile node. Assignment of individual coordinates is performed by the function called *op_ima_obj_attr_set_db1():*

```
op_ima_obj_attr_set_dbl ( parent_obj_id , "x position ",
mymap[parent_obj_id][i].longitude);
```

In the case where the time value is loaded from the GPX file, calling the function *TimeDiffFunc()* is necessary:

```
timeD [ parent_obj_id ] += TimeDiffFunc (i, mymap [
parent_obj_id ]);
```

The function mentioned above returns a difference of times between two points. The acquired time value is incremented into the *timeD* variable at each pass through the *Coordinates* state. In the case where the time value is set manually through station's attributes, the *timeD* value is acquired differently.

```
timeD[parent_obj_id] += mymap[parent_obj_id][i-1].time;
op_intrpt_schedule_self(timeD[parent_obj_id], 0);
```

The function *op_intrpt_schedule_self()* is a standard function of the OPNET Modeler environment. It performs an interruption of the state at the very time that is saved in the *timeD* variable. This results in mobile node's transition to the desired location at the requisite time. This procedure repeats until there are no coordinates available.

3) DISCARD state

This state performs actions associated with terminating functions of the process model and thus terminating the superior Mobility processor element. From the simulation point of view, the DISCARD state provides termination of station's movement.
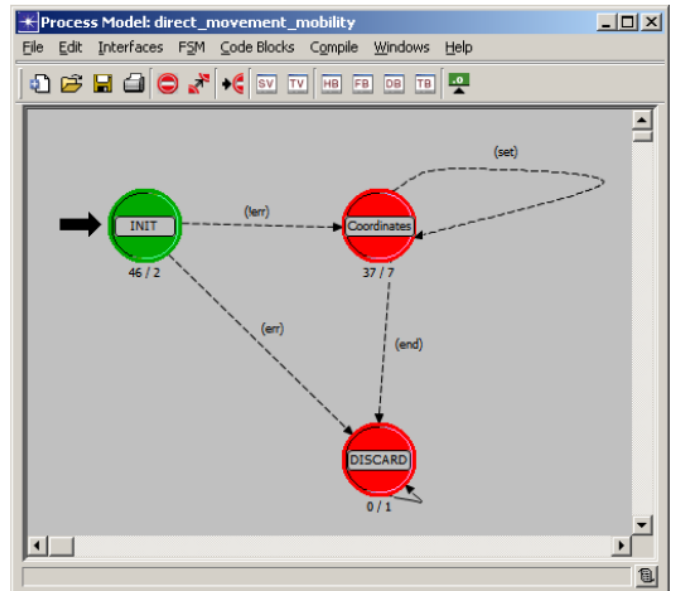
Fig. 5. Process model direct_movement_mobility

VII. ANALYSIS OF THE SIMULATION RESULTS OBTAINED

The simulation was performed for two mobile nodes. Each mobile node obtained slightly different settings. The adapted model, supplemented with the new Coordinates state and process parameters, was used as the mobile node's model. Settings of parameters of individual mobile nodes correspond to the following Table II.

TABLE II
PARAMETERS OF INDIVIDUAL MOBILE NODES

Attribute	mobile_node0	mobile_node1
GPX file	traceA.gpx	traceB.gpx
Generate TRJ	enabled	disabled
Manual Time	enabled	disabled
Speed	20	0
Travel Time	0	0

The OPNET Modeler environment contains an advanced debugger that allows observation of chosen simulation parameters, simulation progress control and display an animation of individual object's movement. The movement animation is an essential simulation parameter. It allows monitoring of the mobile node if it follows the trace that was defined in the GPX file assigned (see Fig. 6).
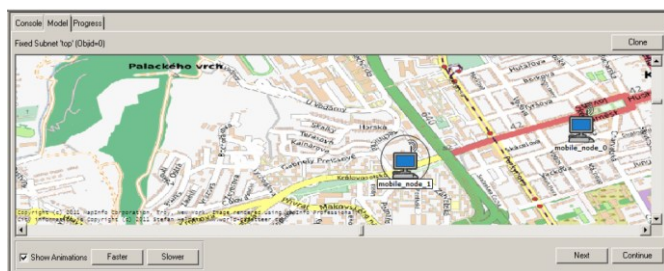
Fig. 6. The sample of mobile node's movement around the map background based on a trajectory defined in a GPX file

VIII. CONCLUSION

In the beginning, the paper states options of station model's control in the OPNET Modeler environment. Particularly, a TRJ file and its structure is essential. The file provides trajectory control and the possibility of moving the station using direct manipulation of the attributes. The next part of the paper deals with implementation of functions for a real trajectory simulation. All these functions are implemented in an individual file and create an interface between the GPX file defining a real trajectory and the OPNET Modeler environment. This system enables to control movement of a station around a real trajectory. This was impossible in the OM until now. It is possible to use more fractional GPX files for a trajectory definition. The functions defined in the OM are loading fractional files and connecting indiv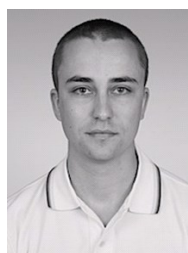idual trajectories into one continuous trajectory. The station moves around the resultant trajectory, then. This solution brings new opportunities for network simulations to get closer to the real environment.

REFERENCES

[1]   ILLYAS, M. The Handbook of Ad Hoc Wireless Networks, CRC Press, 2003.

[2]   BOUKERCHE, Z. Algorithms and Protocols for Wireless and Mobile Ad Hoc Networks, Wiley, 2009.

[3]   SKOŘEPA, M.; ŠIMEK, M.; MAHDAL, O. Mobile Ad-Hoc Network routing protocols - performance analysis. In Proceedings of the 32nd International Conference Telecommunications and Signal Processing. 2009. s. 1-4. ISBN: 978-963-06-7716- 5.

[4]   CAMP, T.; BOLENG, J.; DAVIES, V. A survey of mobility models for ad hoc network research. In Wireless Communications and Mobile Computing, 2002, vol. 2, no. 5, pp. 483-502.

[5]   HOŠEK, J.; MOLNÁR, K.; JAKÚBEK, P. Map-Based Direct Position Control System For Wireless Ad- Hoc Networks. In Proceedings of the 34th International Conference on Telecommunication and Signal Processing, TSP 2011. Budapest: Asszisztencia Szervezo Kft., 2011. s. 195-200. ISBN: 978-1-4577-1409- 2.

[6]   OPNET Technologies. OPNET Modeler Product Documentation Release 16.1 .2011.

[7]   FOSTER, D. GPX: the GPS Exchange Format, [online]. 2004. URL: http://www.topografix.com/gpx_for_developers.asp.

[8]   GIS FAQ Q5.1: Great circle distance between 2 points, [online]. 2010. URL: http://www.movable-type.co.uk/scripts/gis-faq-.1.htm.

[9]   PHP: Preface - Manual [online]. 2010. URL: http://cz.php.net/manual/en/preface.php.

[10] Hrebenar, Jiří. SimpleXML - jednoduše na XML v PHP 1.díl [online]. 2009. URL: http://programovani.blog.zive.cz/2009/12/simplexml-jednoduse-na-xml-v-php-1dil.

[11] About JavaScript - MDC Doc Center [online]. URL: https://developer.mozilla.org/en/JavaScript/AboutJavaScript.

Pavel Vajsar completed the Master degree at Faculty of Electrical Engineering in Communications and Informatics specialization in Brno University of Technology. He is currently 4th-year postgraduate student at the Department of Telecommunications of the same faculty. His research work has been concentrated on routing in MANET networks with regard on quality of services. Recently he has also been concerned with wireless sensor networks and developing of application for monitoring of these networks.

Jiri Hosek received the B.S. and M.S. degrees in Electrical Engineering from Faculty of Electrical Engineering and Communication at the Brno University of Technology in 2005 and 2007, respectively. He is currently an assistant professor at the Department of Telecommunications of the Faculty of Electrical Engineering and Communication at the same university. His research work has been concentrated on the design of new communication protocols and services for the wireless networks.

Milan Bartl is currently a 3rd-year master student at the Department of Telecommunications of the Faculty of Electrical Engineering and Communication, BUT. His master thesis is focused on the issue of cooperation between external systems and simulation environmet OPNET Modeler and its utilization in QoS assurance area.

Karol Molnar received his MSc. degree in Electronics and Communications (1997) and Ph.D. degree in Teleinformatics (2002) at Brno University of Technology (BUT), Czech Republic. He is with the Honeywell International, s.r.o. In his scientific work he focuses on modern network technologies, especially on topics of QoS support in both fixed and mobile network technologies. During the last several years he actively participates in theoretical and research works closely related to the technology of Mobile Adhoc Networks.

The Device for Low-Cost Measurement of 2D Thermal Distribution

Jiří Minář, Kamil Říha

Abstract—**The article describes a specialized device for measurement of thermal distribution of two dimensional surfaces for some applications in medical industry, and mechanical or civil engineering. The device is a substitution of expensive device for this kind of measurement is thermal camera which can be expensive for some application or should have the limitation of non-possibility to read temperature behind a barrier (wall, bandage).**

The main goal of this work was to design a device for measurement of thermal distribution on 2D surface for low-cost measuring processes with slow change of temperature and for processes, which do not require high resolution of collected data. The next advantage of presented device is a possibility of temperature measurement behind the barrier.

Keywords— **2D Sensor Field, NTC, Temperature Measurement, Thermistor.**

I. Introduction

Nowadays, there are many methods of field temperature measurement available on the market. Most of these methods are designed for a non-contact measurement e.g. two-dimensional infrared spectroscopy [1], three-dimensional temperature measurement of water using two-color laser-induced fluorescence (LIF) [2] or CCD (Charge-Coupled Device) or ICCD (Intensified Charge-Coupled Device) sensors [3]. Nevertheless, this kind of measurement device could be expensive for some application or there could be also disadvantage of impossibility of measurement temperature behind the barriers. The most common device, which is used for 2D temperature field measurement is infrared thermo camera, which can be bought from $2000. This can be expensive for some application. Therefore, a low-cost device for these types of measurement is sought. As a basic element for such device simple and cheap sensor: NTC thermistor (Negative Temperature Coefficient) was selected. This sensor is passive electronic component based on conversion of temperature to resistance [4]. The dependence of the resistance of typical thermistor is

$$R_T = Ae^{\frac{B}{T}},\qquad(1)$$

Jiri Minar is with Dept. of Telecommunications, Faculty of Electrical Engineering and Communication, Brno University of Technology, Purkynova 118, 612 00 Brno, Czech Republic,
mail: xminar15@phd.feec.vutbr.cz.

where R_T is resistance, A is a constant based on geometrical shape and material of thermistor, B is temperature constant based on material of thermistor, and T is thermodynamic temperature.

NTC thermistor has exponential temperature/resistance characteristic. And measurement results can be very imprecise without elimination of this non-linearity. This can be solved with a lookup table (see Chapter IV.) or by inversion function.

As a minimal size of the 2D temperature field is used sensors matrix with 8 x 8 sensors. This size should be sufficient for practical verification of the solution.

II. Sensor Characteristics

A. Thermistor

There is a big variety of NTC thermistors on the market with different size, different toleration or mounting technology, and the price range is from $0.1 to $5 per sensor.

For experimental device NTC thermistor, form company Betatherm with type number SMD110KJ375J was chosen. Its parameters are described in Table I. This thermistor is built for SMT - Surface Mount Technology. The size of the thermistor is very small (3.2 mm × 1.6 mm) therefore is suitable for building big sensors array and the price of this sensor is suitable for low cost application. It is about $0.3 per sensor.

TABLE I
BETATHERM SMD110KJ375J

Parameter	Value
Operation temperature	- 40°C to + 120°C
Max. load	400mW
Resistance at 25°C	10kΩ
Tolerance	5%
Dissipation Constant	3mW/°C

B. Thermistor Characteristic

All the sensors used in the two-dimensional field should have the same exponential characteristic. Same exponential characteristic is expected for all thermistors of the same type. The only error in offset is expected, which is given by 5% tolerance of the thermistor, which can be easily removed only adding or subtracting offset value. This can be solved by implementation into look up table together with linearization of exponential characteristic of thermistor. The shapes of exponential functions of thermistors are same on

considered temperature operation range (25°C to 50°C). As is seen in Fig. 1, where is the example of two NTC thermistors used in measurement device.
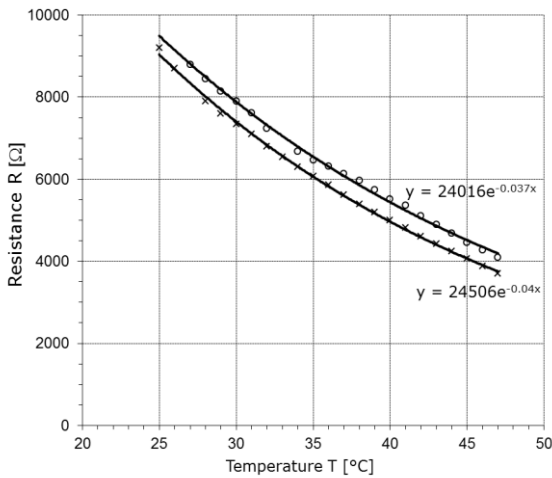

Fig. 1. Example of two NTC thermistors characteristic $R = f$ (T) with constant current 50µA

Measurements of two thermistors were performed in oil fluid, where oil was heat up to 50°C and then temperature decrease from 50°C to 25°C. Cool down of thermistor was approximately 1°C per 15 seconds. As can be seen from Fig. 1, that temperature is out of tolerance in 25°C, but this is cause by thermal accumulation of thermistor. Resistance was in tolerance after approx. two minutes. And the values of thermistor were stabilized on values 10100 Ω and 10180 Ω, which is 5% tolerance.

III. DEVICE REALIZATION

A. Wheatstone Bridge

Value of Temperature on sensor is value of resistance of thermistor; therefore temperature is measured indirectly by measuring of voltage. Very good application of this type of measurement is connection of thermistor into Whetstone bridge with differential amplifier (Fig. 2).
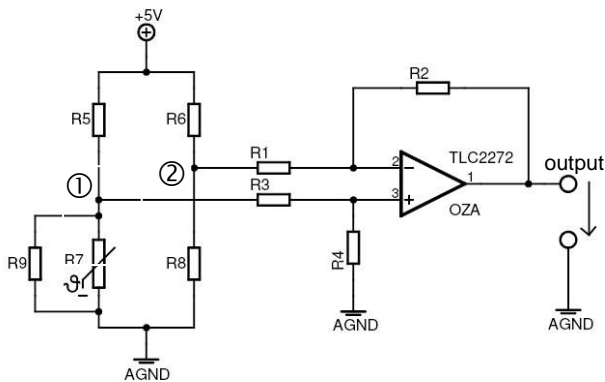
Fig. 2. Wheatstone bridge with parallel connection of thermistor

Device was designed for precision 0.1°C and for measuring temperature range from 25°C to 45°C. These parameters were chosen specifically for one of possible use

of this device; measuring of skin temperature.

Values of resistance of Wheatstone bridge were designed for mentioned parameters (R_7 = 5 kΩ − 10 kΩ parameters of thermistor from Fig. 1) and for precision 0.1°C (max. current I_{max} = 300 µA).

Bridge is balanced in measurement points' ① a ②   in Fig. 2. Values of resistors R_5, R_9 are designed to reflect maximum of value of measurement current. Then there are $R_5 = R_6$ = 50 kΩ, and $R_8 = (R_7$ in parallel combination with $R_9) = 2200$ Ω. Resistance R_9 is added for linearization exponential characteristic of thermistor [4].

Amplifier was chosen TLC2272 from company Linear Technology. This amplifier is of rail-to-rail type (can produce output voltage V_{out} very close to supply voltage V_{cc}. Resistances for setting of differential amplifier were set on these values: $R_1 = R_2$ = 5 kΩ a R_3 = 26 kΩ.

Values of resistors were verified in program PSpice that current through thermistor is not higher the I_{max} (Fig. 3).

Based on toleration analysis of resistors in program PSpise, possible influence of toleration of resistors on temperature error was verified. Resistors R_1 - R_4 are not too sensitive to precise value of resistors (Fig. 4).
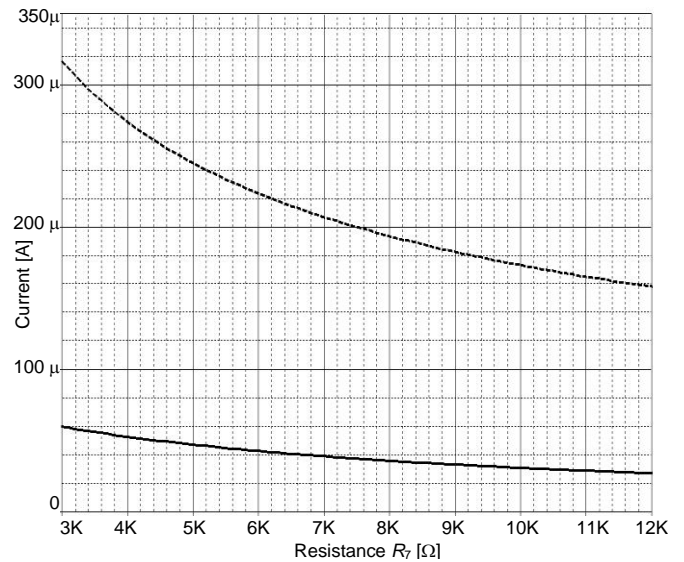
Fig. 3. Current through thermistor R_7
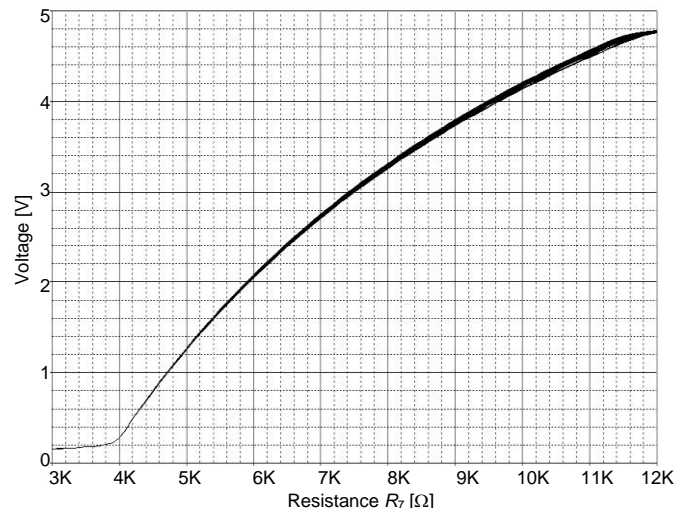
Fig. 4. Toleration analysis for resistors R_1-R_4 with tolerance 1 %

Fig. 5. Toleration analysis for resistors R_5-R_7 and R_9 with tolerance 1% - 25 runs

But resistors $R_5 - R_7$ inside the Wheatstone bridge have to be selected from series with very low tolerance (Fig. 5). Because resistors with 1 % tolerance can cause additional offset error, this means 8°C error. For practical realization should be selected resistor from series with tolerance 0.5 % or better or instead of resistor R5 use trimmer for weighting of Wheatstone bridge.

B. Controlling of Sensor matrix

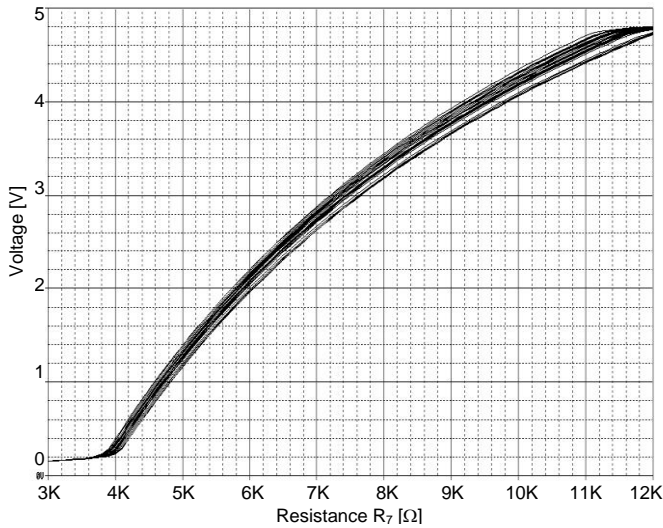Matrix of sensors has been designed as square matrix with 8 x 8 sensors, therefore switching method was chosen for 64 sensors as an individual connection of thermistors into differential amplifier by multiplexer MC14067B from company ON Semiconductor. This connection ensures that current measurement goes through single switched thermistor (Fig. 6). All thermistors are connected to the ground and only one thermistor is selected. Used multiplexer handle serve 16 sensors, therefore 4 multiplexers have to be used.
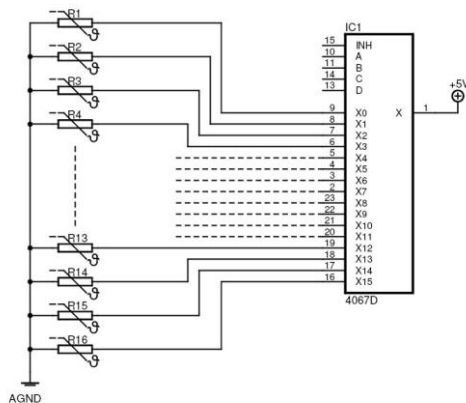
Fig. 6. Switching of thermistor by multiplexer

For controlling and communication with PC microcontroller ATMEL ATmega16 was used. This controller provides necessary functionality for A/D conversion and communication. A/D convertor used in ATmega16 has 10-bits resolution and this is enough for temperature range 25°C – 45°C with toleration 0.1°C,

because change of one bit means that this range is change of 0.02°C.

IV. EXPERIMENTAL RESULTS

Due to exponential characteristic of thermistor and offset of thermistor by 5 % toleration, it is essential to calibrate every sensor at whole range of temperature. Exponential characteristic can be linearized by inversion function from eq. (1) or by lookup table. Lookup table was selected due to its modesty to compute power and also for calibration of offset.

For 0.1°C precision on all temperature range it is necessary to divide whole range at least to 20 intervals, as is seen in Fig. 7. Each interval is considered as linear.

Calibration should be essential, because non-calibrated sensors can have temperature up to 1°C. Fig. 8 shows a situation for 3 examples of calibration. First curve considers only 3 calibration points and due to this the temperature error between two these points can be up to 0.9°C. Second curve demonstrates 5 points calibration with temperature error up to 0.4°C. And the third curve demonstrates sufficient calibration with 23 points and there is temperature error below 0.1°C. This calibration should be done in temperature chamber with suitable temperature range and with step 1°C per 2 minutes to ensure sufficient heat of thermistor.
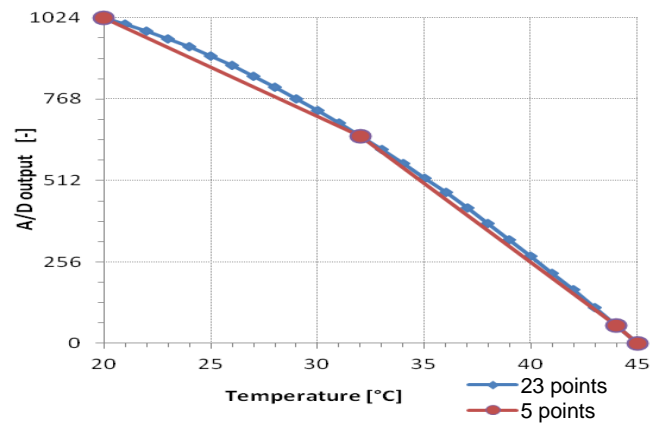
Fig. 7. Conversion characteristic Sample/Temperature for 3-point and 23-points calibration
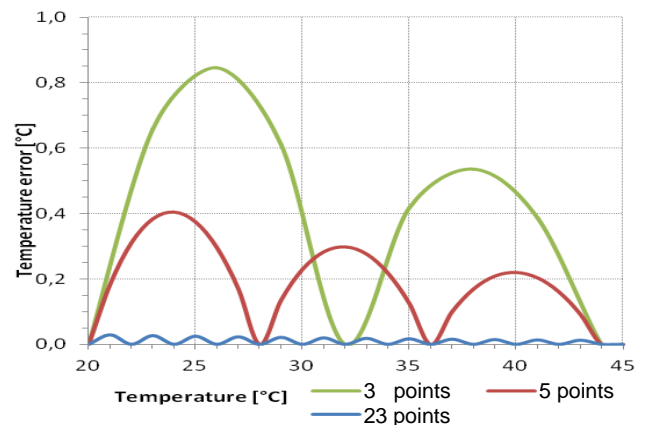
Fig. 8. Temperature error for 3-point, 5-points and 23-points calibration

a) 8 x 8	b) 15 x 15	c) 29 x 29	d) 64 x 64

$i = 0$	$i = 1$	$i = 3$	$i = 7$
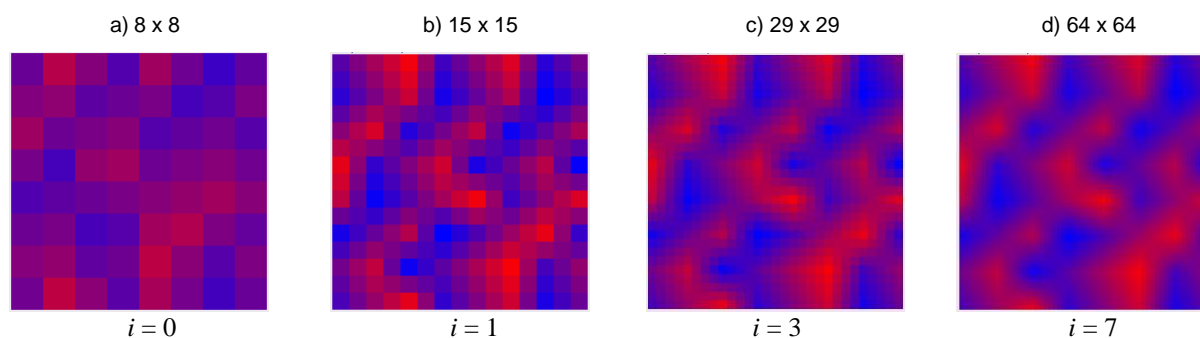
Fig. 9. Interpolation of measurement data – interpolation coefficient i

Visualization of measured values was done as temperature map in PC, where the lowest temperature (25°C) is of blue color, the highest temperature (45°C) is red color and the temperatures between the temperature range have the relevant colors from blue – red color range Fig. 9(a) Interpolation from 1 to 7 was used for better interpretation of measured field Fig. 9(b), Fig. 9(c), and Fig. 9(d), where value interpolation coefficient i defined amount of computed values was added between two measured values.

In Fig. 9, there is sample of measured data as a temperature footprint of three fingers as is described in Fig. 10.
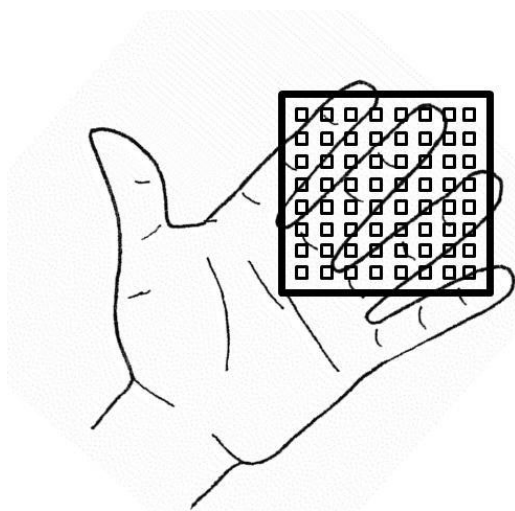
Fig. 10. Experimental measurement of three fingers with matrix of 8 x 8 of thermistors

## V. CONCLUSION

The solution for low cost measurement device based on matrix of NTC thermistor was presented. This device should be used as a cheap substitution of common method of measurement of thermal two-dimensional field e.g. infrared thermo-camera. The proposed solution has price about $30comparing with price of infrared thermo-camera (starting at $2.000) is much cheaper. For some application could be advantage that this device could be placed behind solid barrier. This device can be used for measuring the temperature field with slow change of temperature (minutes) and where is not necessary detailed resolution. Relevant application of this solution could be in medical use as e.g.

mechanical industry, where the big distance between the sensors is not a problem.

REFERENCES

[1] Isao Noda, "*Two-Dimensional Infrared (2D IR) Spectroscopy* Theory and Applications," Appl. Spectrosc. 44, 550-561 (1990)

[2] J. Sakakibara, R. J. Adrian , *Whole field measurement of temperature in water using two-color laser induced fluorescence* , Experiments in Fluids, Volume 26, Issue 1-2 , pp 7-15, 1999

[3] J. Lindén, C. Knappe, M. Richter and M. Aldén*, Precision in 2D temperature measurements using the thermographic phosphor BAM*, Measurement Science and Technology, Volume 23, Number 8, 2012

[4] Kreidl, Ml. *Měření teploty: senzory a měřicí obvody*. 1. vyd. Praha, BEN, 2005. 240 s. ISBN 80-7300-145-4.

Jiri MINAR received BSc. at the Department of Telecommunications at the Faculty of Electrical Engineering and Communication at Brno University of Technology in 2005. He received Ing. (MSc) at the same department in 2007. Now he is a PhD student at the same faculty. The area of his professional interests sensors and digital image processing.

Kamil RIHA received his M.Sc. degree in Electronics & Communication in 2003 and the Ph.D. degree in 3D Scene Acquisition for Auto-Stereoscopic Display in 2007. Presently, he is employed at Brno University of Technology, Faculty of Electrical Engineering, Department of Telecommunications, as the academic employee (since 2006). His research interests include in particular areas of digital image processing and electronics.

Suitable Image Intensity Normalization for Arterial Visualization

Yara Omran, Radek Benes, Kamil Riha

Abstract—**Ultrasonic imaging is a widely used non-invasive medical imaging procedure since it is economical, comparatively safe, portable and adaptable. However, one of its main weaknesses is the poor quality of images, which makes the enhancement of image quality an important issue in order to have a more accurate diagnose of the disease, or for the transformation of the image through telemedicine channel and in many other image processing tasks [1]. The purpose of this paper is to automatically enhance the image quality after the automatic detection of the artery wall. This step is essential before subsequent measurements of arterial parameters [9]. This was performed automatically by applying linear normalization, where results showed that normalization of ultra sound images is an important step in enhancing the image quality for later processing. In comparison with other methods, our method is automatic. The evaluation of image quality was done mathematically by comparing pixel intensities of images before and after enhancement, in addition to a visual evaluation.**

I. INTRODUCTION

Ultrasound imaging (sonography) uses high-frequency sound waves to view soft tissues such as muscles and internal organs. Since ultrasound images are captured in real-time, they can show movement of the body's internal organs as well as blood flowing through blood vessels. But the complex nature of sound transmission and reflection in anatomical structures causes the medical ultrasound images to contain many artifacts. We can mention the most common artifact such as:

- speckle noise: which results in image degredation and reduction in contrast resolution.
- Shadowing: when the beam encounters an interface of highly different acoustic impedance, a large proportion of it is even reflected or absorbed, so only little remains to travel into deeper tissues and produce echos, this reduction in the beam's intensity appears as shadow in the image.
- Scattering: Scattering happens especially when the beam meets a very small object or a rough surface, so the echos are scattered in all directions in a non-uniform manner instead of being reflected back to the probe.
- Blood backscattering: The flow of blood in arteries causes aggregation of blood cells moving in the lumen following the bloodstream. Blood clots would be detectable as hyper-echogenic fixed spots in the ever moving bloodstream which makes the lumen appear brighter than it

should be (ideally, the artery should appear as a black strip (the lumen) surrounded by bright lines (the walls)). this artifact puts a big challange on the measuring of the LI boundary. Normalization is a good way for reducing the problem of backscattering [4].

These drawbacks and many others the improvement of ultrasound iamges'quality an important need. The goal is to achieve an image with a good quality that allow to take measurements of static and dynamic parameters of the artery, such as lumen diameter LD, artery stiffness (AS), intima media thickness IMT, the results of such measurements can be used for the prediction of patient's risk of cardio-vascular events. These days the measurements are still performed manually by experts and main efforts are paid to atomize them.

A. Anatomy of the artery

Blood vessels are usually composed of three layers: the tunica intima, tunica media, and tunica adventitia [3]. The outermost layer is known as the tunica externa formerly known as "tunica adventitia" and is composed of connective tissue and elastic fibers. Inside this layer there is the tunica media, which is made up of smooth muscle cells and elastic tissue. The innermost layer, which is in direct contact with the flow of blood, is the tunica intima, commonly called the intima. This layer is made up of mainly endothelial cells. The hollow internal cavity in which the blood flows is called the lumen [3]. Segmentation of the artery wall means automatically tracing the profiles of the most important interfaces: Lumen-Intima (LI), media-adventitia (MA) interface. For the measuring of IMT the longitudinal view is required [4] (for automatic measuring see [9]).

II. RELATED WORK

Much effort has been devoted to enhance the quality of ultrasound images, due to the importance of image quality in making later measurements of the artery more effective and robust. In [1], [2] manual algebraic normalization was used by linearly adjusting the image so the average gray level of the blood was 0-5 inside the lumen, and the average gray level of pixels on the artery wall was 180-190, in this work linear normalization and speckle reduction proved their efficiency [1]. However, this was all done manually. In our work, after the automatic detection of the artery, linear normalization was performed also automatically by automatic selection of a reference point inside the lumen and of another point on the adventitia, then applying linear remapping of intensity values between these two values following the same procedure mentioned above.
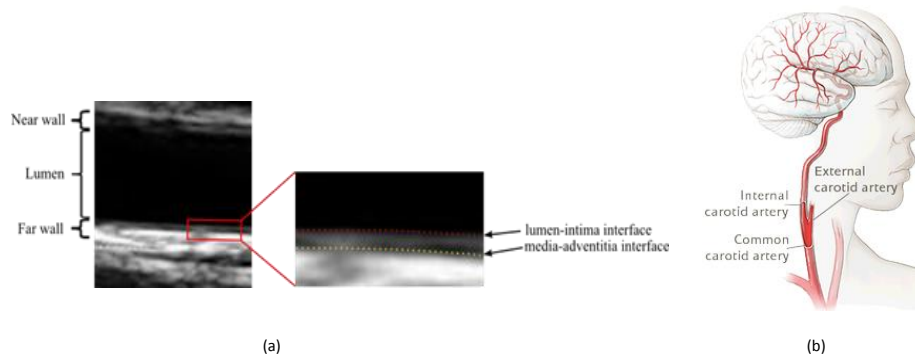
Y. Omran, R. Benes, and K. Riha are with the Brno University of Technology, Dept. of Telecommunications, Purkynova 118, 612 00 Brno, Czech Republic (corresponding author: yara.omran@phd.feec.vutbr.cz)).

Fig. 1: (a) B-mode common carotid artery ultrasound image (b) Anatomy of CA

III. Materials and Method

Our data base consists of 84 B-mode ultrasound images of the longitudinal view of the CCA (common carotid artery). CCA images were obtained with the patient lying down with the neck turned to the side. Images were acquired from 10 volunteers, with 8 images from each one with Sonix OP ultrasound scanner with deferent set-up of depth, gain, time gain compensation(TGC) curve, and deferent linear array transducers (frequencies 10MHzand, 14MHz). Images were not zoomed during scanning and also they were not cropped after the capturing.

After automatically detecting the arterial wall [9] and by analyzing pixels we can find two sets of points, points inside thumen $l(i)$ and points that are on the arterial wall $w(i)$. These sets of points were analyzied in order to find a suitable remapping function that will transfer the intensities into an appropriate interval. Intervals were chosen in similar way described in [1], [2], which implies that pixels' intensities inside the lumen will be transferred into the interval $\langle 0, 5 \rangle$, and those on the arterial wall should be in the range $\langle 180, 255 \rangle$. The intensity remapping was done by applying the so called look-up-table, this table matches each intensity value with appropriate value using linear remapping, the look up table is graphically depicted in Fig. 2.

The structure of look-up-table:

- Inside the lumen:
  Pixel intensities inside the limen fall into the interval $\langle \max(l(i)), \min(l(i)) \rangle$, where $\min(l(i))$ is almost 0 in all cases. What we want is to remap these values into the interval $\langle 0, 5 \rangle$. However, $\max(l(i))$ can be - due to artifacts, noise and other factors - corrupted, therefor we take a quantile of 80% of $l(i)$ (we assume that 20% of points can be corrupted). This quantile value was marked as $Q_{0.8}(l(i))$. The mapping of points inside artery can be defined as:
  $$\left. \begin{array}{l} 0 \rightarrow 0 \\ Q_{0.8}(l(i)) \rightarrow 5 \end{array} \right\}$$

- On the arterial wall:
  Points on the arterial wall have a mean value of intensity $\text{mean}(w(i))$, we know that this value should be transfered to 180. In similar way we can define the mapping of pixels on the arterial wall as:

$$\left. \begin{array}{l} \text{mean}(w(i)) \rightarrow 180 \\ 255 \rightarrow 255 \end{array} \right\}$$

The points in LUT are approximated by lines. The final LUT is depicted on Fig. 2.
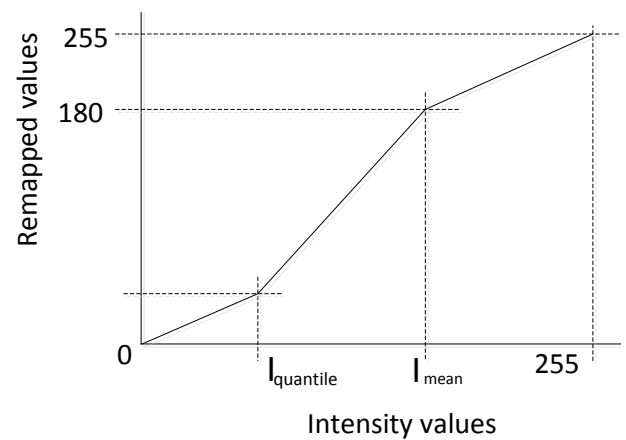
Fig. 2: Remapping Function

IV. Results

We tested our method on 84 ultrasound images, the evaluation was done mathematically by comparing the values of pixels in both areas inside the lumen and on the arterial border as shown in Fig. 3, where we can see the two box plots representing the intensity values inside the lumen and on the arterial wall respectively, before and after the normalization procedure was applied, in Fig. 3(a) we notice that most of pixels inside the lumen had the values 0-20 before normalization, but after normalization these pixels had the values 0-5. In similar way pixels on the arterial wall were remapped to have intensity values 150-200 (which are around the wanted value 180) as shown in Fig. 3(b).

Fig. 3(c) shows mean values computed from all images inside the artery, where mean values were between 2-4 before normalization but after normalization they were moved to the range 4-6. In similar way mean values on the arterial wall were moved from the range 80-100 to the range 140-160 as shown in Fig. 3(d).

By plotting the mean values calculated for each image inside the lumen as showed in Fig. 3(e),(f) we notice that mean
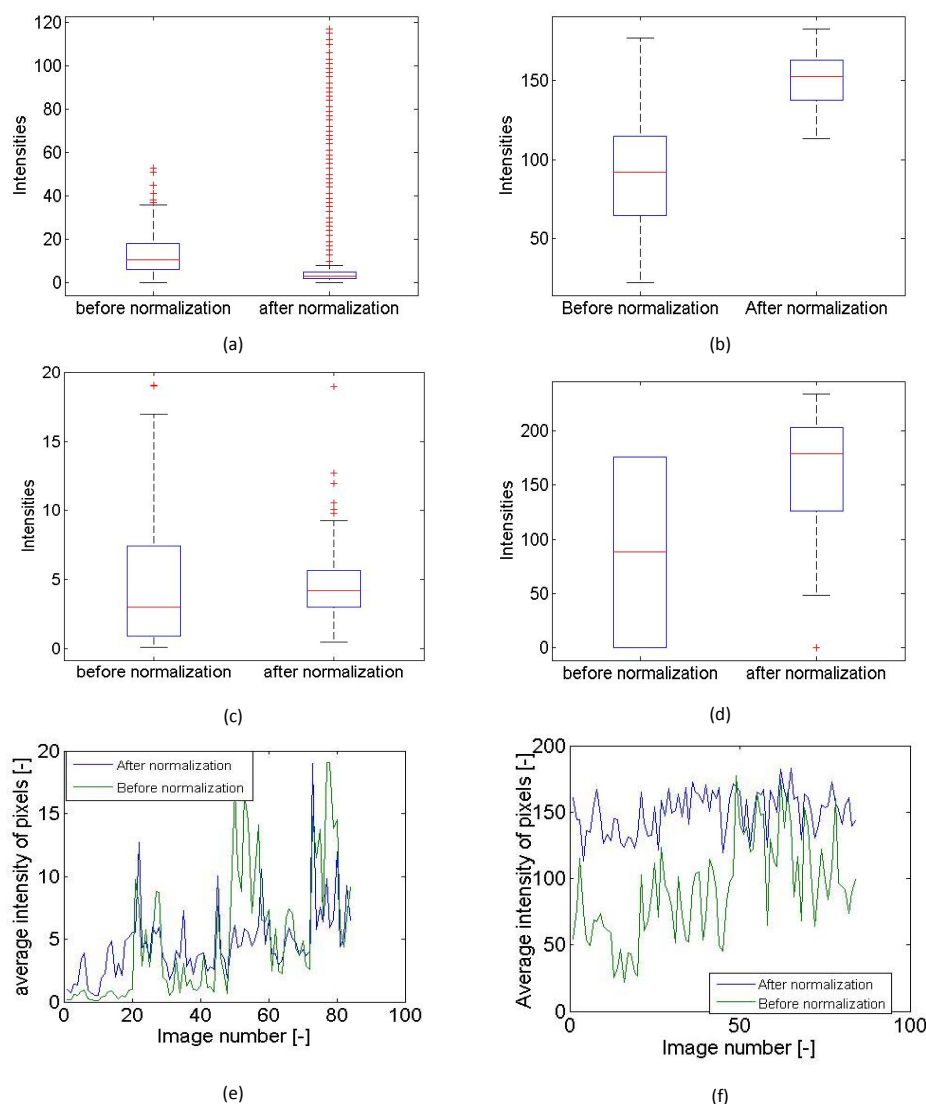
Fig. 3: (a) pixels' intensity values inside the lumen (b) pixels' intensity values on the arterial wall (c) Box plot of mean values of pixels inside the lumen computed from all images (d) Box plot of mean values of pixels on the arterial wall computed from all images (e) mean value of each image inside the lumen (f) mean value of each image on the arterial wall

values inside the lumen were even lower than 4 or higher than 8, but after normalization most of them fall into the range between 0 to 6 Fig. 3(e), while mean values on the arterials wall were less than 100 before normalization (Fig. 3(f)), but after normalization they were transfered to the range between 140 and 170. The main interest of experts when evaluating an ultrasound image is the ability to extract usefull information, they are primarily interested in differentiating blood from carotid wall, intima media, or plaque surface, which is very dependent on the image's quality. In Fig. 4 we can see the differences between ultrasound images before and after normalization especially inside the lumen area.

V. CONCLUSION

In this paper we have investigated the usefulness of normalization on the image quality as an important step for later

processing of the image. Normalization was also proposed in other studies using blood echogenicity as a reference, and applied in carotid artery images [6]. In [7], [8], it was shown that normalization improves the image comparability by reducing the variability introduced by different gain settings, different operators and different equipment [1]. We tested our method on 84 ultrasound carotid images. Images were evaluated by comparing the pixel values in addition to mean values in each image, in the areas inside the lumen and on the arterial wall, before and after applying normalization. It can be seen in Fig. 3(a) that most of the pixels inside the lumen were remapped to the desirable range 0-5 after normalization, while they had the values 0-20 before normalization. In a similar way, as shown in Fig. 3(b), pixels on the arterial wall were remapped to have intensity values 150-200 (which are around the wanted value 180). Fig. 3(c) shows mean values
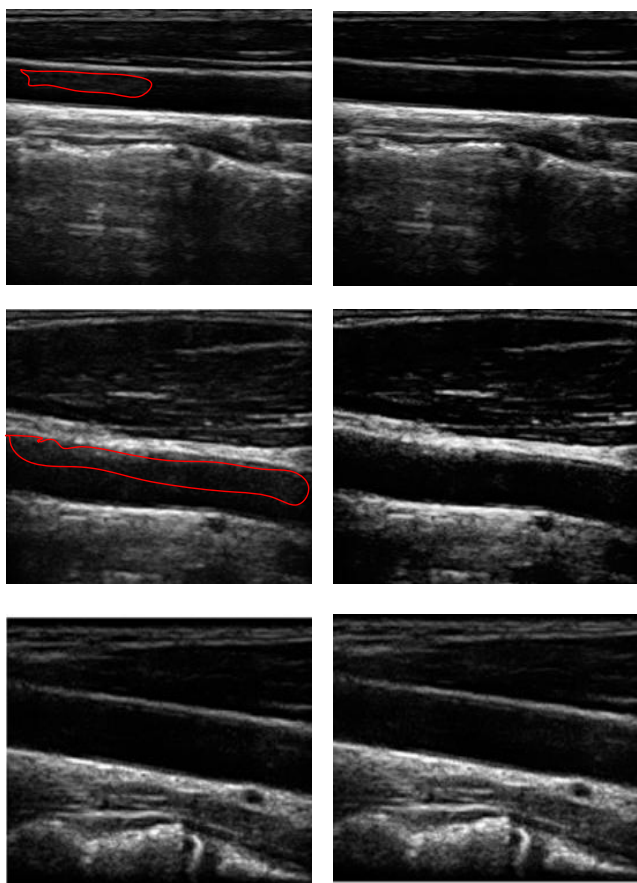
Fig. 4: (a), (c), (e) are images before normalization. (b), (d), (f) after normalization. We can see, For example in c, the normalization method decrease the echo artifacts in arterial lumen.

computed from all images inside the lumen, those values were between 2-4 before normalization but after normalization they were moved to the range 4-6. Mean values on the arterial wall were moved from the range 80-100 to the range 140-160 as can be seen in Fig. 3(d). Visual evaluation was also applied, results showed that the remapping of pixel intesities resulted in a better image quality, which is important for better analysis of the image. As it can be seen in Fig.4. Concluding results of this study showed that normalization is an important step in enhancing the quality of ultrasound images for the purpose of efficient segmentation or subsequent processing, the usefulness of this method in ultrasound systems needs to be more investigated.

REFERENCES

[1] Loizou, C. and Pattichis, C. and Pantziaris, M. and Tyllis, T. and Nicolaides, A., "Quality evaluation of ultrasound imaging in the carotid artery based on normalization and speckle reduction filtering",*Medical and Biological Engineering and Computing*, Volume 44, Issue 5, 2006, Pages 414-426, ISSN 0140-0118, DOI:10.1007/s11517-006-0045-1.

[2] Loizou, C.P.; Pattichis, C.S.; Pantziaris, M.; Nicolaides, A.; , "An Integrated System for the Segmentation of Atherosclerotic Carotid Plaque", *Information Technology in Biomedicine, IEEE Transactions on*, vol.11, no.6, pp.661-667, Nov. 2007. doi: 10.1109/TITB.2006.890019

[3] Molinari,F.,Zeng,G.,Suri,J. S.,"A state of the art review on intimamedia thickness (IMT)measurement and wall segmentation techniques for carotid ultrasound", *Computer Methods and Programs in Biomedicine*, Volume 100, Issue 3, December 2010, Pages 201-221, ISSN 0169-2607, DOI:10.1016/j.cmpb.2010.04.007.

[4] Treece, G.; Prager, R.; Gee, A.; , "Ultrasound attenuation measurement in the presence of scatterer variation for reduction of shadowing and enhancement", *Ultrasonics, Ferroelectrics and Frequency Control, IEEE Transactions on* , vol.52, no.12, pp.2346-2360, Dec. 2005 doi: 10.1109/TUFFC.2005.1563279

[5] I. B. Casella, C. Presti, R. M. P. Porta, C. R. D. Sabbag, M. A. Bosch,Y. Yamazaki, "A practical protocol to measure common carotid arteryintima-media thickness", *Clinics*, Volume 63, Issue 4, 2008, ISSN 1807-5932.

[6] Wilhjelm, J.E.; Gronholdt, M.-L.M.; Wiebe, B.; Jespersen, S.K.; Hansen, L.K.; Sillesen, H.; , "Quantitative analysis of ultrasound B-mode images of carotid atherosclerotic plaque: correlation with visual classification and histological examination", *Medical Imaging, IEEE Transactions on*, vol.17, no.6, pp.910-922, Dec. 1998, DOI: 10.1109/42.746624.

[7] Elatrozy T, Nicolaides A, Tegos T, Zarka AZ, Griffin M,Sabetai M, "The effect of B-mode ultrasonic image standardization of the echodensity of symptomatic and asymptomatic carotid bifurcation plaque", *International Angiology*, September 1998, Volume 17, Issue 3, Pages 179186.

[8] Kyriakou E, Pattichis MS, Christodoulou C, Pattichis CS,Kakkos S, Griffin M, Nicolaides A, "Ultrasound imaging in the analysis of carotid plaque morphology for the assessment of stroke", 2005, PMID: 15923744.

[9] Benes, R.; Hasmanda, M.; Riha, K.; , "Object localization in medical images", *Telecommunications and Signal Processing (TSP), 2011 34th International Conference on*, vol., no., pp.559-563, 18-20 Aug. 2011, DOI: 10.1109/TSP.2011.6043667

[10] . D. Gill, H. M. Ladak, D. A. Steinman, and A. Fenster, "Segmentation of ulcerated plaque: A semi-automatic method for tracking the progression of carotid atherosclerosis," in *Proc. World Congr. Med. Phys. Biomed. Eng.*, Chicago, IL, 2000, pp. 14, 2000.

[11] . Zhang, C. R. McKay, and M. Sonka, "Tissue characterization in intravascular ultrasound images," *IEEE Trans. Med. Imag.*, vol. 17, no. 6, pp. 889899, Dec. 1998.

[12] . R. Cardinal, J. Meunier, G. Soulez, E. Th'erasse, and G. Cloutier, "Intravascular ultrasound image segmentation: A fast-marching method," in *Proc. MICCAI, LNCS 2879*, 2003, pp. 432439.

[13] . Brusseau, C. L. De Korte, F. Mastick, J. Schaar, and A. F. W. Van der Steen, "Fully automatic luminal contour segmentation in intracoronary ultrasound imaging: A statistical approach," *IEEE Trans. Med. Imag.*, vol. 23, no. 5, pp. 554566, May 2004.

Yara OMRAN received her M.Sc. degree in Electronics & Communication in 2009. Now she is a PhD student at Brno University of Technology, Faculty of Electrical Engineering, Department of Telecommunications. The area of her professional interests is focused mainly on medical image processing..

Radek BENES eceived his M.Sc. degree in Electronics & Communication in 2008. Presently, he studys at Brno University of Technology, Faculty of Electrical Engineering, Department of Telecommunications. His research interests is focused mainly on medical image processing.

Kamil RIHA received his M.Sc. degree in Electronics & Communication in 2003 and the Ph.D. degree in 3D Scene Acquisition for AutoStereoscopic Display in 2007. Presently, he is employed at Brno University of Technology, Faculty of Electrical Engineering, Department of Telecommunications, as the academic employee (since 2006). His research interests include in particular areas of digital image processing and electronics.

Efficient Spectral Estimation of Non-Stationary Harmonic Signals Using Harmonic Transform

Michal Trzos and Hasan Khaddour

Abstract—Non-stationary harmonic signals cannot be accurately represented by Fourier transform (FT). Fortunately, several methods for representing non-stationary harmonic signals exist including Fan-Chirp trasnform (FChT) or Harmonic transform (HT). This article is focused on the Harmonic transform and its computation. Estimation of slope of fundamental frequency change between analysed segments is essential for computation of the HT. The slope is estimated using several realisations of HT and comparing the spectral flatness. Optimisation of this procedure is presented in the article.

Keywords—Harmonic transform, non-stationary harmonic signals, time-frequency representations.

I. Introduction

The FT is generally able to represent frequency content of a signal, when the signal is composed of components with invariant frequency. Such signals can be called stationary harmonic signals and by using FT we can get their frequency representation with sufficient resolution in a specified frequency band. The ability of the FT to represent frequency content of a signal dimnishes if the signals contains components with varying frequency [1], [2].

One solution of this problem is to use Warped Fourier Transform (WFT) [3], where the signal is frequency warped before applying the FT. This operation can be interpreted as change of the signal's scale for the conversion of time-varying frequency components to frequency invariant components. The scaling operation can be generalized using the Scale Transform (ST) [4], [5], [6], where the scale is taken as a physical property of the signal, or the scaling operation can be integrated into the definition of transformation, as in Harmonic Transform [7].

There are other transforms for representation of nonstationary harmonic signals, which are suitable for specific applications. The Fractional Fourier Transform (FrFT) [8], [9] and Chirp Transform (CT) [10], [11] are suitable for linearly changing frequency components, whereas the Fan-Chirp Transform [12], [13] is suitable for signals with frequency components varying linearly on a fan geometry.

II. Harmonic Transform

Harmonic transform has been introduced in [7] and its main difference from Fourier transform is the integrated time-warping function. It is defined as

$$S_{\phi_{\mathrm{u}}(t)}(\omega) = \int_{-\infty}^{+\infty} s(t)\phi_{\mathrm{u}}'(t)\mathrm{e}^{-\mathrm{j}\omega\phi_{\mathrm{u}}(t)}\mathrm{d}t, \qquad (1)$$

M. Trzos and H. Khaddour are with the Department of Telecomunications, Brno University of Technology, Brno, Czech Republic, e-mail: trzos@phd.feec.vutbr.cz and xkhadd00@stud.feec.vutbr.cz.

where $\phi_{\mathrm{u}}(t)$ is unit phase, which is the phase of the fundamental harmonic component divided by its instantaneous frequency [7], and $\phi_{\mathrm{u}}'(t)$ is first derivation of $\phi_{\mathrm{u}}(t)$. Linear change of fundamental frequency in a given segment is presumed, which is sufficiently satisfied by selecting an analysis window of appropriate length.

Instantaneous phase $\varphi(t)$ of a sinusoid with linear change of frequency [14] is defined as

$$\varphi(t) = 2\pi\left(f_0 t + \frac{\epsilon t^2}{2}\right), \qquad (2)$$

where f_0 is fundamental fequency and $\epsilon = \Delta f_0/T$ is the change of fundamental frequency divided by lenght of the segment. Assuming discrete signal segment of the length N, where $T = N/F_{\mathrm{s}}$, the discrete phase $\varphi(n)$ of a sinusoid with linear frequency variation [15] can be written as

$$\varphi(n) = 2\pi\left(\frac{f_0 n}{F_{\mathrm{s}}} + \frac{\Delta f_0 n^2}{2N F_{\mathrm{s}}}\right), \qquad (3)$$

where f_0 is discrete instantaneous frequency, N is length of the analysis window, and F_{s} is sampling frequency (initial phase is disregarded for simplicity).

Initial fundamental frequency in a given segment can be written as

$$f_0 = f_{\mathrm{c}} - \frac{a f_{\mathrm{c}}}{2}, \ a = \frac{\Delta f_0}{f_{\mathrm{c}}}, \qquad (4)$$

where f_{c} is the central fundamental frequency within a segment and a is the slope of fundamental frequency change within the segment. Substituting (4) to (3) we get [15]

$$\varphi(n) = \frac{2\pi}{N}\alpha(n), \ \alpha_a(n) = n\left(1 - \frac{a}{2} + \frac{an}{2N}\right). \qquad (5)$$

Frequencies of spectral lines of the Fourier transform are given as

$$f_{\mathrm{c}} = \frac{F_{\mathrm{s}}}{N}, \qquad (6)$$

and from the equation (5) it is obvious that the instantaneous phase is

$$\varphi(n) = \frac{F_{\mathrm{s}}}{N}\alpha(n). \qquad (7)$$

Discrete harmonic transform (DHT) of signals with linear fundamental frequency variation [15] is defined as

$$s(n) = \frac{1}{N}\sum_{k=0}^{N-1} s(n)\alpha'(n)\mathrm{e}^{\mathrm{j}\frac{2\pi k}{N}\alpha(n)}, \qquad (8)$$

where

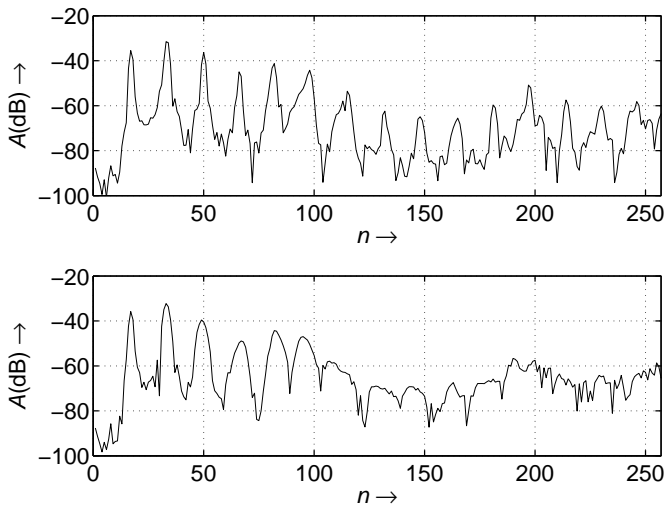$$\alpha_a'(n) = 1 - \frac{a}{2} + \frac{an}{N}, \qquad (9)$$

Fig. 1. Fourier transform spectrum (bottom); Harmonic transform spectrum with parameter $a = 0.2$ (top).
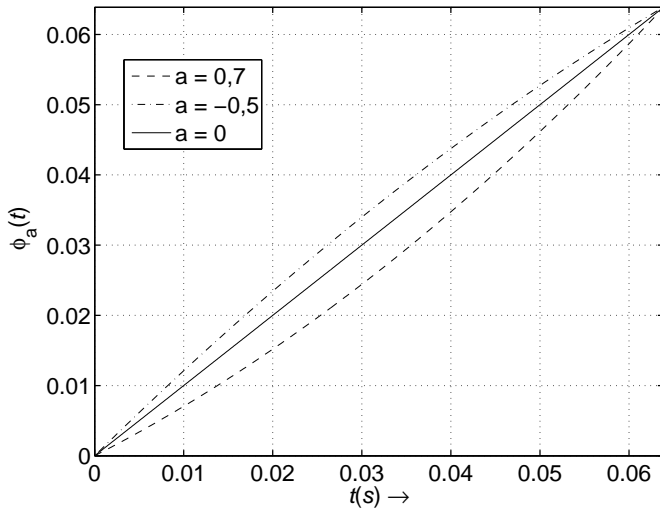
Fig. 2. Influence of parameter a on the phase function $\phi_{\mathrm{a}}(t)$.

is first-order derivation of (5).

The difference between DFT and DHT at analysis of non-stationary harmonic signals can be seen on a part of speech uttering from the PTDB-TUG database with frequency modulation. On Fig. 1 (bottom) we can see that the higher frequencies are smoothed due to frequency modulation. On Fig. 1 (top) even high frequency peaks are clearly visible.

III. ESTIMATING PARAMETER a

As can be seen from equation (4), a determines the change of fundamental frequency in the analysed signal, with the assumption of linear fundamental frequency change. Variation of a results in time-warping of the analysed signal, as can be seen on Fig. 2.

The parameter a is usually estimated by grid search. It consists of performing several realisations of HT with different a [7]. Afterwards, the realisation which minimises spectral
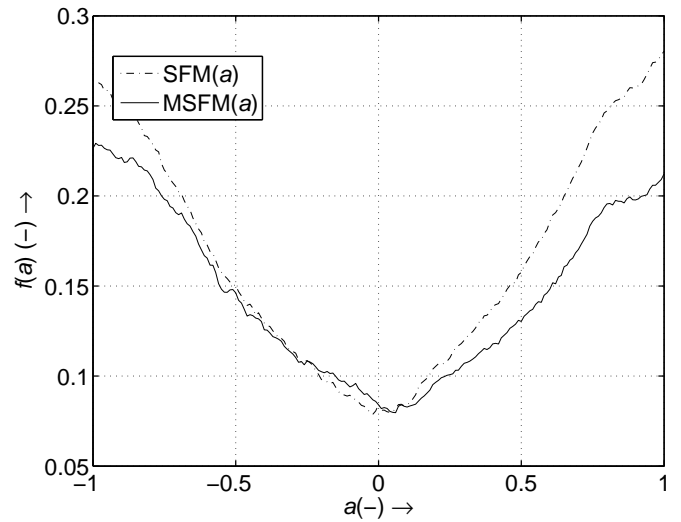
Fig. 3. Comparison of spectral flatness measure and modified spectral measure fo the analysed segment.

flatness measure (SFM)

$$\arg\min_a \mathrm{SFM}(a) = \frac{\sqrt{\prod_{k=0}^{N-1} |\mathrm{DHT}(a,k)|}}{\frac{1}{N}\sum_{k=0}^{N-1}|\mathrm{DHT}(a,k)|}, \qquad (10)$$

where DHT is discrete harmonic transform and $|.|$ denotes absolute value, is selected as the correct value. This approach is computationaly extensive and is usually simplified restricting values a can have and by following the change of fundamental frequency in time [15].

When using (10) the SFM has several minimums and if a search algorithm was used, it could fall into local minimum. It is also noteworthy that it is possible the harmonic transform $|\mathrm{DHT}(a,k)|$ will be equal to zero for some values of k, which could mean that the spectral flatness will be zero for all a. Removing zero values solves this problem and leads to band-limited spectral flatness measure.

The harmonic spectrum is not complex conjugated even for real signals (which is true for Fourier transform). From the frequency axis point of view, the unit phase function $\phi_{\mathrm{u}}(t)$ shifts the spectrum towards lower frequencies if a is positive, and to higher frequencies if its negative. Using the formula (8) we get only one-sided spectrum, the right part will not represent harmonic components of the analysed signal. When estimating a, (10) has two minimums (see Fig. 3). For harmonic signal analysis, only left side of the spectrum is useful, because it appropriately represents non-stationary harmonic signal. Using the modified spectral flatness measure (MSFM)

$$\arg\min_a \mathrm{MSFM}(a) = \frac{\sqrt{\prod_{k=0}^{N/2} |\mathrm{DHT}(a,k)|}}{\frac{1}{N/2+1}\sum_{k=0}^{N/2}|\mathrm{DHT}(a,k)|}, \qquad (11)$$

we can get function of a which has clearly defined minimum. This is caused by using only left side of the spectrum and it consequently leads to reducing the number of operations needed to compute spectral flatness by $\frac{N}{2} - 1$.

IV. Conclusion

Harmonic transform with some of its features and parameters has been described. Furthermore, the parameter a and its influence on non-stationary signal analysis was analysed. By reducing the number of operations in computation of spectral flatness measure, the number of operations needed for computation of Harmonic transform is reduced.

Future work aims at further improving the performance of harmonic transform computation using parallelisation and using machine learning for estimation of parameter a. Sensitivity to noise will also be measured.

Acknowledgment

References

[1] M. Goodwin and M. Vetterli, "Time-frequency signal models for music analysis, transformation, and synthesis," in *Proceedings of the IEEE-SP International Symposium on Time-Frequency and Time-Scale Analysis*, 1996, pp. 133–136.

[2] G. Wakefield, "Time-pitch representations: acoustic signal processing and auditory representations," in *Time-Frequency and Time-Scale Analysis, 1998. Proceedings of the IEEE-SP International Symposium on*, Oct. 1998, pp. 577–580.

[3] A. Makur and S. Mitra, "Warped discrete-fourier transform: Theory and applications," *Circuits and Systems I: Fundamental Theory and Applications, IEEE Transactions on*, vol. 48, no. 9, pp. 1086–1093, Sep. 2001.

[4] L. Cohen, "The scale representation," *Signal Processing, IEEE Transactions on*, vol. 41, no. 12, pp. 3275–3292, Dec. 1993.

[5] T. Irino and R. D. Patterson, "Segregating information about the size and shape of the vocal tract using a time-domain auditory model: the stabilised wavelet-mellin transform," *Speech Commun.*, vol. 36, pp. 181–203, Mar. 2002.

[6] A. De Sena and D. Rocchesso, "A study on using the mellin transform for vowel recognition," in *SMC05, International conference on Sound Music and Computing*, Salerno, Italy, 2005.

[7] F. Zhang, G. Bi, and Y. Chen, "Harmonic transform," *Vision, Image and Signal Processing, IEE Proceedings*, vol. 151, no. 4, pp. 257–263, Aug. 2004.

[8] D. Bailey and P. Swarztrauber, "The fractional fourier transform and applications," *SIAM Review*, vol. 33, no. 3, pp. 389–404, Sep. 1995.

[9] R. Tao, Y.-L. Li, and Y. Wang, "Short-time fractional fourier transform and its applications," *Signal Processing, IEEE Transactions on*, vol. 58, no. 5, pp. 2568–2580, May 2010.

[10] L. Weruaga and M. Képesi, "Speech analysis with the short-time chirp transform," in *Eurospeech*, Geneve, Sep. 2003, pp. 53–56.

[11] M. Képesi and L. Weruaga, "Speech analysis with the fast chirp transform," 2004.

[12] L. Weruaga and M. Képesi, "The fan-chirp transform for non-stationary harmonic signals," *Signal Processing*, vol. 87, no. 6, pp. 1504–1522, 2007.

[13] M. Képesi and L. Weruaga, "Adaptive chirp-based time–frequency analysis of speech signals," *Speech Communication*, vol. 48, no. 5, pp. 474–492, 2006.

[14] P. Zubrycki and A. Petrovsky, "Accurate estimation of harmonic amplitudes in voiced speech based on harmonic transform," in *Signals and Electronic Systems, 2008. ICSES '08. International Conference on*, Sep. 2008, pp. 47 –50.

[15] ——, "Accurate speech decomposition into periodic and aperiodic components based on discrete harmonic transform," in *15th European Signal Processing Conference (EUSIPCO 2007)*, Poznań, Poland, 2007, pp. 2336–2340.

Michal Trzos received B.Sc. degree in teleinformatics and M.Sc. degree in telecommunications and informatics from the Faculty of Electrical Engineering, Brno University of Technology (BUT), CZE, in 2007 and 2009 respectively. Since 2009, he is a Ph.D. candidate at the Department of Telecommunications. His main task is to explore new methods of time and frequency warping of audio signals. His research interests include: general-purpose computing on graphics processing units, audio algorithm parallelization, time-frequency transformations, and speech processing.

Hasan Khaddour received his Eng. title from the Department of Telecommunications and Electronics, Faculty of Mechanical and Electrical Engineering, Tishreen University, Syria, in 2007. Since 2009, he is a Ph.D. candidate at the Department of Telecommunications, Faculty of Electrical Engineering, Brno University of Technology (BUT), Czech Republic. His current research is focused on sound source localization, acoustical zooming, and sound rendering methods.

On time to buffer saturation in a $GI/M/1/N$-type queue

Wojciech M. Kempa

Abstract—A $GI/M/1/N$-type queuing system with independent and generally distributed interarrival times and exponential service times is investigated. A system of equations for conditional distributions of the time to the first buffer saturation is built. The solution is written using a special-type sequence defined by "input" distributions of the system. The formula of total probability is used to derive a representation for the distribution of the time to the kth buffer saturation for $k \geq 2$. Moreover, special cases of the Poisson arrival process and the system with one-place buffer are discussed. Sample numerical results for the 3-Erlang and deterministic distributions of interarrival times are attached as well.

Keywords—Buffer saturation, finite-buffer queue, formula of total probability, integral equation, Markov moment.

I. INTRODUCTION

A phenomenon of buffer saturation and, in consequence, losses of the arriving packets is a typical one in telecommunication networks. As one can note, the well-known performance measure as the loss ratio, defined as a part of the total amount of packets in transmission that is lost due to the buffer saturation, does not give a sufficient information about the process of losses from the probabilistic point of view. The in-depth analysis of the problem of losses requires the knowledge about distributions of times to successive buffer saturations (or, in other words, periods during which the service process is not blocked) and durations of such periods.

The review of results for stochastic characteristics of queuing systems with finite buffers in the stationary state can be found e.g. in [4], [5] and [13]. In [7] distributions of three different characteristics for the system with the enqueuing process controlled by a drop function were investigated. A part of results from [7] was generalized in [14] and [15] where systems with bounded capacity and continuously distributed packet volumes were analyzed. Transient results for finite-buffer queues can also be found e.g. in monograph [1] and in papers [8] and [9]. In particular, in [9] the system with additional single server vacations is investigated.

Analytical results for distributions of the time to the buffer saturation, in fact, are mainly restricted to systems with a Poisson arrival process (simple or compound) or with the input flow described by a variant of MAP process. In [1] the case of the system with batch Poisson arrivals and constant service times was investigated. The compact formulae for the distribution of the time to the first buffer saturation was obtained in [2] for the $BMAP/G/1/N-$type queue. The case

of the $MMPP-$type input stream can be found in [3]. Some other results related with distributions of the buffer saturation period and the process of losses can be viewed e.g. in [6] and [12]. In particular, in [6] the representation for the joint transform of the busy period and numbers of packets being served and lost during the busy period was found for the system with phase-type distributions of interarrival and service times. In [12] the representation for the distribution of the number of buffer saturations during a single busy period was obtained for the system with Poisson arrivals.

In the paper distributions of times to successive buffer saturations are investigated in the $GI/M/1/N-$type system with general independent input stream of packets and exponential service times. Applying the technique proposed in [10] and developed in [11] the compact formula for the Laplace transform of the distribution of the time to the first buffer saturation, conditioned by the number of packets present in the system at the opening, is obtained. For $k \geq 2$ a formula that allows to express the distribution of the time to the kth buffer saturation using the conditional distribution of the time to the first overflow is found.

So, the remaining part of the article is organized as follows. In the next Section 2 we present a mathematical model of the system and state auxiliary results. In Section 3 we present results for the distribution of the time to the first buffer saturation. In Section 4 a formula for computing distributions of times to next, successive buffer saturations via conditional distributions of the first one is obtained. Section 5 contains results for some special cases: the case of the system with Poisson arrival process and with one-place buffer. Section 6 is devoted to sample numerical computations, and the last Section 7 contains conclusions.

II. QUEUING MODEL AND AUXILIARY RESULTS

We consider the $GI/M/1/N$-type queuing system in which interarrival times are independent and identically distributed random variables with a general-type distribution function $F(\cdot)$, and service times are exponentially distributed with mean μ^{-1}. The maximal system capacity equals N i.e. there are $N-1$ places in the buffer queue and one place in service.

Let $F^{k*}(\cdot)$ be the k-fold Stieltjes convolution of the distribution function $F(\cdot)$ with itself. Besides, introduce the notation

$$f(s) = \int_0^\infty e^{-st} dF(t), \quad \mathrm{Re}(s) > 0. \tag{1}$$

Denote by $X(t)$ the number of packets present in the system at time t. Let $\beta_n^{(k)}$ be the time to the kth saturation of the buffer on condition that the system contains exactly n packets

at the opening. So, $\beta_n^{(k)}$ is the time between the completion epoch of the $(k-1)$th period of buffer saturation and the initial moment of the kth period of saturation. Of course, $\beta_n^{(1)}$ denotes the time from the opening of the system to the first time of buffer overflow. Thus, we have

$$\beta_n^{(k)} = \inf\{t > 0 : X(t + \tau_{k-1}) = N \,|\, X(0) = n\}, \quad (2)$$

where $k \geq 1$, $0 \leq n \leq N-1$ and τ_k stands for the completion epoch of the kth period of buffer saturation (with additional agreement $\tau_0 = 0$).

For the investigation of the distribution of the time to the buffer saturation we propose the approach in which a certain specific-type system of equations occur. The solution of the system is found using the following result from [10] (see also [11]) :

Theorem 1. *Let (α_k), $k \geq 0$, $\alpha_0 \neq 0$, and (φ_k), $k \geq 1$, be known sequences.*

Every solution of the following system of equations:

$$\sum_{k=-1}^{n-1} \alpha_{k+1} x_{n-k} - x_n = \varphi_n, \quad n \geq 1, \quad (3)$$

can be written in the following form:

$$x_n = CR_n + \sum_{k=1}^{n} R_{n-k}\varphi_k, \quad n \geq 1, \quad (4)$$

where C does not depend on n and (R_k) is a sequence defined recursively by means of the given sequence (a_k) in the following way:

$$R_0 = 0, \quad R_1 = \alpha_0^{-1},$$
$$R_{k+1} = R_1\left(R_k - \sum_{i=0}^{k} \alpha_{i+1} R_{k-i}\right), \quad k \geq 1. \quad (5)$$

The sequence (R_k) is called potential connected with the known sequence (α_k).

In fact, in the paper we use a slightly modified version of Theorem 1, given below, where the system of equations is numbered beginning with $n = 2$. Indeed, the following corollary is a simple consequence of the last theorem:

Corollary 1. *Each solution of the following system of equations:*

$$\sum_{k=-1}^{n-2} \alpha_{k+1} x_{n-k} - x_n = \varphi_n, \quad n \geq 2, \quad (6)$$

can be written as

$$x_n = CR_{n-1} + \sum_{k=2}^{n} R_{n-k}\varphi_k, \quad n \geq 2, \quad (7)$$

where C is a constant independent on n and the potential (R_k), $k \geq 0$, connected with the sequence (α_k), is defined by the formulae (5).

III. DISTRIBUTION OF THE TIME TO THE FIRST BUFFER SATURATION

The main result of this section is a theorem that gives the explicit representation for the Laplace transform of the tail $B_n^{(1)}(\cdot)$ of conditional distribution function of the time $\beta_n^{(1)}$ from $t = 0$ to the moment of the first buffer saturation, for any value of initial system "contents" n.

Define

$$B_n^{(1)}(t) = \mathbf{P}\{\beta_n^{(1)} > t\}, \quad (8)$$

where $t > 0$, $0 \leq n \leq N-1$.

Since the arrival instants in the $GI/M/1$-type queue are renewal (Markov) moments, then, applying the formula of total probability with respect to the first arrival moment after the opening of the system, we can write the following system of integral equations:

$$B_n^{(1)}(t) = \sum_{k=0}^{n-1} \int_0^t \frac{(\mu x)^k}{k!} e^{-\mu x} B_{n-k+1}^{(1)}(t-x) dF(x)$$
$$+ \sum_{k=n}^{\infty} \int_0^t \frac{(\mu x)^k}{k!} e^{-\mu x} B_1^{(1)}(t-x) dF(x) + (1 - F(t)), \quad (9)$$

where $0 \leq n \leq N-2$.

Let us comment briefly (9). The first summand on the right side of (9) describes the case in that the first packet arrives at time $x < t$ and before the first arrival the system does not empty completely. In consequence the number of packets at the first Markov moment x equals $n - k + 1$, where k denotes the number of packets completely served before x, and the random event $\{\beta_n^{(1)} > t\}$ coincides with $\{\beta_{n-k+1}^{(1)} > t - x\}$. The second summand on the right side of (9) presents the situation in which the queue becomes empty before the first arrival epoch $x < t$. Thus, at the moment x the system "renews" its operation with exactly $n = 1$ packet present. Obviously, if the first packet enters after t, then $\{\beta_n^{(1)} > t\}$ with probability one (compare the third summand on the right side of (9)).

Similarly, for $n = N - 1$ we get

$$B_{N-1}^{(1)}(t) = \sum_{k=1}^{N-2} \int_0^t \frac{(\mu x)^k}{k!} e^{-\mu x} B_{N-k}^{(1)}(t-x) dF(x)$$
$$+ \sum_{k=N-1}^{\infty} \int_0^t \frac{(\mu x)^k}{k!} e^{-\mu x} B_1^{(1)}(t-x) dF(x) + (1 - F(t)), \quad (10)$$

Let us note that in the first summand on the right side of (10) the sum is taken from $k = 1$. Evidently, in the situation of no completed services before the first arrival moment x, at time x the buffer becomes saturated. Since $x < t$, then the random event that the time to the first buffer saturation exceeds t has probability zero.

Let us introduce the following notation:

$$\alpha_k(s) = \int_0^\infty \frac{(\mu x)^k}{k!} e^{-(\mu+s)x} dF(x), \quad k \geq 0. \quad (11)$$

Moreover, let

$$B_n^{(1)}(s) = \int_0^\infty e^{-st} B_n^{(1)}(t) dt, \quad \text{Re}(s) > 0. \quad (12)$$

Now the system (9)–(10) can be transformed to the following form:

$$B_n^{(1)}(s) = \sum_{k=0}^{n-1} \alpha_k(s) B_{n-k+1}^{(1)}(s)$$

$$+ B_1^{(1)}(s) \sum_{k=n}^{\infty} \alpha_k(s) + \frac{1-f(s)}{s}, \quad 0 \le n \le N-2, \quad (13)$$

$$B_{N-1}^{(1)}(s) = \sum_{k=1}^{N-2} \alpha_k(s) B_{N-k}^{(1)}(s)$$

$$+ B_1^{(1)}(s) \sum_{k=N-1}^{\infty} \alpha_k(s) + \frac{1-f(s)}{s}. \quad (14)$$

Defining the following sequence:

$$\varphi_n(s) = -B_1^{(1)}(s) \sum_{k=n}^{\infty} \alpha_k(s) - \frac{1-f(s)}{s}, \quad n \ge 0, \quad (15)$$

the system (13) can be rewritten as

$$\sum_{k=-1}^{n-2} \alpha_{k+1}(s) B_{n-k}^{(1)}(s) - B_n^{(1)}(s) = \varphi_n(s), \quad (16)$$

where $0 \le n \le N-2$.

It is easy to note that the system (16) has the same form as (6). Of course, since now α_k and φ_n are, in general, functions of s, then the representation for the solution of (16) should be written as (see (7)):

$$B_n^{(1)}(s) = C(s) R_{n-1}(s) + \sum_{k=2}^{n} R_{n-k}(s) \varphi_k(s), \quad (17)$$

where $n \ge 2$, the function $C(s)$ is independent on n and the potential $R_k(s)$ is defined in (5), where now $\alpha_k = \alpha_k(s)$.

Of course, at this stage it is impossible to write down the formulae for $B_n^{(1)}$, $0 \le n \le N-1$, explicitly since the expressions for $C(s)$, $B_0(s)$ and $B_1(s)$ are unknown (the formula (17) is valid for $n \ge 2$). To find them substitute firstly $n = 2$ into the equation (17). We obtain

$$B_2^{(1)}(s) = C(s) R_1(s) = \frac{C(s)}{\alpha_0(s)}. \quad (18)$$

Taking $n = 1$ in (13) and applying the identities

$$\alpha_0(s) = f(s+\mu) \quad \text{and} \quad \sum_{k=0}^{\infty} \alpha_k(s) = f(s), \quad (19)$$

we get

$$B_1^{(1)}(s) = \alpha_0(s) B_2^{(1)}(s)$$

$$+ B_1^{(1)}(s) \big(f(s) - f(s+\mu) \big) + \frac{1-f(s)}{s}, \quad (20)$$

Now, substituting (18) into (20), we have

$$B_1^{(1)}(s) = \frac{s^{-1}\big(1 - f(s)\big) + C(s)}{1 - f(s) + f(s+\mu)}. \quad (21)$$

Similarly, taking $n = 0$ in (13), we obtain

$$B_0^{(1)}(s) = B_1^{(1)}(s) f(s) + \frac{1-f(s)}{s}. \quad (22)$$

Let us now substitute $n = N - 1$ into the formula (17). Applying, additionally, the representations (15) and (21) we get

$$B_{N-1}^{(1)}(s) = C(s) R_{N-2}(s) - \sum_{k=2}^{N-1} R_{N-1-k}(s)$$

$$\times \left(\frac{s^{-1}\big(1-f(s)\big) + C(s)}{1 - f(s) + f(s+\mu)} \sum_{i=k}^{\infty} \alpha_i(s) + \frac{1-f(s)}{s} \right). \quad (23)$$

Another representation for $B_{N-1}^{(1)}(s)$ can be found using the formula (14). Substituting the identity (17) into (14) we have

$$B_{N-1}^{(1)}(s) = \sum_{k=1}^{N-2} \alpha_k(s) \left[C(s) R_{N-1-k}(s) - \sum_{i=2}^{N-k} R_{N-k-i}(s) \right.$$

$$\left. \times \left(\frac{s^{-1}\big(1-f(s)\big) + C(s)}{1 - f(s) + f(s+\mu)} \sum_{j=i}^{\infty} \alpha_j(s) + \frac{1-f(s)}{s} \right) \right]$$

$$+ \frac{s^{-1}\big(1-f(s)\big) + C(s)}{1 - f(s) + f(s+\mu)} \sum_{k=N-1}^{\infty} \alpha_k(s) + \frac{1-f(s)}{s}. \quad (24)$$

Now, we can find easily the formula for $C(s)$, comparing the right sides of (23) and (24). Indeed, we obtain

$$C(s) = \frac{s^{-1}\big(1 - f(s)\big)\big(1 + a(s) - d(s) + g(s)\big)}{h(s) + d(s) - a(s)}, \quad (25)$$

where

$$a(s) = \frac{\sum_{k=2}^{N-1} R_{N-1-k}(s) \sum_{i=k}^{\infty} \alpha_i(s) + \sum_{k=N-1}^{\infty} \alpha_k(s)}{1 - f(s) + f(s+\mu)}, \quad (26)$$

$$d(s) = \frac{\sum_{k=1}^{N-2} \alpha_k(s) \sum_{i=2}^{N-k} R_{N-k-i}(s) \sum_{j=i}^{\infty} \alpha_j(s)}{1 - f(s) + f(s+\mu)}, \quad (27)$$

$$g(s) = \sum_{k=2}^{N-1} R_{N-1-k}(s) - \sum_{k=1}^{N-2} \alpha_k(s) \sum_{i=2}^{N-k} R_{N-k-i}(s) \quad (28)$$

and

$$h(s) = R_{N-2}(s) - \sum_{k=1}^{N-2} \alpha_k(s) R_{N-k-1}(s). \quad (29)$$

Putting together the formulae (17), (21), (22) and (25) we obtain the following main theorem:

Theorem 2. *The formula for the Laplace transform of the tail of conditional distribution of the time $\beta_n^{(1)}$ to the first buffer saturation in the $GI/M/1/N$-type queue is following:*

$$B_n^{(1)}(s) = \int_0^{\infty} e^{-st} \mathbf{P}\{\beta_n^{(1)} > t\} dt$$

$$= \frac{s^{-1}\big(1 - f(s)\big)\big(1 + a(s) - d(s) + g(s)\big)}{h(s) + d(s) - a(s)} R_{n-1}(s)$$

$$+ \sum_{k=2}^{n} R_{n-k}(s) \varphi_k(s), \quad (30)$$

where $2 \leq n \leq N-1$, and

$$\varphi_n(t) =$$
$$-\frac{s^{-1}\big(1-f(s)\big)\big(1+g(s)+h(s)\big)}{\big(1-f(s)+f(s+\mu)\big)\big(h(s)+d(s)-a(s)\big)} \sum_{k=n}^{\infty} \alpha_k(s)$$
$$-\frac{1-f(s)}{s}. \tag{31}$$

Besides

$$B_1^{(1)}(s) = \frac{s^{-1}\big(1-f(s)\big)\big(1+g(s)+h(s)\big)}{\big(1-f(s)+f(s+\mu)\big)\big(h(s)+d(s)-a(s)\big)} \tag{32}$$

and

$$B_0^{(1)}(s) = B_1^{(1)}(s)f(s) + \frac{1-f(s)}{s}. \tag{33}$$

The representations for $R_k(s)$, $\alpha_k(s)$, $a(s)$, $d(s)$, $g(s)$ and $h(s)$ are given in (5), (11), (26), (27), (28) and (29) respectively.

IV. DISTRIBUTION OF THE TIME TO THE kTH BUFFER SATURATION FOR $k \geq 2$

The main aim of this section is in finding a formula to express the distribution (tail) of the time to the kth buffer saturation, for $k \geq 2$, defined as

$$B^{(k)}(t) = \mathbf{P}\{\beta^{(k)} > t\}, \tag{34}$$

in terms of conditional distributions (tails) $B_n^{(1)}(\cdot)$ of the time to the first saturation. Indeed, below we prove the following theorem:

Theorem 3. *In the $GI/M/1/N$−type system the tail $B^{(k)}(\cdot)$ of the distribution function of the time to the kth buffer saturation, for $k \geq 2$, is independent on k and on the initial state of the system, and can be written in terms of conditional distributions $B_n^{(1)}(\cdot)$ of the time to the first saturation in the following way:*

$$B^{(k)}(t) = \int_0^{\infty} dx \sum_{j=0}^{\infty} \int_0^x e^{-\mu y} dF^{j*}(y)$$
$$\times \int_{x-y}^{x-y+t} \left[\sum_{i=1}^{N-2} \frac{\mu^{i+1}(u-x+y)^i}{i!} e^{-\mu u} \right.$$
$$\times B_{N-i}^{(1)}\big(t-u+x-y\big)$$
$$+ \sum_{i=N-1}^{\infty} \frac{\mu^{i+1}(u-x+y)^i}{i!} e^{-\mu u}$$
$$\left. \times B_1^{(1)}\big(t-u+x-y\big) \right] dF(u)$$
$$+ \mu \int_0^{\infty} e^{-\mu x} dx \sum_{j=0}^{\infty} \int_0^x \big(1-F(x-y+t)\big) dF^{j*}(y). \tag{35}$$

Proof:

The independence of $B^{(k)}$ on k and on the number of packets present in the system initially is evident. Indeed, $\beta^{(k)}$ expresses the time from the completion epoch of the

$(k-1)$th buffer overflow period to the initial epoch of the kth one. But, independently on the initial state of the system, at the completion epoch of each period of buffer saturation the number of packets equals $N-1$ (due to "individual" service discipline).

To prove the representation (35) let us apply the formula of total probability with respect to the first arrival epoch after the buffer saturation period. Such an approach is fully justified. Indeed, in the $GI/M/1/N$-type queuing model, due to general distributions of interarrival times, the completion instants τ_1, τ_2, ... of successive periods of buffer saturation are not Markov moments. Simultaneously, due to the memoryless property of exponential distribution, each period of buffer saturation is exponentially distributed with the same mean as the service time i.e. μ^{-1}.

So, the following identity holds true:

$$B_n^{(2)}(t) = \int_0^{\infty} \mu e^{-\mu x} dx \sum_{j=0}^{\infty} \int_0^x dF^{j*}(y)$$
$$\times \int_{x-y}^{x-y+t} \left[\sum_{i=1}^{N-2} \frac{\big[\mu(u+y-x)\big]^i}{i!} e^{-\mu(u+y-x)} \right.$$
$$\times B_{N-i}^{(1)}\big(t-(u+y-x)\big)$$
$$+ \sum_{i=N-1}^{\infty} \frac{\big[\mu(u+y-x)\big]^i}{i!} e^{-\mu(u+y-x)}$$
$$\left. \times B_1^{(1)}\big(t-(u+y-x)\big) \right] dF(u)$$
$$+ \int_0^{\infty} \mu e^{-\mu x} dx \sum_{j=0}^{\infty} \int_0^x \big(1-F(x-y+t)\big) dF^{j*}(y). \tag{36}$$

Let us explain the last formula in details. We position the origin of the time axis at the initial moment of the buffer saturation period (that is a Markov moment since it is connected with an arrival of a packet). On the right side of (36) x indicates the completion epoch of this period and y is the moment of the last arrival before x. In the first summand on the right side of (36) the next packet (arriving after y) occurs after time $u < x - y + t$ and hence the system does not empty between x and $u - x + y$. The second summand relates to the situation in which the server becomes idle before time period u. The last, third summand on the right side of (36) describes the situation in which we have no arrivals during time t, beginning with the completion epoch of the buffer saturation period. In consequence, independently on the instantaneous number of packets in the system, the next period of buffer saturation will start after time t with probability one.

Simplification of (36) immediately leads to (35) □

V. SPECIAL CASES

In this section we present some results for two special cases of the considered queuing model: the case of simple Poisson arrival process and the case of the buffer with one place only.

A. System with Poisson arrivals

Let us consider the $M/M/1/N$-type queuing model in which the arriving packets occur according to a Poisson

process with intensity λ. As it turns out, in such a case it is possible to express the potential (R_k), defined in (5) and connected with the given sequence $(\alpha_k(s))$ from (11), in the explicit form.

Firstly, let us note that now we have

$$\alpha_k(s) = \lambda \int_0^\infty \frac{(\mu x)^k}{k!} e^{-(\lambda+\mu+s)x} dx = \frac{\lambda \mu^k}{(\lambda+\mu+s)^{k+1}} \tag{37}$$

and, of course, $f(s) = \frac{\lambda}{\lambda+s}$.

Define the generating function $R(s,z)$ of the potential $(R_k(s))$ in the following way:

$$R(s,z) = \sum_{k=0}^\infty z^k R_k(s), \quad |z| < 1. \tag{38}$$

Taking into consideration the definition (5) we obtain

$$
\begin{aligned}
R(s,z) &= \sum_{k=1}^\infty z^k R_k(s) = z R_1(s) \\
&+ \sum_{k=1}^\infty z^{k+1}\Big[R_1(s)\big(R_k(s) - \sum_{i=0}^k \alpha_{i+1}(s)R_{k-i}(s)\big)\Big] \\
&= z R_1(s)\big(1 + R(s,z)\big) \\
&- R_1(s) \sum_{i=0}^\infty \alpha_{i+1}(s) z^{i+1} \sum_{k=i}^\infty z^{k-i} R_{k-i}(s) \\
&= z R_1(s)\big(1 + R(s,z)\big) \\
&- R_1(s) R(s,z)\big[f\big(s+\mu(1-z)\big) - \alpha_0(s)\big].
\end{aligned} \tag{39}
$$

Now we eliminate $R(s,z)$ as follows:

$$R(s,z) = \frac{z}{f\big(s+\mu(1-z)\big) - z} \tag{40}$$

and, in the case of the considered $M/M/1/N$-type system, we get

$$R(s,z) = \frac{z[\lambda+s+\mu(1-z)]}{\lambda - z[\lambda+s+\mu(1-z)]}. \tag{41}$$

To find $R_k(s)$ in the explicit form we can use the *Mathematica* environment, e.g. the function *InverseZTransform*, substituting firstly on the right side of (41) $z = \frac{1}{z}$.

Indeed, the kth term of the potential can be written in the following form:

$$
\begin{aligned}
R_k(s) = \frac{1}{2\sigma(s)(2\lambda)^k}\Big\{ & 2\kappa(s)\Big[\big(\kappa(s)+\sigma(s)\big)^n \\
& - \big(\kappa(s)-\sigma(s)\big)^n\Big] \\
& + I\{k \geq 1\}\Big[\big(\kappa(s)+\sigma(s)\big)\big(\kappa(s)-\sigma(s)\big)^n \\
& - \big(\kappa(s)-\sigma(s)\big)\big(\kappa(s)+\sigma(s)\big)^n\Big]\Big\},
\end{aligned} \tag{42}
$$

where

$$\kappa(s) = s + \lambda + \mu \tag{43}$$

and

$$\sigma(s) = \sqrt{s^2 + (\lambda-\mu)^2 + 2s(\lambda+\mu)}. \tag{44}$$

B. System with one-place buffer

Let us consider the original $GI/M/1/N$−type system with $N=2$ i.e. with the one-place buffer only.

It is easy to verify that the system of equations (13)–(14) can be written now in the following form:

$$
\begin{cases}
B_0^{(1)}(s) = f(s)B_1^{(1)}(s) + \frac{1-f(s)}{s}, \\
B_1^{(1)}(s) = B_1^{(1)}(s)\big(f(s) - f(s+\mu)\big) + \frac{1-f(s)}{s}.
\end{cases} \tag{45}
$$

Hence we eliminate $B_0^{(s)}(s)$ and $B_1^{(1)}(s)$ as follows:

$$
\begin{cases}
B_0^{(1)}(s) = \frac{\big(1-f(s)\big)\big(1+f(s+\mu)\big)}{s\big(1-f(s)+f(s+\mu)\big)}, \\
B_1^{(1)}(s) = \frac{1-f(s)}{s\big(1-f(s)+f(s+\mu)\big)}.
\end{cases} \tag{46}
$$

From the definitions (8) and (12) follows that

$$\mathbf{E}\beta_n^{(1)} = B_n^{(1)}(0). \tag{47}$$

Besides, let us note that

$$\lim_{s \to 0} \frac{1-f(s)}{s} = -\lim_{s \to 0} f'(0) = \mathbf{E}F, \tag{48}$$

where $\mathbf{E}F$ denotes the mean of interarrival times.

Now the identities (45) easily lead to

$$\mathbf{E}\beta_0^{(1)} = \mathbf{E}F f^{-1}(\mu)\big(1 + f(\mu)\big) \tag{49}$$

and

$$\mathbf{E}\beta_1^{(1)} = \mathbf{E}F f^{-1}(\mu), \tag{50}$$

thus

$$\mathbf{E}\beta_0^{(1)} = \mathbf{E}F + \mathbf{E}\beta_0^{(1)}. \tag{51}$$

The formula (51) has, obviously, very simple intuitive explanation: in the system with one-place buffer the mean of the time to the first buffer saturation in the system that begins its evolution being empty ($\mathbf{E}\beta_0^{(1)}$), is a sum of the mean of a waiting time for the first arriving packet ($\mathbf{E}F$) and the mean of the time to the first buffer saturation with one packet present ($\mathbf{E}\beta_1^{(1)}$). Of course, similar conclusions can be obtained in general case, basing on equations of the system (13)–(14).

In the case of the Poisson process with intensity λ describing the input flow of packets the formulae (49)–(50) simplify to the forms

$$\mathbf{E}\beta_0^{(1)} = \frac{2\lambda+\mu}{\lambda^2} \quad \text{and} \quad \mathbf{E}\beta_1^{(1)} = \frac{\lambda+\mu}{\lambda^2}. \tag{52}$$

VI. Numerical results

In this section we present sample numerical computations illustrating theoretical results obtained in Theorem 2. All computations are executed using the *Mathematica* environment.

Example 1.

Let us take into consideration the $E_3/M/1/3$-type system in which interarrival times have 3-Erlang distributions with parameter λ i.e.

$$F(t) = 1 - e^{-\lambda t}\big(1 + \lambda t + \frac{1}{2}\lambda^2 t^2\big), \quad t > 0. \tag{53}$$

The traffic load of the system equals $\rho = \frac{\lambda}{3\mu}$, where μ denotes the service rate.

In Table I the values of $\mathbf{E}\beta_0^{(1)}$, $\mathbf{E}\beta_1^{(1)}$ and $\mathbf{E}\beta_2^{(1)}$ are presented for different values of parameter λ and, in consequence, for different values of the traffic load ρ, decreasing from 4.00 to 0.17. Results in Table I are obtained keeping $\mu = 1$.

TABLE I
MEAN TIME TO BUFFER SATURATION IN $E_3/M/1/3$ QUEUE IN FUNCTION OF ARRIVAL RATE

No.	Parameter λ	Traffic load ρ	$\mathbf{E}\beta_0^{(1)}$	$\mathbf{E}\beta_1^{(1)}$	$\mathbf{E}\beta_2^{(1)}$
1	12.0	4.00	0.89862	0.64862	0.33077
2	9.0	3.00	1.28063	0.94730	0.49005
3	7.0	2.33	1.78334	1.35477	0.71504
4	5.0	1.67	2.90999	2.30999	1.27319
5	4.0	1.33	4.19696	3.44696	1.98212
6	3.0	1.00	7.21125	6.21125	3.84088
7	2.5	0.83	10.7058	9.50584	6.21304
8	2.0	0.67	18.5859	17.0859	12.0234
9	1.0	0.33	183	180	156
10	0.5	0.17	4218	4212	4050

Obviously, as one can note, the values of the mean of the time to the first buffer saturation increase with decreasing traffic load ρ. As it is intuitively clear, the values of $\mathbf{E}\beta_2^{(1)}$ are essentially smaller than the corresponding values of $\mathbf{E}\beta_1^{(1)}$ and $\mathbf{E}\beta_0^{(0)}$: in the case of $n = 2$ packets present in the system initially, the buffer saturation begins if only the first arrival instant "outruns" the first service completion epoch.

Results from Table I are presented geometrically in Figure 1 (nos. 1–8), where dotted, dashed and solid lines correspond to the values of $\mathbf{E}\beta_0^{(1)}$, $\mathbf{E}\beta_1^{(1)}$ and $\mathbf{E}\beta_2^{(2)}$ respectively.
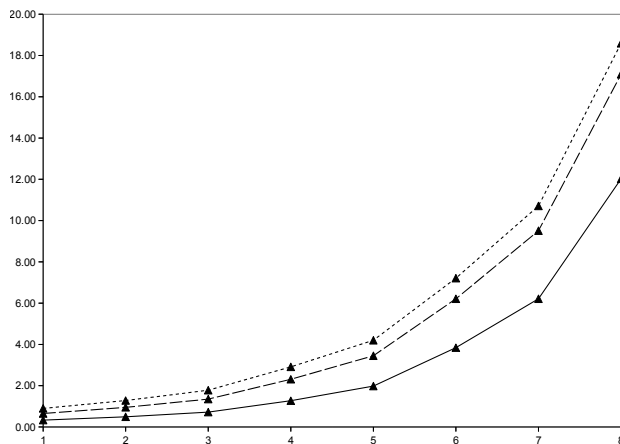

Fig. 1. Mean time to buffer saturation in $E_3/M/1/3$ queue in function of arrival rate (nos. 1-8)

In Table II (see also Figure 2) the values of the mean time to the first buffer saturation, under different initial conditions of the system, are presented in function of the service rate μ. Results in Table II are obtained taking $\lambda = 3$ (so $\rho = \frac{1}{\mu}$).

Example 2.

Let us consider now the $D/M/1/3$−type queuing system in which interarrival times have deterministic distributions i.e. the arriving packets occur at constant intervals equal Δ. Assume

TABLE II
MEAN TIME TO BUFFER SATURATION IN $E_3/M/1/3$ QUEUE IN FUNCTION OF SERVICE RATE

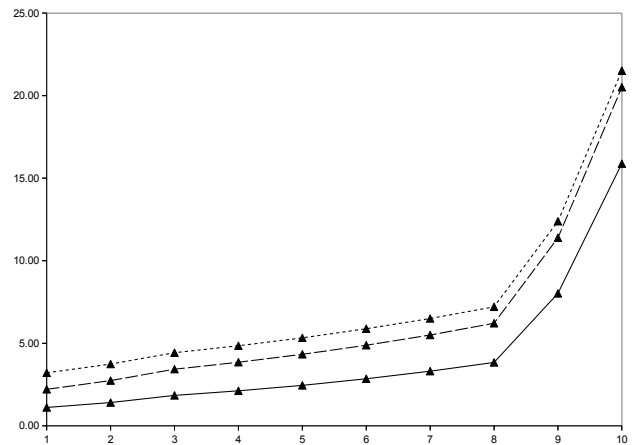| No.	Service rate μ	Traffic load ρ	$\mathbf{E}\beta_0^{(1)}$	$\mathbf{E}\beta_1^{(1)}$	$\mathbf{E}\beta_2^{(1)}$
1	0.1	10.00	3.21402	2.21402	1.11065
2	0.3	3.33	3.73956	2.73956	1.40856
3	0.5	2.00	4.42903	3.42903	1.84107
4	0.6	1.67	4.84998	3.84998	2.12198
5	0.7	1.43	5.33077	4.33077	2.45474
6	0.8	1.25	5.87897	4.87897	2.84667
7	0.9	1.11	6.50281	5.50281	3.30581
8	1.0	1.00	7.21125	6.21125	3.84088
9	1.5	0.67	12.3906	11.3906	8.01563
10	2.0	0.50	21.5075	20.5075	15.8779

Fig. 2. Mean time to buffer saturation in $E_3/M/1/3$ queue in function of service rate

that the service rate equals $\mu = 2$, so the traffic load in the system can be expressed as $\rho = \frac{1}{2\Delta}$.

In Table III the values of $\mathbf{E}\beta_0^{(1)}$, $\mathbf{E}\beta_1^{(1)}$ and $\mathbf{E}\beta_2^{(1)}$ are presented for 10 different values of the constant interarrival times Δ, namely from 0.1 to 1.0 with step 0.1. Let us note that, simultaneously, the traffic load ρ changes from 5 to 0.5, respectively, thus the regime of the system operation changes from the overloaded to the underloaded one.

TABLE III
MEAN TIME TO BUFFER SATURATION IN $D/M/1/3$ QUEUE IN FUNCTION OF ARRIVAL RATE

No.	Parameter Δ	Traffic load ρ	$\mathbf{E}\beta_0^{(1)}$	$\mathbf{E}\beta_1^{(1)}$	$\mathbf{E}\beta_2^{(1)}$
1	0.1	5.00	0.34690	0.24690	0.12475
2	0.2	2.50	0.82413	0.62413	0.32576
3	0.3	1.67	1.51469	1.21469	0.66805
4	0.4	1.25	2.55926	2.15926	1.26904
5	0.5	1.00	4.19453	3.69453	2.33539
6	0.6	0.83	6.81549	6.21549	4.22342
7	0.7	0.71	11.0758	10.3758	7.53716
8	0.8	0.63	18.0486	17.2486	13.2861
9	0.9	0.56	29.4827	28.5827	23.1380
10	1.0	0.50	48.2091	47.2091	39.8200

The interpretation of results in Table III is similar to that in Table I. Additionally, let us observe in practice the realization of the equation (51): in the case of the $D/M/1/N$−type system we have $\mathbf{E}\beta_1^{(1)} = \mathbf{E}\beta_0^{(0)} + \Delta$ (see remark on the equation (51). Results from Table III are presented geometrically

in Figure 3, where, as previously, dotted, dashed and solid lines correspond to the values of $\mathbf{E}\beta_0^{(1)}$, $\mathbf{E}\beta_1^{(1)}$ and $\mathbf{E}\beta_2^{(2)}$ respectively.
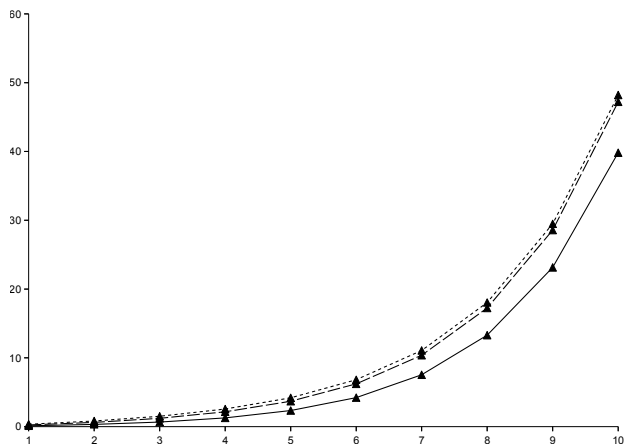

Fig. 3. Mean time to buffer saturation in $D/M/1/3$ queue in function of arrival rate

Finally, in Table IV (see also Figure 4) the values of the mean time to the first buffer saturation, under three different initial conditions of the operation of the system, are given in function of the service rate μ. Results in Table IV are obtained taking $\Delta = 2$ (so $\rho = \frac{1}{2\mu}$).

TABLE IV
MEAN TIME TO BUFFER SATURATION IN $D/M/1/3$ QUEUE IN FUNCTION OF SERVICE RATE

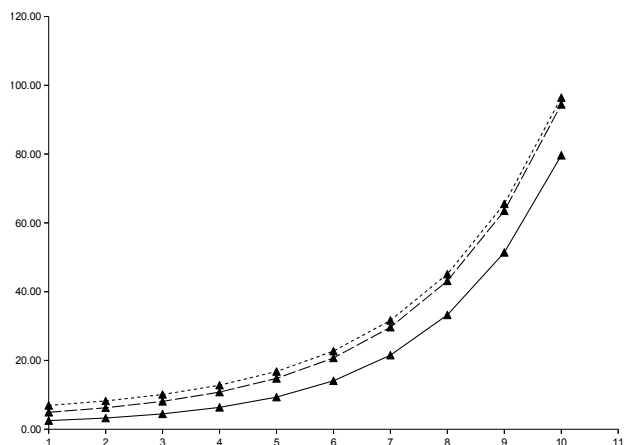| No.	Service rate μ	Traffic load ρ	$\mathbf{E}\beta_0^{(1)}$	$\mathbf{E}\beta_1^{(1)}$	$\mathbf{E}\beta_2^{(1)}$
1	0.1	5.00	6.93789	4.93789	2.49509
2	0.2	2.50	8.24127	6.24127	3.25762
3	0.3	1.67	10.0979	8.09793	4.45369
4	0.4	1.25	12.7963	10.7963	6.34520
5	0.5	1.00	16.7781	14.7781	9.34155
6	0.6	0.83	22.7183	20.7183	14.0781
7	0.7	0.71	31.6451	29.6451	21.5347
8	0.8	0.63	45.1214	43.1214	33.2154
9	0.9	0.56	65.5170	63.5170	51.4177
10	1.0	0.50	96.4182	94.4182	79.6401

Fig. 4. Mean time to buffer saturation in $D/M/1/3$ queue in function of service rate

VII. CONCLUSION

In the article distributions of times to successive buffer saturations are analyzed in the $GI/M/1/N$-type finite-buffer queue with general independent input stream of packets and exponentially distributed service times. The method of potential is applied to obtain the representation for the Laplace transform of the conditional distribution of the time to the first period of buffer saturation. Moreover, a formula for the tail of the distribution function of the "waiting" time to reaching the kth saturation of the buffer, for $k \geq 2$, is proved. The formula expresses the distribution of the time to next buffer overflows in terms of the conditional distribution of the time to the first buffer saturation. Some important special systems are discussed separately, namely the case of the system with Poisson arrival stream of packets and with one-place buffer. Numerical examples illustrating theoretical results are included as well, where the cases of the 3-Erlang and deterministic distributions of interarrival times are investigated.

REFERENCES

[1] A. Chydzinski, R. Winiarczyk, "Distribution of the first buffer overflow time in a deterministic service time queue," in *Computers and Communications, 2005. ISCC 2005. Proceedings of IEEE symposium on Computers and Communications*, 2005, pp. 637–641.
[2] A. Chydzinski, "Time to reach buffer capacity in a $BMAP$ queue," *Stochastic Models*, vol. 23, pp. 195–209, 2007.
[3] A. Chydzinski, "Time to buffer overflow in an $MMPP$ queue," *Lecture Notes in Computer Science*, vol. 4479, pp. 879–889, 2007.
[4] J. W. Cohen, *The Single Server Queue*. Amsterdam - New York - Oxford: North-Holland Publishing Company, 1982.
[5] R. B. Cooper, *Introduction To Queueing Theory*, North Holland, 1981.
[6] A. Al Hanbali, "Busy period analysis of the level dependent $PH/PH/1/K$ queue," *Queueing Syst.*, vol. 67, pp. 221–249, 2011.
[7] W. M. Kempa, "On main characteristics of the $M/M/1/N$ queue with single and batch arrivals and the queue size controlled by AQM algorithms, " *Kybernetika*, vol. 47, no. 6, pp. 930–943, 2011.
[8] W. M. Kempa, "Departure process in finite-buffer queue with batch arrivals, " *Lecture Notes Compt. Science*, vol. 6751, pp. 1–13, 2011.
[9] W. M. Kempa, "The virtual waiting time in a finite-buffer queue with a single vacation policy, " *Lecture Notes Compt. Science*, vol. 7314, pp. 47–60, 2012.
[10] V. S. Korolyuk, *Boundary-value problems for complicated Poisson processes*. Kiev: Naukova Dumka, 1975 (in Russian).
[11] V. S. Korolyuk, M. S. Bratiichuk, B. Pirdzhanov, *Boundary-value problems for random walks*. Ashkhabad: Ylym, 1987 (in Russian)
[12] E. Y. Lee, K. K. J. Kinateder, "The expected wet period of finite dam with exponential inputs," *Stochastic Processes and Applications*, vol. 90, pp. 175–180, 2000.
[13] H. Takagi, *Queueing Analysis, vol. 2. Finite Systems*. Amsterdam: North-Holland, 1993.
[14] O. Tikhonenko, W. M. Kempa, "The generalization of AQM algoritms for queueing systems with bounded capacity," *Lecture Notes in Computer Science*, vol. 7204, 242–251, 2012.
[15] O. Tikhonenko, W. M. Kempa, "Queue-size distribution in $M/G/1$-type system the with bounded capacity and packet dropping," *Lect. Notes Commun. Compt. Inf. Science* (accepted for publication)

Wojciech M. Kempa received his M.S. (from Silesian University of Technology) and Ph.D. (from Wroclaw University of Technology) degrees in mathematics in 1998 and 2003, respectively. He is currently employed as an Assistant Professor in the Institute of Mathematics at Silesian University of Technology in Gliwice, Poland. His scientific interests focus on queuing systems and computer networks, stochastic modeling and different aspects of operations research.

RAIT: the Rational Approximation and Interpolation Toolbox for Matlab, with Experiments on ECG Signals

Péter Kovács, Levente Lócsi

Abstract—**There is a wide range of applications of rational function systems. Including in system, control theories and signal processing. A special class of rational functions, the so-called Blaschke functions and the orthonormal Malmquist–Takenaka (MT) systems are effectively used for representing signals especially electrocardiograms.**

We present our project on a general MATLAB library for rational function systems and their applications. It contains Blaschke functions, MT systems and biorthogonal systems. We implemented not only the continuous but the discrete versions as well, since in applications the latter one is needed. The complex and real interpretations are both available. We also built in methods for finding the poles automatically. Also, some interactive GUIs were implemented for visual demonstration that help the users in understanding the roles of certain parameters such as poles, multiplicity etc.

Keywords—**Complex rational function systems, Digital signal processing, Discretization, Malmquist–Takenaka system, Matlab toolbox.**

I. INTRODUCTION

Rational function systems play an important role in signal processing [1], for instance there is a wide range of their application in system and control theories, see [2]. These systems proved to be appropriate for system identification, furthermore they can be used for denoising and compression. In a wide variety of problems the may also provide a nice and compact representation of the given signal [3]. We have applied our tools mostly for analyzing electrocardiograms (ECG signals).

We present our toolbox for Mathworks MATLAB environment. Our aim was to construct a toolbox that is independent of the particular problem and can be used for processing signals generally.

Many methods and related theoretical results incorporated and implemented in this project. It contains Blaschke functions, Malmquist–Takenaka systems, and also biorthogonal systems to some elementary rational bases [4]. We implemented not only the continuous but the discrete versions as well [5]. Complex and real interpretations are both available. The used systems depend on some parameters, or 'inverse

P. Kovács is with the Department of Numerical Analysis, Eötvös L. University, Budapest, 1117 Hungary (phone: 36-1-372-2500/8471; e-mail: kovika@inf.elte.hu).

L. Lócsi is also with the Department of Numerical Analysis, Eötvös L. University, Budapest, 1117 Hungary (e-mail: locsi@inf.elte.hu).

poles'. The Nelder–Mead simplex method can be used for finding these parameters automatically [6]. Also, some interactive graphical user interfaces (GUI) have been designed. They help the users in understanding how these function systems and methods work, and one can see the effects of certain parameters in action. So the toolbox is also fit for educational purposes.

The toolbox can be downloaded from

http://numanal.inf.elte.hu/~locsi/rait/

The outline of this article is as follows. In Section II we summarise the mathematical methods, and rational function systems used in our tools: Blaschke functions, Malmquist–Takenaka systems, discretization properties, biorthogonal systems and the Nelder–Mead simplex method. In Section III we give a list of possible applications in signal processing. We provide a short reference for the available programs and commands in Section IV, the GUI is demonstrated in Section V. Finally we show two examples for the applications of these tools in the case of real world signals in Section VI.

II. MATHEMATICAL BACKGROUND

In this Section we outline the mathematical concepts behind our toolbox.

Let us denote the set of complex numbers by $\mathbb{C}$, the open unit disc by $\mathbb{D} := \{ z \in \mathbb{C} : |z| < 1 \}$, and the unit circle (or torus) by $\mathbb{T} := \{ z \in \mathbb{C} : |z| = 1 \}$. Furthermore let $\mathbb{N} := \{ 1, 2, 3, \dots \}$.

A. Blaschke functions and products

In this construction the Blaschke functions play an important role. Blaschke functions are complex valued functions of one complex variable, depending on the parameter $a \in \mathbb{D}$. They are defined as follows:

$$B_a(z) := \frac{z - a}{1 - \overline{a}z} \qquad (z \in \mathbb{C} \setminus \{ 1/\overline{a} \}).$$

Blaschke functions have many interesting properties. They are bijections of both $\mathbb{D}$ and $\mathbb{T}$. Furthermore they can be interpreted as the congruencies of the hyperbolic plane in the Poincaré disc model.

Blaschke products are finite products of Blaschke functions. For given $1 < m \in \mathbb{N}$ and $a_1, \ldots, a_m \in \mathbb{D}$ the Blaschke product of order m is defined as follows:

$$B_{a_1,\ldots,a_m} := \prod_{j=1}^{m} B_{a_j}(z).$$

A Blaschke product of order m is an m-fold map on $\mathbb{T}$, i.e. for all $w \in \mathbb{T}$ there exist exactly m values, $z_1, \ldots, z_m \in \mathbb{T}$, that are mapped to w.

The Blaschke functions appear (in connection with the below) when we need to calculate an appropriate discretization on $\mathbb{T}$, and also in the product form of the orthogonal Malmquist–Takenaka functions.

B. Basic rational functions

The elementary building blocks in the toolbox are the complex rational functions of the form

$$r_{a,k}(z) = \frac{1}{(1 - \overline{a}z)^k},$$

with $a \in \mathbb{D}, k \in \mathbb{N}$. The parameter a is sometimes referred to as an *inverse pole* (because $1/\overline{a}$ is a pole in the standard sence), r_k is said to be a *basic function of order k*. Using a terminology similar to the trigonometric case, the value $k = 1$ corresponds to the *fundamental tone* and $k > 1$ the *overtones*.

Usually we take the restriction of the functions on the unit circle, which we identify with the $[-\pi, \pi)$ real interval, in our toolbox. To this order we apply the map $t \mapsto e^{it} \in \mathbb{T}$. Then the real part and the imaginary part can both be used for signal processing purposes.

Applying this process to basic rational functions the generated real valued functions shows similarities to certain types of signals. For instance they fit very well to different parts of an ECG signal. We note that this process is very adaptive.

The linear combinations of the $r_{a,k}$ functions can be applied to more general signals. They are of the form

$$\sum_{k=1}^{n} c_k r_{a_k,k} \qquad (c_k \in \mathbb{C}).$$

In our model a signal will be represented as such a linear combination. In order to do that we should find proper inverse poles and coefficients. In the following subsections we will discuss our approach (also implemented in the toolbox) to these problems.

We also mention that in some cases the so-called 'modified' basic rational functions are more appropriate. They are of the form

$$\frac{z^{k-1}}{(1 - \overline{a}z)^k} \qquad (a \in \mathbb{D}, \ k \in \mathbb{N}).$$

They span the same subspace of the functions analytic on $\overline{\mathbb{D}}$ as the corresponding basic rational functions.

C. Malmquist–Takenaka systems

Both the basic rational functions and their modified versions form a linearly independent set of functions. An orthogonal system however would be more useful in applications, since the coefficients are easy to calculate in this case.

The Malmquist–Takenaka (MT) systems are orthogonal systems of functions. We generate these systems by the Gram–Schmidt orthogonalization applied to a finite set or to a sequence of basic rational functions. The corresponding scalar product used on $\mathbb{T}$ is:

$$\langle F, G \rangle = \frac{1}{2\pi} \int_{-\pi}^{\pi} F(e^{it})\overline{G}(e^{it})\,\mathrm{d}t \qquad (F, G \in H^2(\mathbb{D})). \quad (1)$$

Naturally we use a discrete approximation of this integral in the toolbox.

A handy property of the MT systems is that their elements can be expressed as Blaschke products. Namely, taking the basic functions for a given $m \in \mathbb{N}$ and $a_1, \ldots, a_m \in \mathbb{D}$ the orthogonalized MT system can be written as:

$$\Phi_k(z) = \frac{\sqrt{1 - |a_k|^2}}{1 - \overline{a_k}z} \prod_{j=1}^{k-1} B_{a_j}(z),$$

with $1 \le k \le m$.

D. Discretization

In practice the discrete orthogonal systems are very useful. It is known that in the trigonometric case the discrete system is generated by uniform discretization of $\mathbb{T}$. For the MT system we had to find a proper non-uniform sampling of $\mathbb{T}$ and a weight function in the discrete scalar product to obtain a discrete orthogonal system.

In the definition of the set of discrete points, again, Blaschke products play an important role. In this respect the key fact is that B_a is a $\mathbb{T} \to \mathbb{T}$ bijection. This led us to the definition of the *argument function* associated to the Blaschke function B_a $(a \in \mathbb{D})$:

$$\beta_a : [-\pi, \pi) \to \mathbb{R} \qquad \beta_a(t) := \arg B_a(e^{it}).$$

In calculations it is useful to have an explicit form for β_a

$$\beta_a(t) = (\delta + \varphi) + 2\arctan\left(\frac{1+r}{1-r}\tan\frac{t-\varphi}{2}\right),$$

where $a = re^{i\varphi}$.

One can think of $\delta \in [-\pi, \pi)$ as a correction term: we can make sure that β_a will map the interval $[-\pi, \pi)$ onto itself. The function β_a is strictly increasing and invertible.

For Blaschke products we define the argument function in the following way:

$$\beta_{a_1,\ldots,a_m}(t) := \frac{1}{m}\arg\prod_{j=1}^{m} B_{a_j}(z) = \frac{1}{m}\sum_{j=1}^{m}\beta_{a_j}(t).$$

The $1/m$ factor is applied to maintain the $[-\pi, \pi)$ bijection property.

Let us consider the set of $N \in \mathbb{N}$ equidistant points

$$D_0^N := \left\{ -\pi + k \cdot \frac{2\pi}{N} : 0 \le k \le N - 1 \right\} \subset [-\pi, \pi).$$

Then for given $1 \leq m \in \mathbb{N}$, and $a_1, \ldots, a_m \in \mathbb{D}$ parameters the set

$$D^N_{a_1,\ldots,a_m} := \left\{ \beta^{-1}_{a_1,\ldots,a_m}(t) \,:\, t \in D^N_0 \right\} \subset [-\pi, \pi) \qquad (2)$$

is a *non-equidistant N point discretization* of the interval $[-\pi, \pi)$.

We note that when $m = N$ the Malmquist–Takenaka system is also orthogonal with respect to the discrete scalar product on the above defined discretization points:

$$[F, G]_N := \sum_{t \in D^N_{a_1,\ldots,a_m}} F(e^{it}) \overline{G}(e^{it}) \rho_N(e^{it}), \qquad (3)$$

with the weight function $\rho_N(e^{it}) = 1/\beta'_{a_1,\ldots,a_m}(t)$.

In the case of the discrete complex MT system real valued functions have to be extended with its imaginary parts before the MT expansions has been calculated. We should use the discrete real MT systems if we want to compute the MT coefficients directly. Now, let insert a zero pole into the pole vector $\mathbf{a} = \{0, a_1, \ldots, a_m\}$ and consider the following discretization

$$DR^N_0 = \left\{ -\pi + k \cdot \frac{\pi}{N} \,:\, 0 \leq k \leq 2N - 2 \right\} \in [-\pi\ \pi) \,.$$

Then for a given pole vector we can define the discretization set on the analogy of (2):

$$DR^N_{0,a_1,\ldots,a_m} = \left\{ \beta^{-1}_{0,a_1,\ldots,a_m}(t) \,:\, t \in DR^N_0 \right\} \in [-\pi\ \pi) \,.$$

The real valued MT system that corresponds to the pole vector $\mathbf{a}$ is defined as follows

$$U_0 = 1,\ V_0 = 0,\ U_n = \mathrm{Re}(\Phi_n),\ V_n = \mathrm{Im}(\Phi_n)\ \ (n \in \mathbb{N}) \,.$$

It can be proved that in the case of $m = N - 1$ the real MT system $(U_n, V_n, 0 \leq n \leq m)$ is also orthonormed system with respect to the discrete real scalar product

$$[F, G]^R_N = \sum_{t \in DR^N_{0,a_1,\ldots,a_m}} F(e^{it}) G(e^{it}) \rho^R_N(e^{it}) \,,$$

where ρ^R_N denotes the discrete real weight function

$$\rho^R_N(e^{it}) = 1/(2\,\mathrm{Re}\,\beta'_{0,a_1,\ldots,a_m}(t) - 1) \,.$$

E. Biorthogonal systems

As it was mentioned above, signals can be easily represented by using MT systems. We only need to calculate the coefficients of the MT expansions by computing continuous or the discrete scalar products. However in some special cases it can be beneficial to work with the original rational base functions instead of the orthonormal MT systems. For instance, this is the case of system identification when a partial fraction representation of the transfer function is taken, and the poles should be determined [7]. Furthermore, in contrast with the MT systems (Fig. 1), the biorthogonal systems (Fig. 2) are independent from the order of the poles. We take $n + 1$ different poles $a_0, \ldots, a_n$ with multiplicities $m_0, \ldots, m_n$ and the corresponding base functions

$$\phi_{k,i}(z) = \frac{z^{i-1}}{(1 - \overline{a}_k z)^i} \qquad (k = 0, \ldots, n,\ i = 1, \ldots, m_k) \,.$$

(a) Coefficients.

(b) Real part of the MT basic functions.

(c) Coefficients.
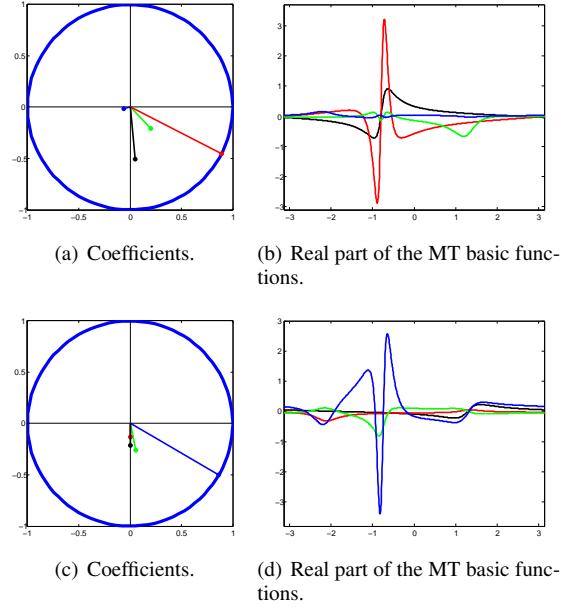
(d) Real part of the MT basic functions.

Fig. 1.   MT system defined by the same poles but in different order.

For the definition of the biorthogonal system we will need the following functions

$$\Omega_{\ell n}(z) = \frac{1}{(1 - \overline{a}_\ell z)^{m_\ell}} \prod_{i=0, i\neq \ell}^{n} B^{m_i}_{a_i}(z) \,,$$

$$\omega_{\ell n}(z) = \frac{\Omega_{\ell n}(a_\ell)}{\Omega_{\ell n}(z)}$$

where $(0 \leq \ell \leq n)$.

By Theorem 1 in [4] the functions

$$\Psi_{\ell,j}(z) = \frac{\Omega_{\ell n}(z)(z - a_\ell)^{j-1}}{\Omega_{\ell n}(a_\ell)} \sum_{s=0}^{m_\ell - j} \frac{\omega^{(s)}_{\ell n}(a_\ell)}{s!}(z - a_\ell)^s$$

$(0 \leq \ell \leq n,\ 1 \leq j \leq m_\ell)$ are biorthogonal to $\phi_{k,i}$ with respect to the scalar product defined by (1). As a result the biorthogonal expansion of an $f \in \Re$ function can be easily calculated as follows

$$P_N f = \sum_{k=0}^{n} \sum_{i=1}^{m_k} \langle f, \Psi_{ki} \rangle \phi_{ki} \,,$$

where $N = m_0 + m_1 + \cdots + m_n$.

Moreover it was shown in Theorem 2 in [4] that the systems $\phi_{k,i}$ and $\Psi_{\ell,j}$ are also biorthogonal with respect to the discrete scalar product defined by (3),

$$[\Psi_{\ell r}, \phi_{ks}]_N = \delta_{k\ell}\delta_{rs} \,,$$

where $(1 \leq r \leq m_\ell,\ 1 \leq s \leq m_k,\ 0 \leq k, \ell \leq n) \,.$

F. Optimization method

If the poles and the multiplicities, and so the basic rational functions are given then the orthogonal and the biorthogonal expansion can be calculated as described above. The next issue is the choice of the best possible poles and multiplicities.
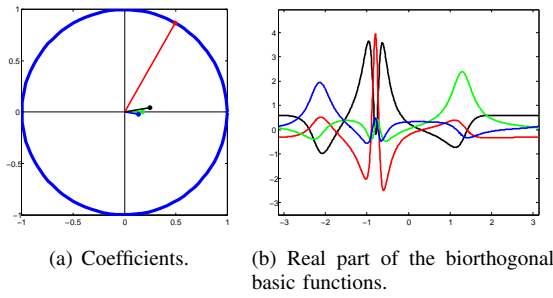
(a) Coefficients. (b) Real part of the biorthogonal basic functions.

Fig. 2. Biorthogonal system.

(a) Projection onto $\Re_N$. (b) Approximation error.

Fig. 4. Approximating real signals by taking lead 3 of record *s0301lre* from ptbdb database of Physionet [9].
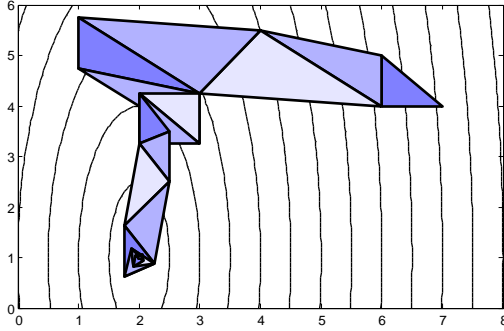

Fig. 3. The steps of the Nelder–Mead simplex algorithm minimizing a quadratic function of two variables.

In other words we want to minimize the distance of the subspace spanned by the basic rational functions with the given parameters from the original signal. For the solution of this optimization problem we have implemented the Nelder–Mead simplex method [8].

This algorithm is an iterative method for the minimization of an arbitrary real valued function of several variables. It is widely used in natural and engineering sciences and it is also mathematically studied. Its basic idea is a step-by-step improvement by means of geometric transformations of a simplex (i.e. in 2 dimensions a triangle). For a detailed description we refer to the original article [8], and for a recent application [6].
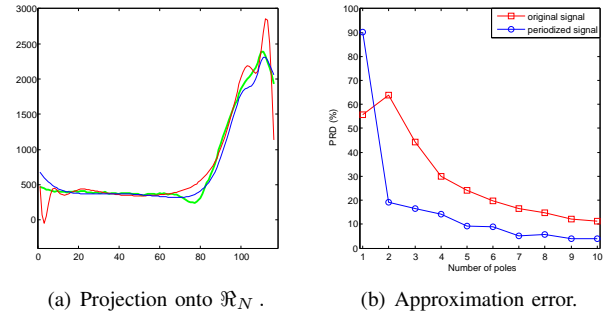
Fig. 3 shows a simple example for the application of the Nelder–Mead method.

An additional difficulty is that the original Nelder–Mead method is defined in $\mathbb{R}^n$, but in our case the parameters must stay within $\mathbb{D}$. Therefore we used a $\mathbb{R}^n \to \mathbb{D}$ bijective map to adjust the algorithm for our case.

We note that different versions of this algorithm have been implemented according to the function systems, i.e. discrete, continuous, complex, real.

III. APPLICATION IN SIGNAL PROCESSING

We provide procedures to handle discrete datasets and signals. If the discrete versions of the systems are used then the values of the signal must be evaluated at non-equidistant discretization points. It means that we have to resample the signal as well. We have implemented this method by using linear interpolation between uniform sampling points.

In order to improve the accuracy of the approximation we had to transform the signals to 2π periodic functions. In particular we had to make sure that the values at the end points are equal. In our implementation we wanted to avoid using such filters that distort the original signal. The preprocessing steps were carried out as follows. First we applied Savitzky–Golay FIR smoothing filter by using second order polynomials and width frame size equal to 11 samples. We used this smoothed data to predict the sign of the slopes of the original signal. Then the signal was extended at the two endpoints by keeping the slopes and used vertical shift. Then a Tukey window was applied to generate a 2π periodic signal. The parameters of the window were set so that the constant one part of the window corresponded to the original signal and the transition part must be equal with the length of extension. Fig. 4. shows the difference between the approximations by using the original and the periodized signals. The effect of jump discontinuity at the endpoints can be seen as the red colored function starts to oscillate near to the ends of the interval.

IV. FUNCTION REFERENCE

In this section we introduce the main parts and the programs of the RAIT toolbox. Our functions can be divided into 6 classes which are enumerated in Table I.

We have three types of rational function systems, namely the biorthogonal, the basic rational and the MT systems. Three functions were implemented for all types of these systems to compute the values, the coefficients and the projection onto $\Re_N$. The names of the functions include the name and the type of the system and the operation that we want to execute. For instance, if we want to calculate the coefficients of a function with respect to the discrete complex MT system, then the abbreviation `mtdr_coeffs` should be used. We introduce the parameterization of these procedures along with the continuous MT system. All functions in the first three classes can be called the same way.

- `mt_system(len,poles)`. Calculates the values of the Malmquist–Takenaka system defined by the `poles` vector at `len` number of uniformly distributed points in the interval $[-\pi, \pi]$.
- `mt_coeffs(v,poles)`. Computes the Fourier coefficients of `v` with respect to the MT system defined by `poles`.

- `mt_generate(len,poles,coeffs)`. Generates a function in the space spanned by the MT system.

The Blaschke class includes the procedures that compute and visualize the values of the Blaschke functions. Additionally, the derivatives and the inverse of the argument function also belong to this directory. Let us consider the most important procedures of this class:

- `arg_fun(a,t)`. Calculate the values of the argument function of a Blaschke product at `t` defined by the pole vector `a`.
- `arg_inv(a,b,eps)`. Compute the inverse images of the argument function at the elements of `b`. In this case, the poles of the Blaschke product is defined by `a` and the accuracy is determined by the variable `eps`.
- `blaschkes_img(image,a,show)`. Transforms an `image` by applying the Blaschke function defined by poles `a`. In addition, the absolute values and the arguments of the projection are also calculated. E.g. Fig. 5 was generated by this procedure.

The problem of calculating the projection onto $\Re_N$ is twofold. On one hand, we need to find the best poles for the selected rational system to minimize the approximation error. On the other, hand we need to calculate the projection. The latter can be easily computed by using functions of the first three classes. The former can be solved by applying different types of simplex algorithms. We have implemented this method for the five types of rational systems so we can choose the one which is the best suited to the given problem.

- `simplex_mt(f,mul,period,init,show,eps)`. Gives the poles of the continuous MT system that best fit the approximation of the function `f`. The parameters `mul` and `period` determine the multiplicities and the periodicity of the pole vector. Initial values are defined by the `init` variable. Furthermore, the predicted poles can be displayed at each steps by setting true the value of the `show` parameter. We can control the accuracy of the process through the `eps` variable. All types of simplex algorithm are called consistently by using the right rational system abbreviation, such as `mtdc`, `mtdr`, `biort` etc.
- `coords2params(k)`. It is an important function that maps coordinates in $\mathbb{R}^2$ to parameters in $\mathbb{D}$. The (x,y) coordinates are given sequentially in the vector `k`.

There are several other procedures that implement operators in $H^2(\mathbb{D})$, perform conversations between systems, visualize rational functions etc. We present some of the most important methods below, but additional examples can be also found in Section VI.

- `addimag(v)`. Calculates the imaginary part of the function `v` using FFT. It should be used to compute the expansion of `v` with respect to the complex versions of the systems, such as `mt`, `mtdc`, `biort` etc.
- `coeff_conv(l,poles,coeffs,base1,base2)`. It converts the coefficients `coeffs` between the continuous systems `base1` and `base2`. Parameters `l` and `poles` define both of the systems. Furthermore, a similar function called `coeffd_conv` is also available

TABLE I
FUNCTION REFERENCE

Biort_sys	Rat_sys	MT_sys
biort_system	lf_system	mt_system
biort_coeffs	lf_generate	mt_coeffs
biort_generate	mlf_system	mt_generate
biortdc_system	mlf_coeffs	mtdc_system
biortdc_coeffs	mlf_generate	mtdc_coeffs
biortdc_generate	mlfdc_system	mtdc_generate
	mlfdc_coeffs	mtdr_system
	mlfdc_generate	mtdr_coeffs
		mtdr_generate

Blaschke	Simplex	Other
arg_der	simplex_mt	addimag
arg_fun	simplex_mtdc	bisection_order
arg_inv	simplex_mtdr	coeff_conv
arg_inv_anim	simplex_biort	coeffd_conv
argdr_inv	simplex_biortdc	discretize_dc
blaschkes	coords2params	discretize_dr
blaschkes_img	coords2params_all	dotdc
	multiply_poles	dotdr
	periodize_poles	kernel
		multiplicity
		rshow
		subsample
		periodize

to perform conversations between the discrete versions of the systems.

- `discretize_dc(poles,eps)`. Computes the non-equidistant complex discretization on the unit disc that refers to the given `poles`. The accuracy of the method can be set by the variable `eps`.

V. MATLAB GUI

Our aim was to construct a toolbox that is appropriate to a wide range of applications. Furthermore, we also want to help the users in understanding the effects of certain parameters of the systems. Accordingly two additional interactive MATLAB GUIs were implemented to demonstrate the role of poles, multiplicities etc.

The first GUI is called `blaschke_tool`. It can be used to visualize the connection between the position of the pole and the values of the argument function. It is also possible to display grayscale images that are projected onto the unit disc by Blaschke functions. E.g. Fig. 5(a) and Fig. 5(b) show that how the Blaschke functions transform the unit disc and how it depend from the poles. Furthermore, the absolute values and the arguments of the Blaschke function from Fig. 5(b) also can be seen on Fig. 5(c) and on Fig. 5(d).

Additional GUI called `malmquist_tool` were implemented to introduce and to describe the properties of the MT systems. We can determine the positions, the number and the multiplicities of the selected poles. The argument function is also displayed on the unit disc. Furthermore, all the members of the MT system can be visualized related to the defined poles. Additionally, not only the complex case, but the real type of MT expansions were implemented as well. It means that both real and complex discretization can be used for interpolation purposes. In addition, the results and the weight function of the two types of discrete scalar product can be
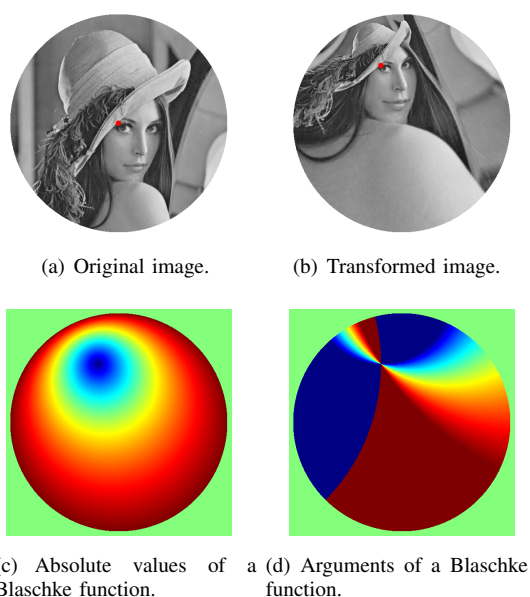
(a) Original image.

(b) Transformed image.

(c) Absolute values of a Blaschke function.

(d) Arguments of a Blaschke function.

Fig. 5.   Properties of a Blaschke function.

(a) Poles and multiplicities.

(b) Argument function.

(c) Real part of Φ_6.
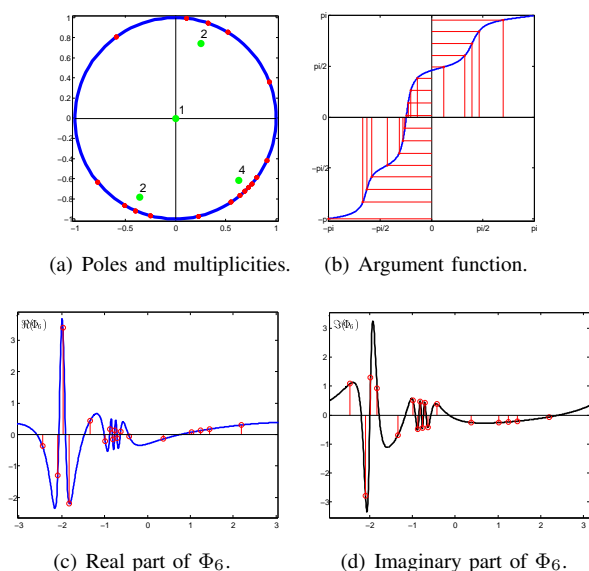

(d) Imaginary part of Φ_6.

Fig. 6.   Visualization of the MT systems defined by an appropriate pole vector.

calculated. All of these functions can be animated interactively by moving the poles in the unit circle. Fig. 6 shows some illustrations generated by the toolbox. On Fig. 6(a) one can see the poles and the real discretization on the unit disc determined by the argument function on Fig. 6(b). It illustrates well the fact that the points of discretization tends to be more dense near the pole as it gets closer to the torus. The real and the complex part of the 6th member of the related MT system is showed by Fig. 6(c) and Fig. 6(d).

VI. EXAMPLES

In this section we present some MATLAB instructions from the RAIT toolbox. We will give examples for both continuous and discrete approximations as well.

First, we start with a real ECG curve from the ptbdb database of Physionet [9]. Second, the simplex algorithm has been performed to find the best poles for the continuous MT system. Finally, we compute the coefficients and the MT expansion. We note that the original signal was extended by its imaginary part. As we shall see later, this step can be skipped if we use the discrete real MT system. This is achieved by the following code:

```
>> s=periodize(ecg,0.1,0);
>> s_im=addimag(s);
>> m=[1 2 1];
>> pr=2;
>> init=zeros(1,6);
>> p=simplex_mt(s,m,pr,init,0,1e-6);
>> mp=periodize_poles(multiply_poles(p,m),pr);
>> mtco=mt_coeffs(s_im,mp);
>> s_mt=mt_generate(length(s),mp,mtco);
```

We can get the reconstructed signal by taking the real part of the variable s_mt. On Fig. 1(d) one can see the poles of the MT system and the approximation. We note that the 6.92% percentage root mean square difference (PRD) was gained by using only 8 complex coefficients and 3 complex poles. The original signal contains about 900 samples per heartbeats.

If we convert the coefficients into the basic rational function system, we can separate the main diagnostic waves of the ECG curve. Using this method to analyse ECG curves is a very obvious intention since these waves express real diagnostic features. On Fig. 9 we can see that the MT basic functions do not reflect any diagnostic properties in contrast with the basic rational functions. On Fig. 9(b) the P, T waves and the QRS complex was generated by sorting the projections of the ECG curve by using the basic functions which were defined by the same pole. The following code separates the main waves of the ECG curve:

```
>> len=length(s);
>> lfco=coeff_conv(len,mp,mtco,'mt','lf');
>> lfs=lf_system(len,mp);
>> P=real(lfco([1,5])*lfs([1,5],:));
>> QRS=real(lfco([2,3,6,7])*lfs([2,3,6,7],:));
>> T=real(lfco([4,8])*lfs([4,8],:));
```

Let us consider the interpolation process of the toolbox. The approximation will be carried out like the continuous case. Now we use a segment of a central venous pressure (CVP) signal. After the best poles were found then the discrete coefficients can be calculated directly. We note that, there is no need to extend the original signal with its imaginary part. On Fig. 10(a) and Fig. 10(b) one can see the reconstructed signal. In the former case the approximation was carried out on 6 poles. The latter figure was obtained by duplicating the number of the poles periodically. Hence the same instructions were executed by setting the variable pr to 2. For instance, Fig. 10 was obtained as follows:

```
>> s=periodize(cvp,0.1,0);
>> len=length(s);
>> m=[1 3 2];
>> pr=1;
>> init=[-0.6,-0.6,0.2,0.7,-0.4,-0.6];
>> p=simplex_mtdr(s,m,pr,init,0,1e-6);
>> mp=periodize_poles(multiply_poles(p,m),pr);
```
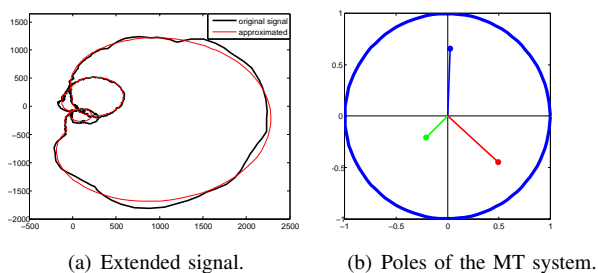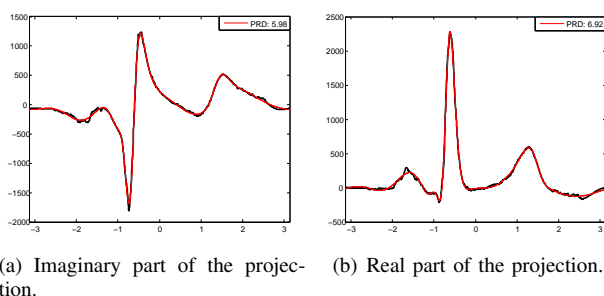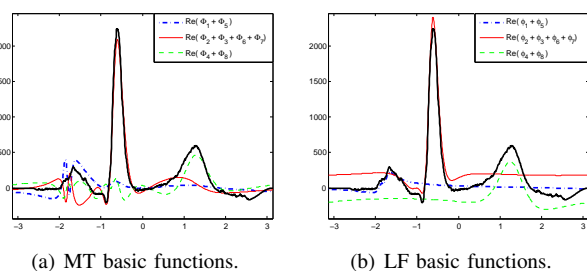
(a) Extended signal.   (b) Poles of the MT system.

Fig. 7.   Approximation steps.

(a) Imaginary part of the projection.   (b) Real part of the projection.

Fig. 8.   MT approximation of the record *s0306lrem* from ptbdb database of Physionet.

(a) MT basic functions.   (b) LF basic functions.

Fig. 9.   Basic functions of MT and LF systems.

(a) Approximation of the signal by using 6 poles.   (b) Approximation of the signal by using 12 poles.
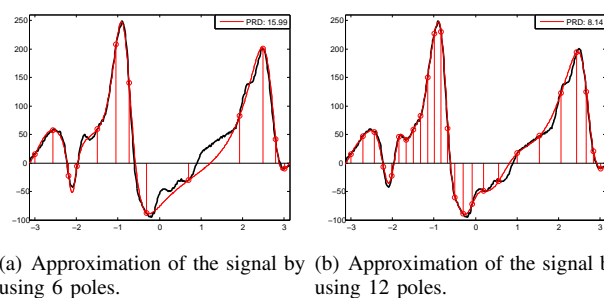
Fig. 10.   Real MT approximation of the record *mgh001* from mghdb database of Physionet.

```
>> [cUk,cVk]=mtdr_coeffs(s,mp,1e-6);
>> s_mtdr=mtdr_generate(len,mp,cUk,cVk);
```

VII. Experiments

In this section, we want to emphasize the efficiency of rational functions by compressing different types of signals. However, we have already given some examples for the practical applications of the systems, but comparsions have not

been presented yet. For this reason, we have performed experiments to compare the compression ratio and the accuracy of different algorithms in biomedical signal processing. We used the review [10] as a reference of the ECG signal compressing methods. To assess the quality of the results, we performed our tests on the two main classes of the ECG compression algorithms. Namely, we compared the performance of rational functions with wavelet and polynomial approximation based methods.

Furthermore, we want to use an objective measure of the level of compression and distortion rate. For this reason, synthesized ECG signals [13] were also used to test these methods. In this case, we can generate electrocardiograms with different diagnostical and geometrical features, but we can get the original signals in analytic forms as well. So, both compression and distortion rate can be measured by using different types of error measures, such as PRD and the so-called weighted diagnostic distortion (WDD) [14].

Wavelets are widely used in signal processing for not only compressing data, but for extracting different features as well. In our tests, a one dimensional discrete wavelet transform (DWT) was applied for ECG signals. It means that we generated 100 different synthetic ECG signals with normal diagnostic parameters by using the statistics of these features from [12]. This is a piecewise polynomial model with at most fifth order segments., therefore we used Daubechies wavelets having six vanishing moments (D6). These functions can be applied efficiently to compress our synthetic signals, because they can supress at least 5 order polynomials. The embedded MATLAB commands wdencmp and wpdencmp were used to perform the tests. The former one is a wavelet coefficient thresholding algorithm. The latter is an efficient implementation of the wavelet packets (WP) method. In contrast with the simple wavelet thresholding algorithms, the WP procedure is an adaptive transformation in the sense of the coefficient management. It means that both the approximation and the detailed coefficients are further decomposed at each level of the multiresulotion analysis. After this step, all the coefficients will be removed which have high entropy. The remaining terms are the 'best' optimal selection in the sense of Shannon entropy measure. We refer to [11] for details.

Now, let us consider the experiment. The aforementioned algorithms were applyed to the 100 synthetic ECG signals. During the compression the thresholds were decreased in each step until the desired 5% PRD was reached. Finally, the number of coefficients and the WDD were encountered for each method. Fig. 11 shows our results. One can see that if the MT representation was used then generally we need less number of coefficients than in the D6 wavelet decomposition. In the former case, the diagnostic distortion is better. As it was excepted, the WP algorithm has outperformed the simple wavelet thresholding method. Now, the average number of coefficients is about 30. However it is slightly better, but it is still comparable with the performance of the rational functions. Furthermore, the WDD of the MT approximation is the best among these there methods.

In our second experiment we used an additional compression algorithm. It is a polynomial approximation method where
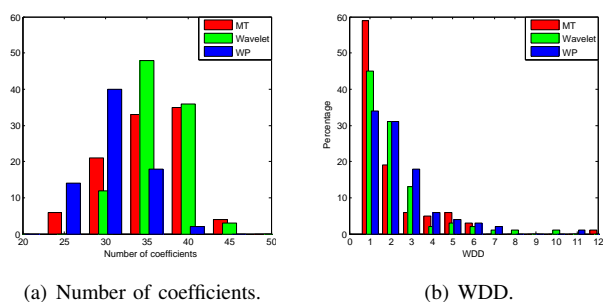
(a) Number of coefficients.   (b) WDD.

Fig. 11.   Statistics of the tested methods on 100 synthetic beats.

Fig. 12.   Statistics of the tested methods on 14 real ECG signals.

the base functions are b-splines. This is a simple procedure which starts with an initial spline approximation given by a large number of knots. The knots are then removed, one by one, until we reach a certain degree of distortion. The key point of this algorithm is the prediction of the error at each of the removed knots. By taking advantage of the fact that the beat to beat changes in ECG signals are generally not significant, the compression ratio of this algorithm can be further improved. But here we will use only the number of coefficients and knots to determine the related compression ratios for each beat. For proper algorithms see e.g. [16].

This test contains 14 real ECG signals of the mitdb database from Physionet [9]. Some preprocessing steps are necessary to deal with noise, but these algorithms are beyond the scope of this paper, we just enumerate the applied techniques, see references for further details. First of all, we segmented the signals into beats by taking into account the heart rate variability and the related statistics of the ECG signals from [12]. Then a simple baseline subtraction algorithm was used from [17] to deal with baseline wandering. Additionally the well known KLT transformation was also applied to filter out high frequency noises. Only the first few KLT basis function were computed by keeping 90% of the whole energy. The series of beats in a signal were aligned along with their R peaks. Furthermore, we calculated the KLT basis by using the SVD decomposition of 60 successive beats. The running SVD algorithm [15] were used to improve the speed of the preprocessing step. For further analysis see Chapters 5 and Appendix 9A from book [12].

In contrast with our previous experiment, now we fixed the number of coefficients that can be used by each of the tested algorithms. On one hand it means that the compression ratio is the same for all of these procedures. On the other hand the error of the approximation is different. The final results can be seen on Fig. 12. The average PRD was assigned to all of the related methods and records. As we expected, the b-spline approximation can not keep step with the other three methods. Otherwise, it is hard to distinguish the average PRDs in the latter case. So it is difficult to choose the algorithm that achieved the best scores. However, the red lines are almost always under the others. Which means that the rational function representation performed slightly better.

Our primary goal was to demonstrate the feasibility and applicability of the method. The potential application area can
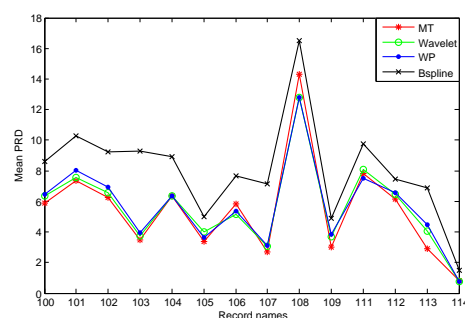
be extended to other types of datas thats are not necessary to be biomdecical or physiological signals. Although the rational functions systems did perform better than wavelets and wavelet packets on some experiments, but we do not claim that it generally outperforms them. Further research is required to answer these questions.

VIII. Conclusion

A new MATLAB toolbox has been introduced which can be useful in a wide range of applications. However, we proposed some practical applications for signal processing. For instance, these systems are capable to represent different types of signals. Taking advantage of approximation and interpolation properties not only equidistant but non-uniform discretization can be used as well. Four types of signal representations are available by using different classes of rational function systems. It is worth to examine other properties of these representations, for instance the energy compaction, compression rate, sense of the coefficients and the poles etc. A related open question is that of the filtering property, whether or not we can use these expansions for denoising signals. Two MATLAB GUIs were implemented for educational purposes. However, we want to extend the toolbox with real biorthogonal expansions by analogy with `mtdr` functions. In addition, we are working on a GUI called `biort_tool` similar to `malmquist_tool` that demonstrate the properties of biorthogonal systems.

Further research is required on finding the best poles for a system. We used the Nelder–Mead algorithm to resolve this problem, but it can terminate in local optima. An alternative solution could be applying the simplex algorithm partially. Another way is to use hyperbolic geometry instead of eucledian. Unfortunately, it is hard to generalize the operations in higher dimension such as computing bisectors, intersections, reflections etc. However, Blaschke functions can be useful to resolve this problem. In the near future, we also want to implement a similar toolbox involving hyperbolic operations, simplex algorithm and different models such as Poincaré disk and Cayley–Klein model.

References

[1] A. Soumelidis, F. Schipp, J. Bokor, "Frequency domain representation of signals in rational orthogonal bases," in *Proc. 10th Mediterranean*

Conference on Control and Automation–MED 2002, Lisbon, Portugal, p. on CD.

[2] P. S. C. Heuberger, P. M. J. Van den Hof, B. Wahlberg, *Modelling and Identification with Rational Orthogonal Basis Functions*. London, CA: Springer-Verlag, 2005, pp. 61–102.

[3] S. Fridli, L. Lócsi, F. Schipp, "Rational function system in ECG processing," in *Proc. 13th Int. Conf. Computer Aided Systems Theory– EUROCAST 2011, Part I (eds. R. Moreno-Díaz et al.)*, LNCS 6927, pp. 88–95.

[4] S. Fridli, F. Schipp, "Biorthogonal systems to rational functions," *Annales Univ. Sci. Budapest., Sect. Comp*, vol. 35, no. 1, pp. 95–105, 2011.

[5] L. Lócsi, "Calculating non-equidistant discretizations generated by Blaschke products," *Acta Cybernetica*, vol. 20, no. 1, pp. 111–123, 2011.

[6] L. Lócsi, "Approximating poles of complex rational functions," *Acta Univ. Sapientiae, Mathematica*, vol. 1, no. 2, pp. 169–182, 2009.

[7] A. Soumelidis, M. Pap, F. Schipp, J. Bokor, "Frequency domain identification of partial fraction models," in *Proc. 15th IFAC World Congress*, Barcelona, Spain, 2002, p. on CD.

[8] J. A. Nelder, R. Mead, "A simplex method for function minimization," *Computer Journal*, vol. 7, no. 4, pp. 308–313, 1965.

[9] A. L. Goldberger, L. A. N. Amaral, L. Glass, J. M. Hausdorff, P .Ch. Ivanov, R. G. Mark, J. E. Mietus, G. B. Moody, C. K. Peng, H. E. Stanley. (2000). "PhysioBank, PhysioToolkit, and Physionet: Components of a New Research Resource for Complex Physiologic Signals." *Circulation* [Online]. *101(23)*. pp. 215-220. Available: http://circ.ahajournals.org/cgi/content/full/101/23/e215

[10] P. S. Addison, "Wavelet transforms and ECG: a review," *Computer Journal*, vol. 26, pp. 155–199, 2005.

[11] P. S. Addison, The Illustrated Wavelet Transform Handbook: *Introductory Theory and Applications in Science, Engineering, Medicine and Finance*, 1rd ed.   Naiper University, Edinburgh, UK, 2002.

[12] G.D. Clifford, F. Azuaje and P.E. McSharry, Advanced Methods and Tools for ECG Data Analysis, 1rd ed.   Artech House, London and Boston, 2008.

[13] P. Kovács, "ECG signal generator based on geometrical features," *Annales Univ. Sci. Budapest., Sect. Comp.*, vol. 37, pp. 247–260, 2012.

[14] Y. Zigel, A. Cohen and A. Katz, "The Weighted Diagnostic Distortion (WDD) Measure for ECG Signal Compression," *IEEE Transactions on Biomedical Engineering*, vol. 47, pp. 1422–1430, 2000.

[15] D. Chetverikov, A. Axt, "Approximation-free running SVD and its application to motion detection," *Pattern Recognition Letters*, vol. 31, pp. 891–897, 2010.

[16] M. Karczewicz, M. Gabbouj, "ECG data compression by spline approximation," *Signal Processing*, vol. 59, pp. 43–59, 1997.

[17] G.D. Clifford, "Collection of ECG processing algorithms: Filters, " *http://www.mit.edu/~gari/CODE/FILTERS*, Feb. 22, 2007 [Oct. 26, 2012].

Péter Kovács was born in Budapest, Hungary. He received the BSc degree in Computer Science in 2008, the MSc degree (with honors) in mathematical modelling from Eötvös L. University, Budapest, Hungary, in 2010. Currently he is writing his PhD thesis in signal and image processing at the Department of Numerical Analysis of Eötvös L. University. His current research interests include rational function approximation theory, ECG signal processing, such as filtering, compressing, feature extraction and beat classification.

Levente Lócsi has received his MSc degree (with honors) in Computer Science in 2008 at the Faculty of Informatics, Eötvös L. University, Budapest, Hungary. He is now an assistant lecturer at the Department of Numerical Analysis (same Faculty) since 2011, teaching numerical methods, analysis and Matlab programming. His PhD is in progress with the topic of applying complex rational function systems in signal processing (with special emphasis on ECG signals).

Voltage-Controlled Square/Triangular Wave Generator with Current Conveyors and Switching Diodes

Martin Janecek, David Kubanek, and Kamil Vrba

Abstract—A novel relaxation oscillator based on integrating the diode-switched currents and Schmitt trigger is presented. It is derived from a known circuit with operational amplifiers where these active elements were replaced by current conveyors. The circuit employs only grounded resistances and capacitance and is suitable for high frequency square and triangular signal generation. Its frequency can be linearly and accurately controlled by voltage that is applied to a high-impedance input. Computer simulation with a model of a manufactured conveyor prototype verifies theoretical assumptions.

Keywords—Current conveyor, Relaxation oscillator, Schmitt trigger, VCO, Voltage-controlled oscillator.

I. INTRODUCTION

Square waveform generators with controllable frequency are widely used circuits in the fields of instrumentation and measurement. They serve as interfaces for signal processing from sensors [1], [2], [3], as they offer better electromagnetic interference immunity, lower sensitivity, and simpler structures compared to harmonic oscillators based on a linear positive feedback structure. Due to these advantages, many relaxation oscillators have been published recently [2] – [11]. The topology of relaxation oscillator usually consists of a Schmitt trigger and an integrator in a closed loop. Designers employed various active elements in these blocks. Initially mostly operational amplifiers were used, later operational transconductance amplifiers, current conveyors, current feedback operational amplifiers etc.

Our paper presents a novel square/triangular wave generator with current conveyors, only grounded resistances and integration capacitance. This makes the circuit attractive for integrated implementation. High-impedance voltage input is used to accurate, linear, and wideband control of oscillation frequency. The generator is a modification of an opamp-based circuit where the active elements were appropriately replaced by current conveyors. Thanks to conveyors the circuit can operate with wider bandwidth, higher slew rate, better accuracy, and higher dynamic range with low supply voltage.

II. GENERATOR CIRCUIT

A. Original Circuit with Opamps

The generator designed in this paper is based on the circuit shown in Fig. 1.
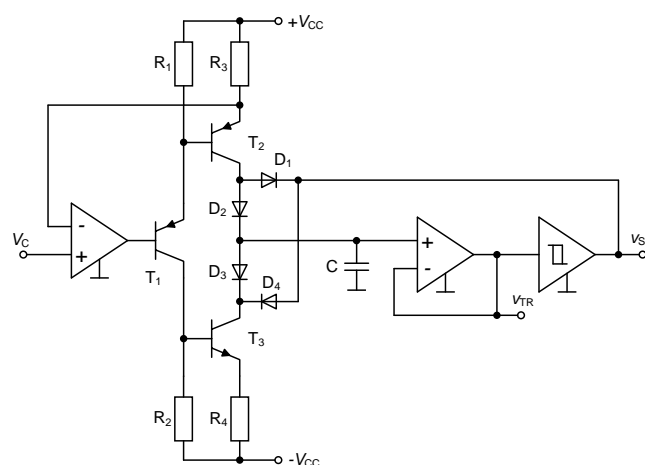

Fig. 1. Generator with operational amplifiers and transistors

It is a well known structure of relaxation oscillator where the capacitor C is periodically charged and discharged by a constant current that alternates its polarity. Magnitude of this current is directly proportional to the control voltage V_C and this current is generated in the left part of the circuit (from the capacitor C). The control voltage regulates the speed of charging the capacitor and also the frequency of the generated output signal. If it is valid $R_3 = R_4$, the collector currents of the transistors T_2 and T_3 are equal and are flowing down in the schematic (providing that the control voltage is positive). The diodes D_1 to D_4 ensure switching the T_2 and T_3 collector currents in the following way: if the hysteresis comparator output is low, D_1 is open and drains the entire T_2 collector current into the comparator output. Thus no current flows through D_2. In this period C is being discharged by the T_3 collector current via D_3. If the capacitor voltage reaches negative threshold of the comparator, the output of comparator changes to high. In this case D_2 leads the entire T_2 collector current into the capacitor which is being charged until its voltage reaches the positive threshold of the comparator. D_4 is open and no current flows through D_3. The voltage at v_{TR} output has a triangular waveform and voltage at v_{SQ} output a square waveform.

B. Current Conveyors Employed

Before we introduce the novel generator circuit, we present the current conveyors CCII+/- and UCC [12] that are employed in the circuit solution. Their symbols and terminal specification are shown in Fig. 2. The following relations are valid for the voltages and currents in Fig. 1:

UCC:
$I_{Y1+} = I_{Y2-} = I_{Y3+} = 0$, $V_X = V_{Y1+} - V_{Y2-} + V_{Y3+}$, $I_{Z1+} = -I_{Z1-} = I_{Z2+} = -I_{Z2-} = I_X$.

CCII+/−:
$I_Y = 0$, $V_X = V_Y$, $I_{Z+} = -I_{Z-} = I_X$.

These two conveyors are included in the integrated circuit UCC-N1B [13] whose samples were manufactured in the ON Semiconductor Design Centre Brno, Czech Republic. The proposed generator can be realized with only one UCC-N1B circuit.
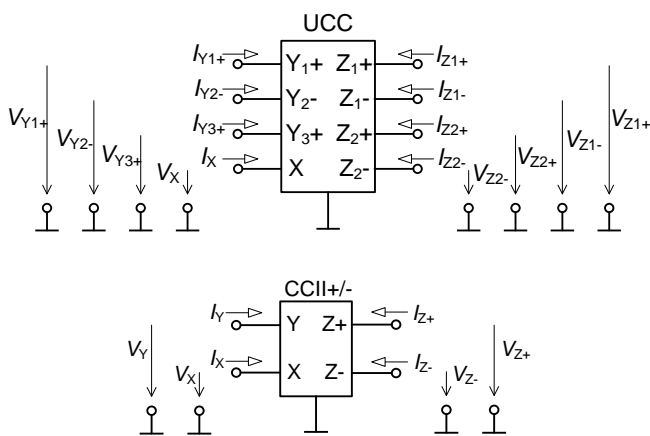

Fig. 2. UCC and CCII+/- symbols and their terminal specification

C. Oscillator with Current Conveyors

The proposed square/triangular wave oscillator is shown in Fig. 3.

As apparent, the transistor current source was replaced by CCII+/- which converts the input control voltage V_C to currents with opposite directions at Z+ and Z- outputs. The method of switching currents by the four diodes remained unchanged and works in the same way as described above.
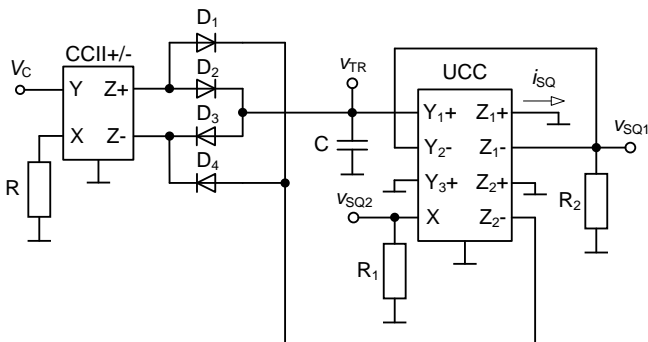

Fig. 3. Square/triangular wave generator

The slight difference is that cathode of D_1 and anode of D_4 are connected to current output of hysteresis comparator (Schmitt trigger) [11] which consists of UCC, R_1, and R_2. The Z_{1-} Y_{2-} connection provides a positive feedback in the comparator. It is necessary to select $R_2 > R_1$ to ensure the positive feedback with a loop-gain higher than unity. The input threshold levels of the comparator are given as

$$V_{TH} = -V_{TL} = I_{XZmax}(R_2 - R_1), \qquad (1)$$

where I_{XZmax} is the lower value of the two currents I_{Xmax} and I_{Zmax} which are the maximum currents that can be supplied by UCC at pins X and Z_{1-} respectively. The Schmitt trigger can be also designed using simple CCIIs as it was shown in [14], however, two active elements have to be used.

The triangular output voltage (v_{TR}) is taken directly from the capacitor C. Two voltage outputs (v_{SQ1} and v_{SQ2}) offer mutually inverted square waveforms. These outputs can be loaded only with very high impedance, otherwise a voltage buffer must be connected. A current output (i_{SQ}) is also available, which can be loaded by arbitrary impedance without affecting the circuit performance.

The frequency of the generated signal is

$$f_G = \frac{V_C}{2RC(V_{TH} - V_{TL})} = \frac{V_C}{4RCI_{XZmax}(R_2 - R_1)}. \qquad (2)$$

III. COMPUTER SIMULATION

While computing numerical parameters of the circuit and performing its simulations we will consider the real parameters of the UCC-N1B prototype. The maximum X and Z terminal currents of the conveyor are the same, namely $I_{Xmax} = I_{Zmax} = I_{XZmax} = 0.7$ mA. The resistance R_2 will be chosen 1 kΩ which results in the amplitude of the output voltage v_{SQ1} of 0.7 V. If the resistance $R_1 = 500$ Ω, the Schmitt trigger threshold voltage is according to (1) $V_{TH} = -V_{TL} = 0.35$ V. The resistance R was chosen 1 kΩ and diodes BAT68 Schottky.

Figs. 4 a) and b) show the waveforms of the generator with $V_C = 0.1$ V, $C = 5$ nF, (theoretical frequency $f_G = 14.3$ kHz), and $V_C = 0.7$ V, $C = 200$ pF, (theoretical frequency $f_G = 2.5$ MHz), respectively.

Fig. 4 a) shows the behaviour of the circuit at low frequency. Here the influence of conveyor non-idealities is very small and the waveforms are almost ideal. Distortion is apparent in Fig. 4 b) where the simulated frequency is about 1.5 MHz, which differs from the theoretical value, but the waveforms still maintain their shape.

Dependency of frequency on control voltage for three values of capacitance C is demonstrated in Fig. 5.

The simulated frequency corresponds very well with the ideal one computed by (2) at frequencies below 100 kHz. Above this frequency the error increases but the dependency is still nearly linear.
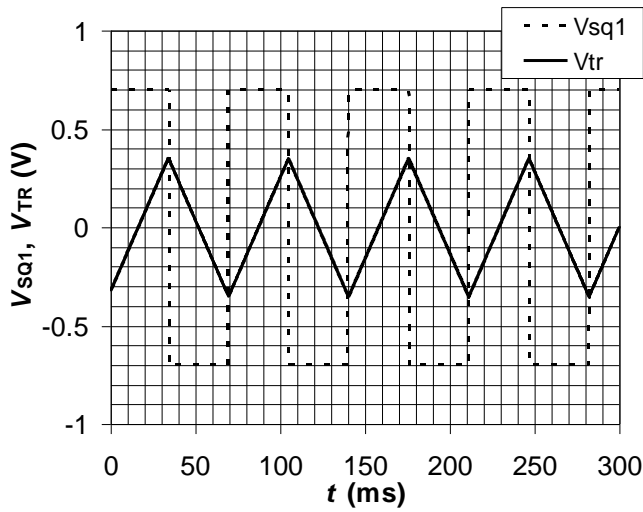
a)
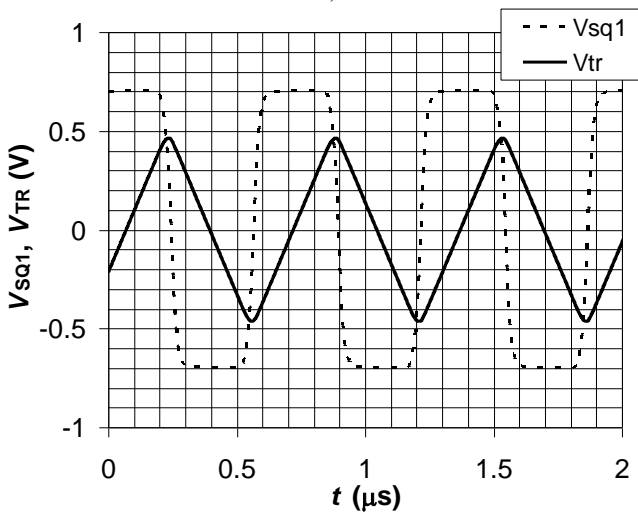
b)

Fig. 4. Simulated waveforms of the generator; a) $V_C = 0.1$ V, $C = 5$ nF; b) $V_C = 0.7$ V, $C = 200$ pF

IV. CONCLUSION

Relaxation oscillator with two current conveyors according to a classic circuit with operational amplifiers has been designed. It employs only grounded passive elements, which is advantageous for integrated implementation. The circuit features with voltage triangular-wave output and both voltage and current square-wave output.

The generated frequency is directly proportional to the control voltage and the relation for evaluating the generated frequency depending on the control voltage and element values has been given. The circuit functionality has been verified by computer simulations with a PSpice model of manufactured sample of universal current conveyor UCC-N1B. Thanks to the high-speed conveyors and diodes the circuit is suitable for generating high frequency signals. The generated frequency agrees with theoretical assumptions up to about 100 kHz and linearity of the frequency setting is maintained up to units of megahertz. The future work in this area will continue with practical implementation of the proposed circuit and modifications improving the accuracy of the generated frequency according to the control voltage.
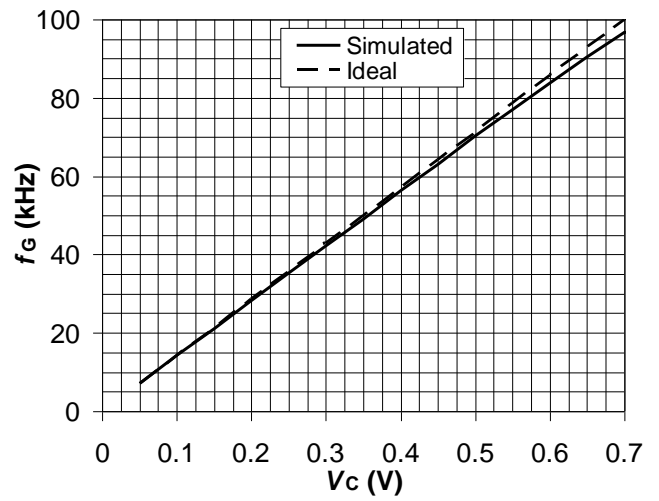
a)
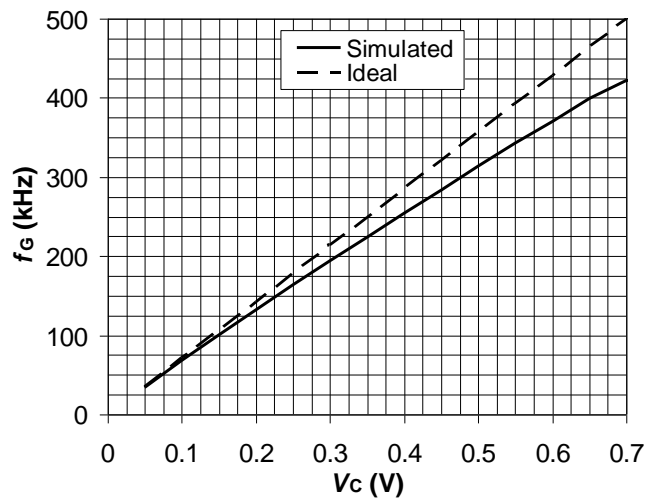
b)
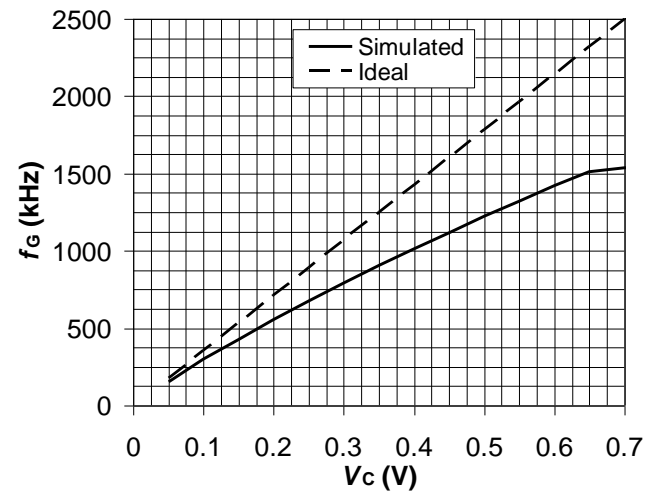
c)

Fig. 5. Generated frequency vs control voltage for three capacitances a) $C = 5$ nF, b) $C = 1$ nF, c) $C = 200$ pF

REFERENCES

[1] I. M. Filanovsky, Nonsaturated multivibrators for sensor signal conditioning, in *Proceedings of the IEEE 32nd Midwest Symposium on Circuits and Systems*, Vol. 36, pp. 1256–1257, 1989.

[2] S. N. Nihtianov, G. P. Shterev, B. Iliev, G. C. M. Meijer, An interface circuit for R-C impedance sensors with a relaxation

oscillator. *IEEE Trans. Instrum. Meas.*, Vol. 50, No. 6, pp. 1563–1567, 2001.

[3] M. T. Abuelma'atti, M. A. Al-Absi, A current conveyor-based relaxation oscillator as a versatile electronic interface for capacitive and resistive sensors. *Int. J. Electron.*, Vol. 92, No. 8, pp. 473–477, 2005.

[4] M. T. Abuelma'atti, M. A. Al-Absi, A low-cost dual/slope triangular/square wave generator. *Int. J. Electron.*, Vol. 91, No. 3, pp. 185–190, 2004.

[5] M. T. Abuelma'atti, S. M. Al-Shahrani, New CFOA-based triangular/square wave generator. *Int. J. Electron.*, Vol. 84, No. 6, pp. 583–588, 1998.

[6] B. Almashary, H. Alhokail, Current-mode triangular wave generator using CCIIs. *Microelectron. J.*, Vol. 31, pp. 239–243, 2000.

[7] W.-S. Chung, H. Kim, H.-W. Cha, H.-J. Kim, Triangular/squarewave generator with independently controllable frequency and amplitude. *IEEE Trans. Instrum. Meas.*, Vol. 54, No. 1, pp. 105–109, 2005.

[8] O. Cicekoglu, H. Kuntman, On the design of CCII+ based relaxation oscillator employing single passive element for linear period control. *Microelectron. J.*, Vol. 29, pp. 983–989, 1998.

[9] D. Pal, A. Srinivasulu, B.B. Pal, A. Demosthenous, B.N. Das, Current conveyor-based square/triangular wave generators with improved linearity. *IEEE Trans. Instrum. Meas.*, Vol. 58, No. 7, pp. 2174–2180, 2009.

[10] A. Srinivasulu, A novel current conveyor-based Schmitt trigger and its application as a relaxation oscillator. *Int. J. Circuit Theory Appl.*, Vol. 39, No. 6, pp. 679–686, 2011.

[11] S. Minaei, E. Yuce, A Simple Schmitt Trigger Circuit with Grounded Passive Elements and Its Application to Square/Triangular Wave Generator. *Circuits, Systems, and Signal Processing*, 22 November 2011, pp. 1–12, 2011.

[12] D. Kubanek, K. Vrba, Two-function Filters Employing UCCX Element. In *Proc. of the 27th Int. Conference Telecommunications And Signal Processing 2004*. Brno, Czech Republic, 2004, pp. 107–110.

[13] Datasheet: UCC-N1B Universal Current Conveyor (UCC) and Second-Generation Current Conveyor (CCII+/-), Rev. 0, 2011, available online:
www.utko.feec.vutbr.cz/~koton/soubory/UCC_N1B_Rev0.pdf

[14] J. Misurec, J. Koton, Schmitt Trigger with Controllable Hysteresis Using Current Conveyors. *International Journal of Advances in Telecommunications, Electrotechnics, Signals and Systems*, Vol. 1, No. 1, pp. 26-30, 2012. ISSN: 1805- 5443.

Martin Janecek received his BSc. degree in Electrical Engineering and Communication from Brno University of Technology, Czech Republic, in 2010. He is currently a MSc. student at the Department of Telecommunications, Brno University of Technology. He has expertise in new principles of designing non-linear analog circuits, particularly rectifiers, function approximation circuits, and relaxation oscillators based on non-conventional active elements.

David Kubanek was born in 1978. He graduated at the Faculty Electrical Engineering and Communication, Brno University of Technology in 2002 and received Ph.D. from the same university, in 2006. Since 2006, he has been an Assistant professor at the Department of Telecommunications, Brno University of Technology. His research interests include active filters, analog and digital signal processing, and digital modulation recognition.

Kamil Vrba received the Ph.D. degree in Electrical Engineering in 1976, and the Prof. degree in 1997, both from the Technical University of Brno. Since 1990 he has been Head of the Department of Telecommunications, Faculty of Electrical Engineering and Computer Science, Brno University of Technology, Brno, Czech Republic. His research work is concentrated on problems concerned with accuracy of analog circuits and mutual conversion of analog and digital signals. In cooperation with AMI Semiconductor Czech, Ltd. (now ON Semiconductor Czech Republic, Ltd.) he has developed number of novel active function blocks for analog signal processing such as universal current conveyor (UCC), universal voltage conveyor (UVC), programmable current amplifier (PCA), digitally adjustable current amplifier (DACA), and others. He is an author or co-author of more than 700 research articles published in international journals or conference proceedings. Professor Vrba is a Member of IEEE and IEICE.

Source Separation via Spectral Masking for Speech Recognition Systems

Gustavo Fernandes Rodrigues, Thiago de Souza Siqueira, Ana Cláudia Silva de Souza, and Hani Camille Yehia

Abstract—In this paper we present an insight into the use of spectral masking techniques in time-frequency domain, as a preprocessing step for the speech signal recognition. Speech recognition systems have their performance negatively affected in noisy environments or in the presence of other speech signals. The limits of these masking techniques for different levels of the signal-to-noise ratio are discussed. We show the robustness of the spectral masking techniques against four types of noise: white, pink, brown and human speech noise (bubble noise). The main contribution of this work is to analyze the performance limits of recognition systems using spectral masking. We obtain an increase of 18 % in the speech hit rate, when the speech signals were corrupted by other speech signals or bubble noise, with different signal-to-noise ratio of approximately 1, 10 and 20 dB. On the other hand, applying the ideal binary masks to mixtures corrupted by white, pink and brown noise, results in an average growth of 9 % in the speech hit rate, with the same differents signal-to-noise ratios. The experimental results suggest that the spectral masking techniques are more appropriate when applied to bubble noise, which is produced by human speech, than to white, pink and brown noise.

Keywords—Blind source separation, Independent component analysis, Neural networks, Spectral masking, Speech recognition.

I. Introduction

When several people are talking at the same time in a meeting or public places, it is necessary to separate the voice of a given person or an specific source from other interference sources so that each speaker can be recognized. Independent components analysis has been an important source separation technique, however, with the presence of noise and reverberation, the separated signals have strong residual components of other interference sources [1]. In these cases, a signal preprocessing method must be used in order to reduce other sources of interference. Our goal is to show the potential improvement of automatic speech recognition in noisy environments or with multiple speech signals. In this paper, we show that spectral masking techniques, used as preprocessing tools, reduce other sources of interference and increase the efficiency of the speech recognition systems.

Several works use observation vectors of uncertainties in the decoding process for the treatment of noisy signals in the automatic speech recognition task [2]–[4]. When dealing with

speech recognition in environments with several speakers, such as the ones in [5]–[7], some authors suggest the use of binary masking [8], [9]. However, when speech signals are exposed to environments with reverberation and in the presence of other speakers, the process of extracting the masks becomes extremely difficult. This paper intends to quantify and analyze the efficiency of the spectral masking in speech recognition tasks.

The majority of speech recognition systems does not show good performance in noisy environments or when there are interferences from other voices. Therefore, we intend to improve the efficiency of speech recognition systems through the implementation of a source separation method using spectral masking in time-frequency domain, as a preprocessing stage. Time-frequency domain masking is used to extract an specific speech signal from the noise corrupted signal [10], [11]. The mel-cepstral parameters are used in the speech recognition step to provide the input data to the speech recognition system. Some papers show that binary masking provides extracting information in time-frequency domain which best characterizes speech signal [11]. The necessity to improve the speech recognition system's performance in environments under adverse conditions and multiple speakers has attracted researchers attention and many papers about separation of speech signals have been published [1], [4]–[6], [9], [10]–[14].

This paper is organized as follows. In Section II we discuss source separation techniques via spectral masking. In Section III we describe the steps to obtain the speech signals parameters and discuss the implementation of the speech recognition system. In Section IV we show the results of the experiments and simulations done to verify the influence of noise and other voices in speech recognition tasks. The tests made to analyze the limits and improvement capacity of the speech recognition systems through spectral masking as well as the analysis of the results obtained are detailed in Section IV. Finally, Section V outline the conclusions of this work.

II. Spectral Masking in time-frequency domain

An specific sound source can be recovered by applying a weighted mask to an acoustic mixture at each point in the time-frequency domain. The regions dominated by this source receive higher weights than the ones where other sound sources of the analyzed mixture prevails. The masks may be binary or assume real values. The use of a binary mask is motivated by the masking process which occurs in human audition, where a more intense sound can mask or obscure a less intense one within the same critical band. With the

G. F. Rodrigues, T. S. Siqueira and A. C. Souza are Department of Telecommunications and Mechatronic Engineering, Federal University of São João del-Rey, Ouro Branco, Minas Gerais, Brazil (corresponding author to provide phone and fax: +55 31 37413583, e-mail: gustavofernandes@gmail.com).

H. C. Yehia is with Department of Electronic Engineering, Federal University of Minas Gerais, Belo Horizonte, Minas Gerais, Brazil.

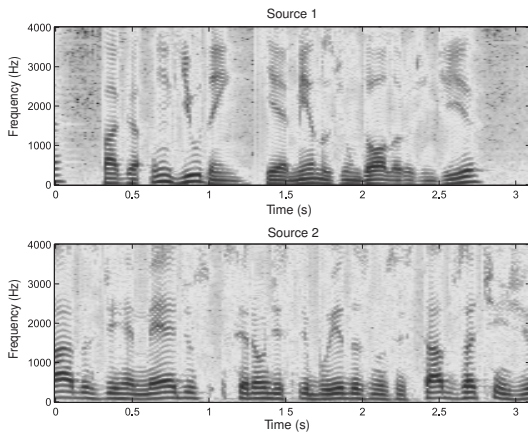Manuscript received October 28, 2012.

Fig. 1.   Two speech spectrograms.

Fig. 2.   Images of binary ideal masks from the sources (s_1 and s_2) for 100 speech frames.

purpose of separating the voice signals, [15] proposed the usage of an ideal binary mask. Given a speech signal $s(t, f)$ and a noise $n(t, f)$, where t and f represent the instant in time and frequency, respectively, the ideal binary masking $m(t, f)$ can be obtained through the following expression:

$$m(t, f) = \begin{cases} 1 & if \quad s(t, f) > n(t, f), \\ 0 & otherwise. \end{cases} \quad (1)$$

A similar approach was adopted in [16], who observed an orthogonal tendency in different voice signals in time-frequency domain with high resolution, showing that it is possible to separate signals through binary masking. Several papers have shown that the speech signal reconstructed by an ideal binary mask is intelligible when extracted from a mixture of two or more speakers [9], [17], [18].

The ideal binary mask considered here is a binary matrix which assumes value one when the signal energy is stronger than the interference signal for a specific frequency in a given instant and assumes value zero otherwise. When we apply an ideal mask to an instantaneous mixture of two speech signals, we notice that the signal obtained is perfectly audible, with good quality and no interference from the other signal.

In order to obtain the ideal mask, the source signals (s_1 and s_2) are transformed to time-frequency domain and their spectrograms are given, respectively, by:

$$\begin{aligned} s_1(t) &\rightarrow S_1(w, t), \\ s_2(t) &\rightarrow S_2(w, t), \end{aligned} \quad (2)$$

where w represents angular frequency and t represents the time instant of the voice frame being analyzed. The binary masking can be determined by comparing the magnitude of two spectrograms, as shown in Fig. 1.

The ideal masks (M_1 and M_2) were obtained as follows:

$$\begin{aligned} M_1(w, t) = 1, & \quad for \quad |S_1(w, t)| > |S_2(w, t)|, \\ M_2(w, t) = 1, & \quad for \quad |S_2(w, t)| > |S_1(w, t)|, \end{aligned} \quad (3)$$

and the other values of the masks are equal to zero.

Fig. 2 shows an example of ideal binary masks applied to two speech signals, sampled at 8000 Hz, divided in frames of 512 samples with 50% overlap.
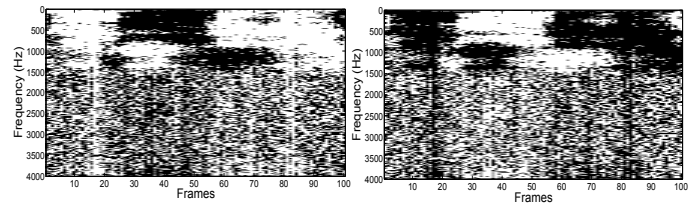
Spectral masking techniques can be applied to speech signal separation, specially when the mixture is corrupted by noise signals. When applying an ideal binary mask to separate two speech signals, it is possible to improve the signal-interference ratio over 40 dB (SIR), but it also increases the signal-distortion ratio (SDR) in 20 dB [1]. However, an ideal binary mask can not be obtained without knowledge of the real signals and an approximation is needed. In order to obtain this approximation, several methods to estimate masks based on ICA (independent component analysis) can be found in the literature, both for binary and continuous masks [12], [14].

The signal-distortion ratio decreases about 3 dB when approximately 10% of the bits of the ideal binary mask are inverted, as shown in [19]. An error of 10% of the bits in the binary masks estimate is acceptable without loss of intelligibility [19], [20].

The objective of this paper is to show the potential improvement of the speech recognition systems, in noisy environments or with multiple speech signals, using spectral masking techniques. We present a signal preprocessing method to reduce other sources of interference, using ideal binary masks. In this experiment, the speech signals or noise signals were known. This fact allows to obtain the ideal binary mask from each mixture analyzed. We use all the recordings to simulate mixtures corrupted by noise, and therefore to obtain the ideal masks. The ideal binary masks obtained were applied to a mixture corrupted by other speech signal or noise, sampled at 8000 Hz, divided in frames of 512 samples with 50% overlap. The ideal binary masks were used to separate the signal of interest (speech signal) from the noise, as a preprocessing step for the speech signal recognition.

The ideal masks obtained were directly applied to the speech signal mixtures in time-frequency domain, before the extraction of the mel-cepstral coefficients and the learning process of the neural network used in the speech recognition tests. The ideal masks were not applied in the training set used to train the neural network.

III. SPEECH RECOGNITION SYSTEM

Speech recognition systems have low performance in noisy environments or in the industry. In this work, we are concerned with real situations where speech signals are corrupted by noise, including other speech signals. A speaker dependent speech recognition system was used to recognize isolated voice commands from a limited vocabulary (30 Portuguese words) and each word was recorded 20 times by one speaker. The corpus consists of voice commands that can be used

in automation and control systems . The Portuguese words used were: right, left, stop, go back, go on, ahead, behind, on, off, fast, slow, turn on, turn off, up, down, speed up, lock, unlock and alarm. Besides these words, the database consists of eleven digits: 0 to 10. The ideal binary masks were used to separate the target speech signals from a mixture with other speech signal or other types of noise. We use all the recordings to simulate mixtures corrupted by noise, and therefore to obtain the ideal masks. The ideal masks obtained were directly applied to the speech signal mixtures in time-frequency domain, before the extraction of the mel-cepstral coefficients and the learning process of the neural network used in the speech recognition system.

A. Extraction of Mel-Cepstral coefficients

The mel-cepstral parameters are the most used features in speech recognition systems as input data. A Mel is unity of measurement for the perceived pitch of a tone. It does not have a linear correspondence to the physic frequency. The Mel scale is defined by a mapping between the frequency scale (in Hz) and the perceived frequency scale (in Mel). The mapping is linear until approximately 1 KHz and logarithmic for superior frequencies. The frequency scale denominated Mel is closely related to the critical-band of the auditory human system and the mel-cepstral coefficients are obtained from the Mel frequency.

The extraction of the mel-cepstral coefficients consists of the following the steps: (i) to obtain the magnitude spectrum of the signal by applying Fourier transform; (ii) to calculate each output of a filter bank in the Mel scale as a sum of the weighted spectral magnitude of each frame; (iii) to obtain the logarithm of the magnitude spectrum in each filter output; (iv) to take the discrete cosine transform (DCT) from each frame.

The speech signals used were recorded with a sampling frequency of 8000 Hz. In the extraction step, the data were divided in frames of 512 samples with 50% overlap. For each frame, a Hamming window was applied followed by 13th order mel-cepstral coefficients.

B. Principal Components Analysis

Principal Components Analysis (PCA) consists of a linear transformation of "m" original variables in "m" new variables, in such a way that the first new variable accounts for as much of the variability in the data as possible and each succeeding component in turn has the highest variance possible under the constraint that it is uncorrelated with the preceding ones, until each variance in the set has been explained. The purpose of this technique in this case is to allow a reduction in the dimension of the data, therefore minimizing error.

For each frame we have used 13 mel-cepstral coefficients and therefore the data set was represented by a Nx13 vector, where N corresponds to the number of frames in analysis.

$$x_n = [x_1(n) \ x_2(n) \ \cdots \ x_{13}(n)]^T, \qquad (4)$$

where $[.]^T$ denotes a transpose matrix. The variable x_n, $1 \le n \le N$ represents one frame of the audio signal being analyzed. The set of all frames is represented by the N-sized vectors:

$$X = [x_1 \ x_2 \ \cdots \ x_N], \qquad (5)$$

where each column of X denotes the 13 coefficients of each signal frame. From that, the covariance matrix is defined by:

$$C = [X - \mu][X - \mu]^T, \qquad (6)$$

where μ is a mean vector. Then, through the decomposition of singular values (SVD) one can denote the covariance matrix as:

$$C = USU^T, \qquad (7)$$

where U is a matrix whose columns are eigenvectors of C and S is a diagonal matrix containing the respective eigenvalues of C.

The sum of the eigenvalues represents the total variance observed in C. Therefore, if the sum of the first k eigenvalues reaches a proportion, as the one considered, of 85% of the sum of all eigenvalues, then the first k eigenvectors of C will account for most of the total variance observed in the data set. In this paper we used the first three components as the input vector for the pattern classification by neural network. The dimensions of speech features were reduced to a vector of 39 values for each word.

C. Learning with neural network

A training corpus of 600 utterances was used from which half was used for training and the remaining for testing. The input speech was reduced to a vector of 39 values for each word from the mel-cepstral coefficients (the dimension was reduced by PCA).

Algorithms based on neural network of type multi-layer perceptron, using backpropagation algorithm to the supervised learning process has been used in voice recognition systems [21]–[24]. The network used in this paper is a feedforward multilayer perceptron (MLP) trained with stochastic back-propagation algorithm. This experiment uses three layer MLP: one input layer, one hidden layer and one output layer. The feature vectors representing speech pattern are fed into neural network at the input layer. Only 39 values (from mel-cepstral coefficients with the dimension reduced by pca) for each word are fed to the neural network. In this neural network there is a single hidden layer that has 30 neurons. The numbers of neurons in output layers is set to five. The output of the network is a binary value representing the recognized word. The hidden and output neurons are activated using sigmoidal and linear activation functions respectively. Once the network is created, it can be trained for a specific problem by presenting training inputs and their corresponding targets (supervised training). A set of 10 samples of each word (300 utterances) was used as training data and another part as test data. The binary masks were not used in the training set. The ideal masks were applied only in the test set used to test the neural network.
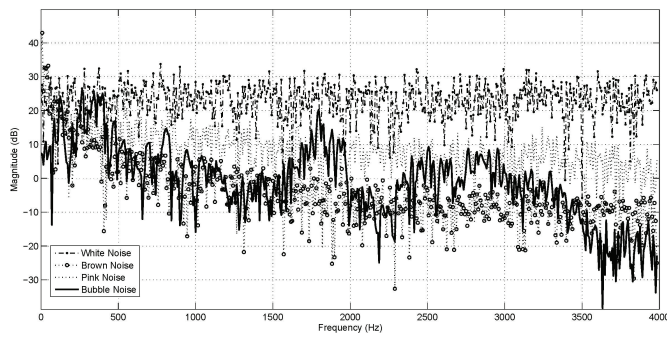
Fig. 3.   Frequency spectrum of white, pink, brown and bubble noise.

TABLE I
THE SPEECH SIGNALS WERE CORRUPTED BY ONE SPEECH SIGNAL FROM
ANOTHER SPEAKER WITH DIFFERENT LEVELS OF SIGNAL-TO-NOISE RATIO
(1, 10, 20 E 30 DB). THE TESTS WERE PERFORMED USING AN IDEAL
BINARY MASK AND WITHOUT APPLICATION OF THE IDEAL MASK.

Mixture corrupted by one speech signal					
Without masking			With masking		
SNR (dB)	Hit Rate (%)	Standard Deviation	SNR (dB)	Hit Rate (%)	Standard Deviation
1	31	9	1	48	11
10	43	12	10	64	15
20	66	16	20	79	16
30	85	19	30	87	17

IV. RESULTS

The recordings were made in a laboratory with low noise level, with approximately zero reverberation time and sampling frequency of 8000 Hz. The hit rate (word recognition rate) was used as a measure of the speech recognition efficiency. Another common metric is the word error rate (WER). We decided to use the hit rate measure as the mirror representation of the word error rate. In order to obtain the speech hit rates, 100 simulations were made for each case being analyzed. Different simulations were done for testing, where the original speech signal was corrupted by other speech signals from different speakers and by different types of noise. In each case different levels of signal-to-noise ratio (1, 10, 20 and 30 dB) were considered.

The definition of noise is derived from a random signal, but it can have different characteristic statistical properties. In this paper, we analyzed the limits of spectral masking techniques for the following types of noise: white, pink, brown and a human speech noise (bubble noise). By definition, the white noise has a flat frequency spectrum. The Pink noise or "$1/f$ noise" is a signal with power spectral density inversely proportional to the frequency. The power density, compared with white noise, decreases by 3 dB per octave (density is proportional to $1/f$). The brown noise refers to a power density which decreases 6 dB per octave with increasing frequency (density is proportional to $1/f^2$). In order to create a noise with a frequency spectrum similar to the human speech we concatenated all the words of the vocabulary used is this work, spoken by 3 males and 3 females [25]. The frequency spectrum of these different types of noise used is shown in 3.

TABLE II
THE SPEECH SIGNALS WERE CORRUPTED BY TWO SPEECH SIGNALS FROM
OTHER SPEAKERS WITH DIFFERENT LEVELS OF SIGNAL-TO-NOISE RATIO
(1, 10, 20 E 30 DB). THE TESTS WERE PERFORMED USING AN IDEAL
BINARY MASK AND WITHOUT APPLICATION OF THE IDEAL MASK.

Mixture corrupted by two speech signal					
Without masking			With masking		
SNR (dB)	Hit Rate (%)	Standard Deviation	SNR (dB)	Hit Rate (%)	Standard Deviation
1	28	9	1	48	12
10	47	12	10	65	18
20	60	18	20	81	18
30	85	15	30	88	19

TABLE III
THE SPEECH SIGNALS WERE CORRUPTED BY THREE SPEECH SIGNALS
FROM OTHER SPEAKERS WITH DIFFERENT LEVELS OF SIGNAL-TO-NOISE
RATIO (1, 10, 20 E 30 DB). THE TESTS WERE PERFORMED USING AN
IDEAL BINARY MASK AND WITHOUT APPLICATION OF THE IDEAL MASK.

Mixture corrupted by three speech signal					
Without masking			With masking		
SNR (dB)	Hit Rate (%)	Standard Deviation	SNR (dB)	Hit Rate (%)	Standard Deviation
1	32	11	1	56	12
10	52	16	10	68	16
20	68	21	20	82	16
30	89	15	30	89	17

TABLE IV
THE SPEECH SIGNALS WERE CORRUPTED BY DIFFERENT TYPES OF NOISE
WITH DIFFERENT LEVELS OF SIGNAL-TO-NOISE RATIO (1, 10, 20 E 30
DB). THE TESTS WERE PERFORMED USING AN IDEAL BINARY MASK AND
WITHOUT APPLICATION OF THE IDEAL MASK.

Mixture corrupted by a white noise					
Without masking			With masking		
SNR (dB)	Hit Rate (%)	Standard Deviation	SNR (dB)	Hit Rate (%)	Standard Deviation
1	23	9	1	33	10
10	30	9	10	51	11
20	53	9	20	52	12
30	64	16	30	72	17
Mixture corrupted by a pink noise					
Without masking			With masking		
SNR (dB)	Hit Rate (%)	Standard Deviation	SNR (dB)	Hit Rate (%)	Standard Deviation
1	25	9	1	37	9
10	44	12	10	54	13
20	58	17	20	63	16
30	77	21	30	79	17
Mixture corrupted by a brown noise					
Without masking			With masking		
SNR (dB)	Hit Rate (%)	Standard Deviation	SNR (dB)	Hit Rate (%)	Standard Deviation
1	54	15	1	65	16
10	56	16	10	66	15
20	78	20	20	80	16
30	88	17	30	91	18
Mixture corrupted by a bubble noise					
Without masking			With masking		
SNR (dB)	Hit Rate (%)	Standard Deviation	SNR (dB)	Hit Rate (%)	Standard Deviation
1	32	8	1	53	14
10	60	16	10	74	13
20	77	21	20	81	14
30	89	14	30	90	13

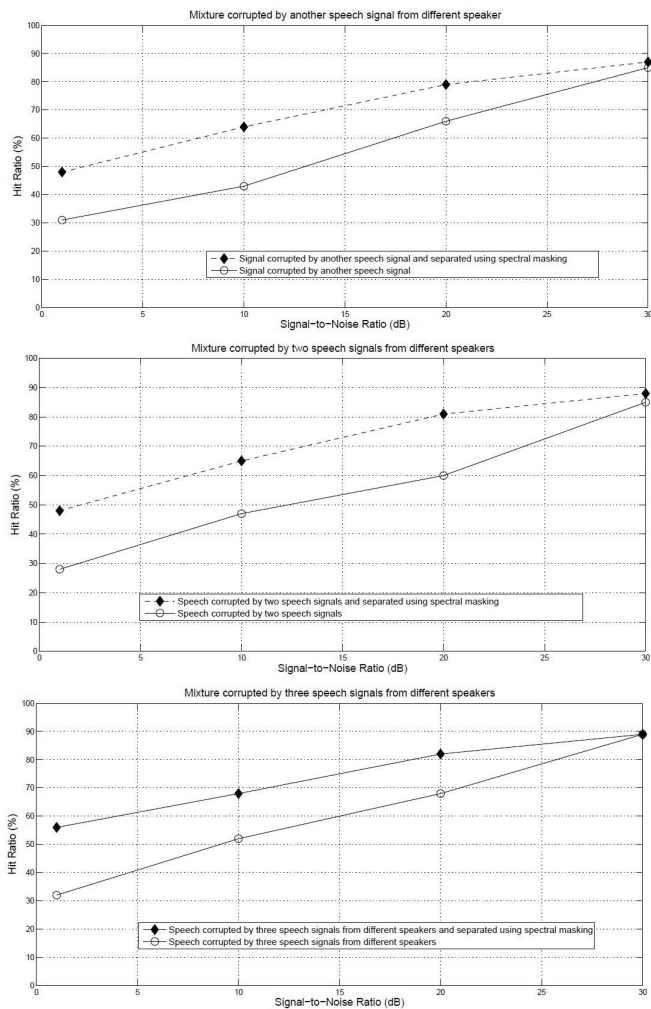The following cases were analyzed: i) speech signal corrupted by a speech signal from another speaker; ii) speech
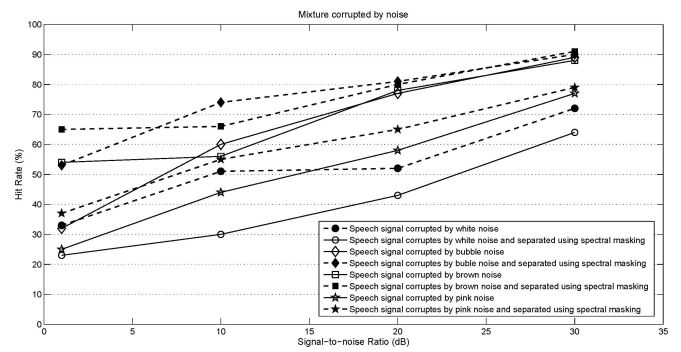
Fig. 5. Speech hit rate for the cases where the original speech signals were corrupted by different types of noise (white, pink, brown and bubble) with different signal-to-noise ratios (1, 10 and 20 dB). The limits of performance improvement of the recognition system using ideal spectral masking (with masking) were analyzed.

shown in Fig. 4.

We show the robustness of the spectral masking techniques against four types of noise as well: white, pink, brown and bubble. In cases where the signal is corrupted by different types of noise, with SNR of approximately 30 dB (low level noise), we notice a small performance improvement of the hit rate when the ideal binary mask was applied, as shown in Table IV.

Moreover, when applying ideal binary masking with higher levels of speech human noise (1,10 and 20 dB) we observe an average growth of 18 percent in the hit rate, similar to that observed in tables I, II and III for the same levels of signal-to-noise ratio. On the other hand, applying the ideal binary masks to mixtures corrupted by white, pink and brown noise, results in an average growth of 9 % on the speech hit rate, with the same different signal-to-noise ratio.

Among the different types of noise, the experimental results reveal that the best hit rates, when applying ideal binary masking, were obtained while using the bubble noise. The worst results were obtained applying the ideal mask to white noise as in Fig. 5. This suggests that the masking spectral techniques works best for bubble noise, which is produced by human speech and justify its applications to realistic situations like human communication.

V. CONCLUSIONS

In this paper we presented an insight into the use of spectral masking techniques in time-frequency domain, as a preprocessing step for the speech signal recognition. Speech recognition systems have their performance negatively affected in noisy environments or in the presence of other voice signals. A speech recognition system based on source separation using ideal binary masks was presented in order to investigate the performance improvement in speech recognition. The signals were corrupted by noise (speech signals and different types of noise) with different signal-to-noise ratios (1, 10, 20 e 30 dB) during the tests. We show the robustness of the spectral masking techniques in the presence of four types of noise: white, pink, brown and bubble. The main contribution

Fig. 4. Speech hit rate for the cases where the original speech signals were corrupted by other speech signals from different speakers with different signal-to-noise ratios (1, 10 and 20 dB). The limits of performance improvement of the recognition system using ideal spectral masking (with masking) were analyzed.

signal corrupted by two other speech signals from different speakers; iii) speech signal corrupted by three other speech signals from different speakers; iv) speech signal mixture corrupted by different types of noise.

According to the results shown in Fig. 4, we verify that in case the speech signal is corrupted by low level noise composed of other speech signals with a signal-to-noise ratio of approximately 30 dB, the hit rate is the same as when the ideal binary mask was applied. In some cases there was a small performance improvement when using the ideal binary mask, as shown in Tables I and II.

We also verify that in the cases where the original signals were corrupted by other speech signals with signal-to-noise ratio levels of 1, 10 and 20 dB, there is an average growth of 18 percentual points in the hit rate when applying ideal binary masking. These results show that when various signals are mixed, spectral masking technique provides a gain of approximately 10 dB in noise level attenuation, significantly improving the speech recognition systems performance, as

of this study was the analysis of the limits of performance improvement of the recognition systems using ideal spectral masking. We verified an average improvement of 18% of the hit rates for signal-to-noise ratios of 1, 10 and 20 dB. We also showed that the spectral masking techniques when applied to mixtures corrupted by other speech signals provide an average gain of 10 dB in noise level attenuation, for the same conditions of signal-to-noise ratios mentioned above. The experimental results suggest that the masking spectral techniques are more appropriate for the case when it is applied a bubble noise, which is produced by human speech, than for the case of applying white, pink and brown noise.

ACKNOWLEDGMENT

REFERENCES

[1] D. Kolossa, R. F. Astudillo, E. Hoffmann and R. Orglmeister, "Independent Component Analysis and Time-Frequency Masking for Speech Recognition in Multitalker Conditions," *EURASIP Journal on Audio, Speech, and Music Processing*, 2010.

[2] T. T. Kristjansson and B. J. Frey, "Accounting for uncertainty in observations: a new paradigm for robust automatic speech recognition," in *Proceedings of the IEEE International Conference on Acustics, Speech, and Signal Processing*, 2002.

[3] V. Stouten, H. Van Hamme and P. Wambacq, "Application of minimum statistics and minima controlled recursive averaging methods to estimate a cepstral noise model for robust ASR," in *Proceedings of the IEEE International Conference on Acoustics, Speech and Signal Processing*, vol. 1, 2006.

[4] M. Van Segbroeck and H. Van Hamme, "Robust speech recognition using missing data techniques in the prospect domain and fuzzy masks," in *Proceedings of the IEEE International Conference on Acoustics, Speech and Signal Processing*, 2008, pp. 4393–4396.

[5] D. Kolossa, A. Klimas and R. Orglmeister, "Separation and robust recognition of noisy, convolutive speechmixtures using time-frequency masking and missing data techniques," in *IEEE Workshop on Applications of Signal Processing to Audio and Acoustics*, 2005, vol. 13, pp. 82–85.

[6] M. Kühne, R. Togneri and S. Nordholm, "Time-frequency masking: linking blind source separation and robust speech recognition in Speech Recognition: Technologies and Applications," *IN-TECH, Vienna, Austria*, 2008, pp. 61–80.

[7] S. Srinivasan and D. Wang, "Transforming binary uncertainties for robust speech recognition," *IEEE Transactions on Audio, Speech and Language Processing*, vol. 15, no. 7, pp. 2130–2140, 2007.

[8] O. Yilmaz and S. Rickard, "Blind separation of speech mixtures via time-frequency masking," *EURASIP Journal on Audio, Speech, and Music Processing*, vol. 52, no. 7, pp. 1830–1847, 2004.

[9] G. J. Brown and D. L. Wang, "Separation of speech by computational auditory scene analysis," in *Speech Enhancement*, J.Benesty, S. Makino, and J. Chen, Ed. Springer, New York, 2005, pp. 371–402.

[10] S. Srinivasan, N. Roman and D. L. Wang, "Binary and ratio time-frequency masks for robust speech recognition," *Speech Communication*, vol. 48,pp. 1486–1501, 2006.

[11] S. Srinivasan, N. Roman and D. L. Wang, "On binary and ratio time-frequency masks for robust speech recognition," in *Proc. International Conference on Spoken Language Processing*, 2004, pp. 2541–2544.

[12] H. Sawada, S. Araki, R. Mukai and S. Makino, "Blind extraction of dominant target sources using ICA and timefrequency masking," *IEEE Transactions on Audio, Speech and Language Processing*, vol. 14, no. 6, pp. 2165–2173, 2006.

[13] T. S. V. Souza, G. F. Rodrigues, A. C. S. Souza, J. M. Moreira and H. C. Yehia, "Binary Spectral Masking for Speech Recognition Systems," in *Proc. 35th International Conference on Telecommunications and Signal Processing (TSP)*, 2012, pp. 432–436.

[14] E. Hoffmann, D. Kolossa and R. Orglmeister, "A batch algorithm for blind source separation of acoustic signals using ICA and time-frequency masking," in *Proceedings of the 7th International Conference on Independent Component Analysis and Signal Separation*, 2007, pp. 480–487.

[15] G. Hu and D. L. Wang, "Speech segregation based on pitch tracking and amplitude modulation," in *Proc. IEEE Workshop on Applications of Signal Processing to Audio and Acoustics*, 2001, pp. 79–82.

[16] A. Jourjine, S. Rickard and O. Yilmaz, "Blind separation of disjoint orthogonal signals: Demixing N sources from 2 mixtures," in *IEEE Conference on Acoustics, Speech, and Signal Processing (ICASSP2000)*, Jun. 2000, vol. 5, pp. 2985–2988.

[17] N. Roman, D. L. Wang and G. J. Brown, "Speech segregation based on sound localization," *J. Acoust. Soc. Am.*, vol. 114, pp. 2236–2252, 2003.

[18] N. Roman and D. L. Wang, "Binaural sound segregation for multisource reverberant environments," in *Proc. IEEE ICASSP*, 2004, vol. 2, pp. 373–376.

[19] G. F. Rodrigues and H. C. Yehia, "Limitations of the Spectrum Masking Technique for Blind Source Separation," *Lecture Notes in Computer Science*, vol. 5441, pp. 621–628, 2009.

[20] N. Li and P. C. Loizou, "Factors influencing intelligibility of ideal binary-masked speech: Implications for noise reduction," *J. Acoust. Soc. Am.*, vol. 3, no. 123, pp. 1673–1682, 2008.

[21] B. S. Kirei, M. D. Topa, I. Muresan, I. Homana and N. Toma, "Blind Source Separation for Convolutive Mixtures with Neural Networks," *Advances in Electrical and Computer Engineering*, vol. 11, no. 1, pp. 63–68, 2011. Available:http://dx.doi.org/10.4316/AECE.2011.01010

[22] A. M. Ahmad, S. Ismail and D. F. Samaon, "Recurrent neural network with backpropagation through time for speech recognition," in *Proceedings of the IEEE international symposium on communications and information technology*, 2004, vol. 1, pp. 98–102.

[23] R. P. Lippmann, "Neural network classifiers for speech recognition," *The Lincoln Laboratory Journal*, vol. 1, pp. 107–128, 1988.

[24] S. I. Amari and A. Cichocki, "Adaptive Blind Signal Processing - Neural Network Approaches," in *Proceedings of IEEE*, 1998, vol.86, no. 10.

[25] D. Kobayashi, S. Kajita, K. Takeda and F. Itakura, "Extracting speech features from human speech like noise," in *Proceedings of IEEE, Fourth International Conference on Spoken Language (ICSLP 96)*, 1996, vol. 1, pp. 418–421.
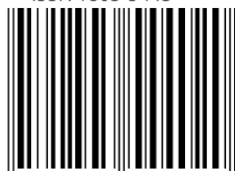
Gustavo Fernandes Rodrigues holds the degree of Electrical Engineer (CEFET-MG, 2008), Master of Electrical Engineering (UFMG, 2003) and Doctor of Electrical Engineering (UFMG, 2008). Currently, he holds the position of Professor at the Department of Telecommunications and Mechatronics Engineering of UFSJ. His research interests include signal processing, speech recognition and blind source separation.

Thiago de Souza Siqueira is an undergraduate student at the Telecommunications Engineering Program at Universidade Federal de São João del-Rei (UFSJ).

Ana Cláudia Silva de Souza holds the degree of Electrical Engineer (UFMG, 2003), Master of Electrical Engineering (UFMG, 2005) and Doctor of Electrical Engineering (UFMG, 2010). At 2008 worked at the Advanced Telecommunications Research Institute (ATR) in Japan. Currently, she holds the position of Professor at the Department of Telecommunications and Mechatronics Engineering of UFSJ. Her research interests are in Biomedical Engineering, focusing on biomedical signal processing and medical image.

Hani Camille Yehia holds the degrees of Electronics Engineer (ITA, 1988), Master of Electronic Eng. and Computer Science (ITA, 1992) and Doctor of Electrical Eng. (Nagoya University, 1997). From 1996 to 1998 he held the position of researcher at the ATR Laboratories (Japan). He holds the position of Professor at the Electronics Dept. and is currently the head of Inova-UFMG Technology Incubator. He is the head of CEFALA - Center for Research on Speech, Acoustics, Language and Music, developing research on Audiovisual production and perception of speech and Music.

12 >